UNIVERSITA' DEGLI STUDI DI PADOVA

Dipartimento di Ingegneria Elettrica

SCUOLA DI DOTTORATO DI RICERCA
IN INGEGNERIA INDUSTRIALE
INDIRIZZO: MECCATRONICA E SISTEMI INDUSTRIALI
CICLO XX

ADVANCED TOPICS ON MOTOR DRIVES FOR EMERGING MECHATRONIC APPLICATIONS

Direttore della Scuola: Ch.mo Prof. Paolo Bariani

Coordinatore: Ch.mo Prof. Alessandro Persona

Supervisore: Ch.mo Prof. Silverio Bolognani

Dottorando: Luca Sgarbossa

31 gennaio 2008

To my family and my friends.

Contents

Sommario

Gli azionamenti elettrici, oggigiorno, si stanno diffondendo rapidamente in svariate applicazioni emergenti meccatroniche come la robotica, gli azionamenti di precisione, i servoazionamenti in campo medico, i veicoli ibridi, l'automazione industriale e tanto altro. Si manifesta, perciò, la necessità di soddisfare richieste di prontezza ed affidabilità sempre più esigenti.

Particolare riguardo nella progettazione della macchina elettrica e una adeguata cura nella modellazione della stessa e implementazione del controllo, riescono a migliorare la dinamica e l'affidabilità dell'azionamento, oltre a portare benefici in termini di costi.

La presente tesi di dottorato affronta, nella prima parte, l'aspetto della modellazione del motore sincrono a magneti permanenti, partendo da approfondimenti teorici per arrivare alla descrizione di un insieme basilare di misure per la caratterizzazione del modello stesso.

Allo scopo è stato sviluppato un banco prova come supporto per la verifica sperimentale dopo la progettazione o le simulazioni, nonché come utile strumento di caratterizzazione dei suddetti motori a scopi di controllo. In questo modo è possibile predisporre un modello matematico accurato, essenziale per lo studio di affinate tecniche di controllo.
Il banco di misura è totalmente automatizzato nell'eseguire le prove, in modo tale da garantire il più possibile la ripetibilità delle misure.

Nella seconda parte della tesi si descrivono alcune applicazioni di azionamenti con motore sincrono a magneti permanenti (alcune adatte anche ad altri motori) che sono state oggetto di studio, sviluppo e sperimentazione durante il triennio del dottorato di ricerca.

I campi di applicazione interessati sono quelli del controllo di motori sincroni a magneti permanenti interni, dell'automotive, della comunicazione con onde convogliate su cavi di potenza per azionamenti, nonché del controllo a microprocessore di azionamenti elettrici per applicazioni civili.

Tutti i lavori svolti sono supportati da verifiche sperimentali i cui risultati sono illustrati nei vari capitoli della tesi.

Abstract

Electrical drives, nowadays, are quickly spreading in various emerging mechatronic applications, such as robotics, precision motion control, servo–drives for medical applications, hybrid vehicles, industrial automation and many more. This implies stringent requirements in terms of reliability and system overall performance.

Special care in design electrical machines and suitable attention in system modelling and implementing control strategy, can improve dynamic response, increase drives lifetime and achieving also costs reduction.

In the first part, this doctoral dissertation deals with modelling permanent magnet synchronous motors, starting from key–concepts arriving to the description of a fundamental measures set in order to characterize the model.

To this aim, a test bench has been developed as useful tool for experimental validation after the design or simulation processes, as well as for a specific support for motor characterization during control design.

In this way, it is possible to prepare a detailed mathematical model, fundamental tool in studying of advanced control strategies.

The test bench is totally automated in executing measure, in order to guarantee measure repeatability.

In the second part, this thesis describes some electrical drive applications with permanent magnet synchronous motors (some applications are suitable also for other type of motors) which have been studied, developed and experimented during the three–year doctoral research.

Some main field interested are: control of interior permanent magnet motors, automotive, power line communication applied to electrical drives, as well as civil applications of drives controlled with microprocessors.

All works performed have been supported by experimental validations whose results have been illustrated on the next thesis chapters.

Chapter 1

Introduction

Nowaday Permanent Magnets Motors are used in many applications where high torque density, high efficiency and precision in control are required.
To achieve the afterward performances, innovative and sophisticated controls, that need an optimal model of the motor, are often used.
In addition, electrical drives are spreading also in field of automation systems and communication features are therefore part of the systems and can be considered an action which reduces costs and improves reliability.
Hereafter, some details on the advanced topics on motor drives for emerging mechatronic applications will be give.

1.1 More–Electric Vehicles

In last fews years, there is a worldwide trend to use more and more electrical driven auxiliaries and to replace the hydraulic and mechanical actuators by electromechanical ones. There are two main reasons for this effort: the reduction of the fuel consumption and the increase of the travel comfort.

The electrical generators, that are used today on cars, have a maximum rated output of about 3 kW. However this power is increasing to meet the future on–board power demand of approximately 6 kW to 10 kW. On the other hand, this increased power demand leads to an electrical machine with a torque that is in the range of the starting torque demand of a big car combustion engine.

As a consequence of that, both starting and generation requirements can be carried out by a single electrical machine. Such an electrical machine can be either coupled directly to the crankshaft or coupled by means of a belt. This type of electrical machine is called an Integrated Starter–Alternator (ISA). As shown in the figure 1.1 which is the cross–section of an hybrid vehicle engine,

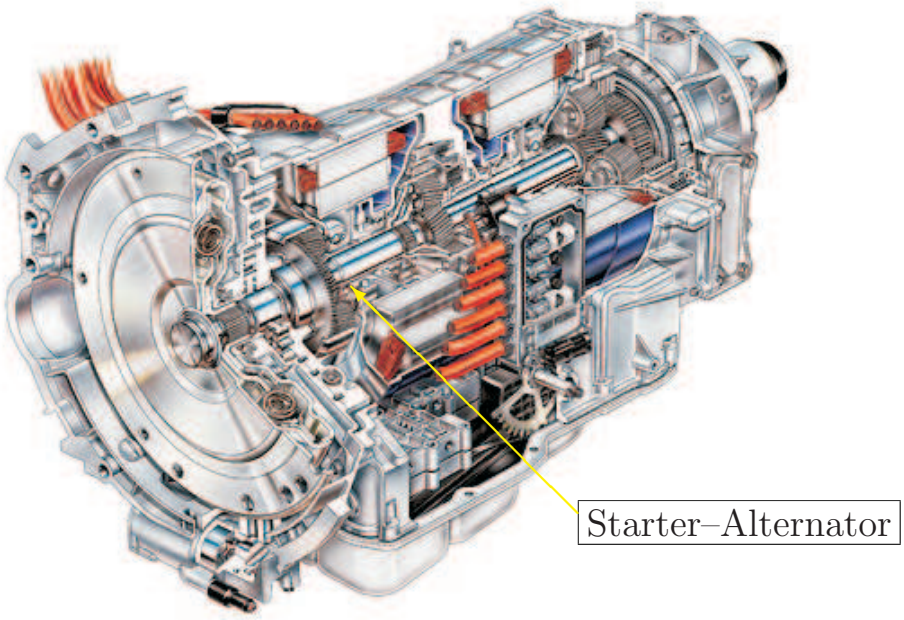

Figure 1.1: Cross-section of hybrid vehicle engine

one can evince that ISA can be considered to be the central component of future board power systems.

A part of this thesis describes the control strategy of an ISA prototype, so as to achieve a high starting torque as well as a high efficiency up to the maximum speed during the generation operations. The adopted electrical machine is an interior permanent magnet machine with a fractional–slot winding. The control strategy takes advantage of the magnetic model of the electrical machine, which is well suited for flux–weakening application.

1.2 Direct Drives

In a Direct Drive (DD) system, the motor drives its load without a reduction gearbox, lube oil systems or ball screws. Consequently, this leads to a simple mechanical structure and high stiffness products. Moreover, the problems of friction, joint clearance, wear, and low efficiency are greatly reduced.
Because of the lack of the gear, disturbances from load are now transmitted directly to the motor. A well designed controller that should be robust and free from noise is needed. Furthermore, the load inertia also affects significantly the overall inertia of the system because it is not reduced by the gear ratio.

Nowadays, DD systems are a new phase in electrical rotating equipment technology and allows electrical machines to rotate at a speed which matching the angular rotation of the load (e.g. centrifugal compressors, steam and gas turbines).

Some advantages given by this technology are:

- Increased efficiency: the power is not wasted in friction, i.e.from the belt, chain and especially, gearboxes.
- Reduced noise: being a simpler device, a direct-drive mechanism has fewer parts which could vibrate, and the overall noise emission of the system is usually lower.
- Longer lifetime: the few quantities of moving parts means having no more parts prone to failure. Failures in other systems are usually produced by aging of the component (such as a stretched belt), or stress.

On the other hand, some disadvantages are:

- needs of a special motor specifically design for the application. Usually motors are built to achieve maximum torque at high rotational speeds, usually 1500 *rpm* or 3000 *rpm*. While this is useful for many applications (such as an electric fan), other mechanisms need a relatively high torque at very low speeds, such as a turntable, which needs a constant (and very precise) 33 1/3 rpm or 45 rpm. A 1500 rpm motor couldn't even start rotating if fed the necessary voltage to make it spin at 33 rpm, and it wouldn't be precise keeping that speed.
- The slow motor also needs to be physically larger than its faster counterpart. On a direct-drive turntable, the motor is about 4 *inch* (10 *cm*).
- Direct-drive mechanisms need a more precise control mechanism. Low voltage variations on a high-speed motor, which is reduced to low rpm can go unnoticed, but in a direct-drive, those variations are directly reflected on the rotational speed.

The fields of application have been grown in the last decade. Some common applications are:

- Washing machine: *Toshiba*® released direct-drive washing machine on the market in 1997. Other manufacturer also introduced a washing machine which drives the drum with a direct-drive motor in spring of 2006.
- Train: *East Japan Railway Company (JR East*® *)* built an experimental `E993` series Electric Multiple-Unit (EMU) called the 'AC Train' in January 2002 to test the feasibility of direct-drive motors on commuter trains.

- Lift equipment: modern elevator systems are more and more comfortable people mobility equipment, widely diffused. They require high efficiency and soft motion features. In addition, some lift manufacturers have been developed a product line with its 'Roomless' equipment, characterized by the lack of the machinery space over the lift tunnel, with some advantages about costs and feasibility of systems installation in particular building. Moreover, rope elasticity plays also an important role in the system dynamic.

1.3 Remote applications

Power line communication (PLCom) techniques seem a worthwhile research issue not only in civil applications, but also into the industrial scenario. The realization of a communication network using the already existing electrical network is attractive for cost benefits, even though it represents a real challenge.
Major problems concern communication reliability, effectiveness of transmission modulation methods and algorithms for error correction. EMC issues also must be taken into account, considering the consequences of injecting high-frequency harmonics into the AC power distribution system.
An important field of application of PLCom techniques is its study in harsh and noisy environment of electrical drives. This research activity points out how the improvements in communication reliability can be achieved not only by a smart choice of the communication protocol, but also by using proper inverter modulation techniques, as Random Space Vector Modulation (RSVM). There are some results coming from the experimental results of transmission tests which explain the comparison of transmission tests with both conventional and random space vector modulation techniques.

1.4 Thesis outline

This doctoral dissertation is divided into two major parts: the first one gives a brief introduction to the key concepts in order to give a scientific background about the topics treated on next chapters. Afterwards, the second part is an exposition of some applications developed during the research activity.

After this Introduction Chapter, the chapter-sharing is proposed as follow:

- Chapter 2 reviews some concept about Permanent Magnet Synchronous motor, starting from base equations arriving to Maximum Torque per Amps curve description. A Motor Test–bench system is next reported as part of the research activities.

- Chapter 3 discusses different cases of application of Permanent Magnet Synchronous Motor in actual systems. This part describes the results of theory application.
  An advanced model, considering the rope elasticity of a direct-drive lift system is studied as the first application.
  Then, a particular self-tuning method of Maximum Torque per Amps loci, using injection of high frequency signals is evaluated.
  Power line communication is the next subject presented.
  At the end, a particular control method of a Starter-Alternator integrated in a vehicle engine is presented.
  All the cases reported in this chapter have been carried out in equivalent paper.

- Chapter 4 summarizes the conclusions of the work and provides some proposals for further research.

Chapter 2

Permanent Magnet Motors

2.1 Overview

With their high efficiency, high power density and elevated torque-to-inertia ratio, Permanent Magnet (PM) machines are a common choice in a wide range of application where the electrical–to–mechanical energy conversion is needed, such as electrical o hybrid vehicles, manufacturing process and many more.
Depending on the ElectroMotive Force (EMF) waveform, PM motor are divided into:

- *brushless dc machines* (BLDC) which have trapezoidal EMF (trapezoidal BL motors) and are fed with rectangular currents form;
- *permanent magnet synchronous machines* (PMSM) which have sinusoidal EMF (sinusoidal BL motors) and are fed with sinusoidal–shape currents.

Usually, the name *PM motors* indicates the Permanent Magnet synchronous motor (PMSM).
As pointed out above, the use of the permanent magnet (PM) in construction of electric machines can yield some benefits, i.e. energy saving (no excitation losses), high torque per volume ratio, high dynamic performance (low rotor inertia), simplification of construction and maintenance, and at last (but not the least) the price reduction when the machine design do not imply peculiarity. Trapezoidal PM brushless machines are more attractive in drive applications that can take advantage of the simple controls and minimum sensors requirement, but paying an higher torque ripple. One more weakness of the trapezoidal type is its more limited speed range in the constant power region compared to a sinusoidal PM brushless machine properly designed to achieve such a feature.

Constraint of maximum dynamic response requested by some applications makes the use of PMSM mandatory, e.g. machine tool servos and robotic actuator drives.

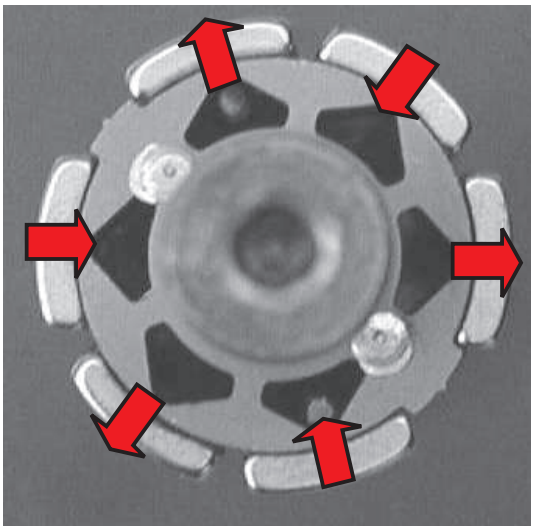

Figure 2.1: Permanent Magnet Synchronous Motor

The Magnet materials are mostly rare-earths, such as NdFeB[1] or SmCo[2], which make it possible to reduce both the machine size and the rotor inertia.
Considering the present pollution and energy consumption the use of PMSM with their high efficiency performance would be a way to share the help to solve in part that problem.

The growing of the possible fields where using Permanent Magnet Synchronous Motor, make this type of motor an attractive choice and requires more accurate control method and high reliability of power electronics.

2.2 Drive modelling

Depending on the spatial position of permanent magnet, PMSM can be divided in two big categories:

- *Surface Permanent Magnet* (SPM) Synchronous Machines
- *Interior Permanent Magnet* (IPM) Synchronous Machines

As visible in figure 2.2, in SPM motors the magnet are mounted (usually glued) on the rotor surface and the shape of the magnet follows the outline of the rotor cylinder.

On the other hand, the IPM rotor depicted in figure 2.3, has the magnet positioned inside the rotor volume.

This different position of permanent magnet, considering the path of magnetic flux, imply a different saliency.

[1]Neodymium Iron Boron magnets are alloys of the Lanthanide group of elements.
[2]Samarium Cobalt is alloy of the Lanthanide group of elements.

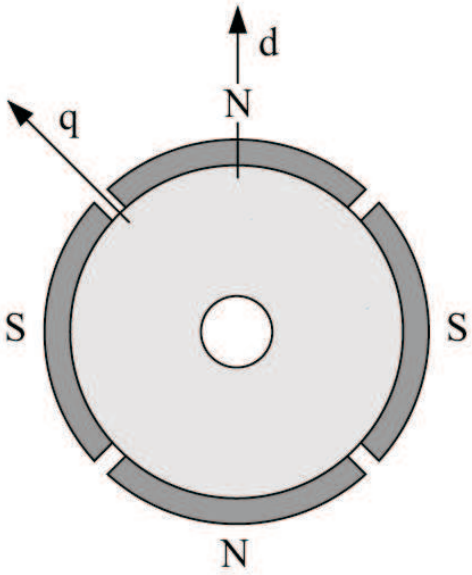

Figure 2.2: Surface mounted permanent magnet (SPM)

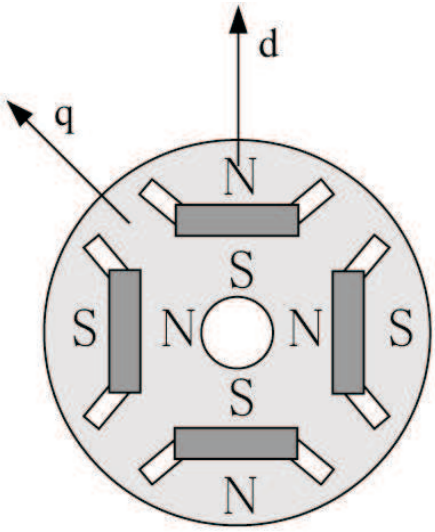

Figure 2.3: Interior permanent magnet (IPM)

SPM motor presents an isotropic rotor; in this case, the electro-mechanical energy conversion applies the principle of electro-dynamic systems, which have stator and rotor with windings, both fed by currents.
On the other hand, IPM motors exhibit rotors with elevated anisotropic magnetic path. In this situation, the electro-mechanical energy conversion follows both the principle of electro-dynamic systems and reluctance systems. This causes the presence of some difference regarding motor equations and a varia-

tion about the supply of the stator windings.
More details on next paragraphs.

2.2.1 IPM motor equations (with saturation)

For describing and analyzing a sinusoidal Permanent Magnet synchronous motor, the most convenient way is to consider a synchronous-rotating reference frame fixed to the rotor [1]. A d– and q– motor model is obtained and used on next paragraphs of the thesis.

Referring to the figure 2.3, the direct axis (marked with label 'd') is aligned with the permanent magnet flux linkage phasor $\overrightarrow{\Lambda}_{mg}$. With a phase displacemnt of 90 electrical-degree (thus orthogonal with d–axis) there is the quadrature axis (marked with label 'q'); it is aligned with the resulting back-emf phasor $\overrightarrow{E}$.

Under steady-state, the value of magnitude of back-emf vector can be expressed by the following equation:

$$E = p \cdot \Omega_m \cdot \Lambda_{mg} = \Omega_{me} \cdot \Lambda_{mg} \tag{2.1}$$

where p indicates the pole pairs, Ω_m is the rotor angular speed, expressed in radians per seconds[3], and Λ_{mg} represents the magnet flux linkage amplitude in $V \cdot s$.

The transformation of the state variables (voltages, currents and fluxes) from the stationary frame (a, b, c) into the rotating d– and q– coordinates, is done using the amplitude-invariant (power–variant) transformation matrix reported below:

$$\begin{bmatrix} d \\ q \end{bmatrix} = \frac{2}{3} \begin{bmatrix} \cos\vartheta_{dq} & \cos(\vartheta_{dq} - \frac{2\pi}{3}) & \cos(\vartheta_{dq} + \frac{2\pi}{3}) \\ -\sin\vartheta_{dq} & -\sin(\vartheta_{dq} - \frac{2\pi}{3}) & -\sin(\vartheta_{dq} + \frac{2\pi}{3}) \end{bmatrix} \cdot \begin{bmatrix} a \\ b \\ c \end{bmatrix} \tag{2.2}$$

where ϑ_{dq} corresponds with the electro–mechanical angle ϑ_{me} in synchronous machines. The lack of power invariance of transformation adopted implies the presence of a coefficient $\frac{3}{2}$ which multiplies the torque expression.

[3]Due to the elevated number of pole in actual sinusoidal machines, in a complete mechanical turn of 2π radians the electrical quantities run more quickly and complete a period many times as the number of pole pairs. For that reason, a period is measured in *electrical-radians* and the electrical angular is indicated as ω_{me}.

Taking into account the magnetic saturation on magnetic circuits, one can obtain the *dq–frame* electric equations of the motor, considering the flux linkages as state variables [2, Ch. 8]:

$$\begin{cases} u_d &= R \cdot i_d + \dfrac{d\lambda_d}{dt} - \omega_{me}\lambda_q \\ u_q &= R \cdot i_q + \dfrac{d\lambda_q}{dt} + \omega_{me}\lambda_d \end{cases} \tag{2.3}$$

where u_d and u_q are d- and q-axis stator voltage components, R is the stator resistance, i_d and i_q are d- and q-axis stator current components, λ_d and λ_q are d- and q-axis stator flux linkage components, $\omega_{me} = p\omega_m$ is the rotor electromechanical speed, p is the number of pole pairs and, at the end, ω is rotor mechanical speed.

As suggested before, applying both the principle of electro-dynamic systems and variable reluctance systems in electro-mechanical energy conversion, the electromagnetic torque is obtained[4]:

$$M = \frac{3}{2} p \cdot (\lambda_d \cdot i_q - \lambda_q \cdot i_d) \tag{2.4}$$

Equation 2.4 provides the average electromechanical torque. Harmonics torque components[5] (e.g. given by a non sine-distributed windings) are not take into account by the 2.4.

Since the d– and q– component flux linkages are both function of d– and q–axis current components, the interaction between the two axes, due to the magnetic saturation, appear as a *magnetic cross-coupling*[6].
As known [2], that magnetic cross-coupling is due to the shared path between the two flux linkage component (d- and q-axis) and the non-linear behaviour of the ferromagnetic material.

However, multi-barrier IPM motors, such as used in the experimental works of this thesis (refer to Chapter 3), have point out that magnetic cross-coupling can be neglected. Mutual- and auto-inductance provided by the magnetic circuit are considered in a parameter called *synchronous inductance* and indicated with the symbol L.
In IPM motor, the synchronous inductance depends of the rotor position: considering the transformation given by equation 2.2 it follows that two inductance value are defined:

[4] Performing an energy balance and assuming sine-distributed windings.
[5] Causing the cogging torque.
[6] Also called *cross-saturation*.

- L_d as the direct synchronous inductance, runs by direct current i_d;
- L_q as the quadrature synchronous inductance, runs by quadrature current i_q.

Motor equations (considering the iron saturation) can be given in a generic form such as equation 2.5.

$$\begin{cases} u_d &= R \cdot i_d + \dfrac{d\lambda_d(i_d)}{di_d} \cdot \dfrac{di_d}{dt} - \omega_{me} L_q(i_q) \cdot i_q \\ u_q &= R \cdot i_q + \dfrac{d\lambda(i_q)}{di_q} \cdot \dfrac{di_q}{dt} + \omega_{me}[L_d(i_d) \cdot i_d + \Lambda_{mg}] \end{cases} \tag{2.5}$$

It's allowed to assume L_q as function of only the q-axis current component i_q, while L_d can be treated as constant value [2, Ch. 10].
With this assumption, the flux linkages are given by:

$$\begin{cases} \lambda_d &= L_d i_d + \Lambda_{mg} \\ \lambda_q &= L_q(i_q) \cdot i_q \end{cases} \tag{2.6}$$

where Λ_{mg} is the constant flux linkage component given by the permanent magnets (PMs).

Considering the variation of inductance value, as assumed above, one can obtain the electrical equations of the motor by considering the currents as state variables:

$$\begin{cases} u_d &= R \cdot i_d + L_d \dfrac{di_d}{dt} - \omega_{me} L_q(i_q) \cdot i_q \\ u_q &= R \cdot i_q + \dfrac{d\lambda_q(i_q)}{di_q} \cdot \dfrac{di_q}{dt} + \omega_{me}(L_d i_d + \Lambda_{mg}) \end{cases} \tag{2.7}$$

Also the torque equation can be rewritten as a function of the currents only:

$$M = \frac{3}{2} p \cdot [\Lambda_{mg} i_q + (L_d - L_q(i_q)) i_d i_q] \tag{2.8}$$

The current vector can be represented by the d- and q-axis currents i_d and i_q or by the amplitude I and the phase angle β.
The torque equation 2.8 become:

$$M = \frac{3}{2} p \cdot \left[\Lambda_{mg} I \cos\beta + \frac{1}{2}(L_d - L_q(i_q)) I^2 \sin(2\beta) \right] \tag{2.9}$$

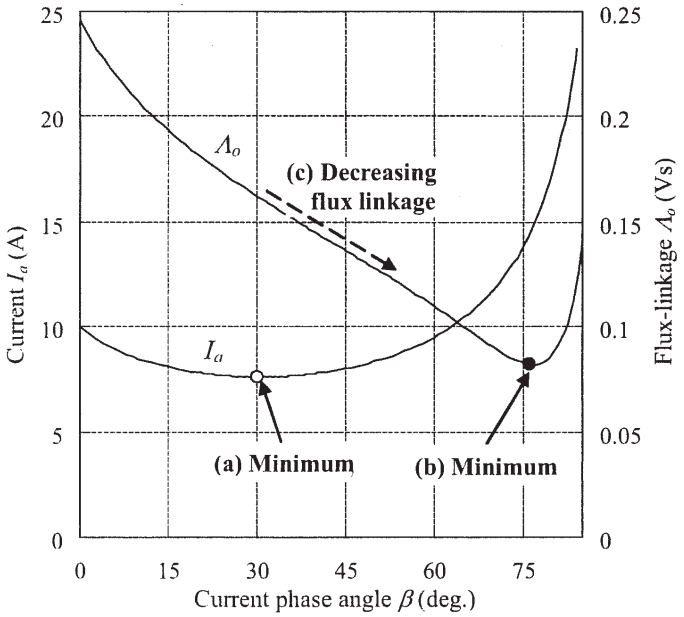

Figure 2.4: Current phase angle β vs. current magnitude I_a

Figure 2.4 shows the magnitude of current and flux linkage as functions of current phase angle. This is given under the constant torque condition.
Appear immediately the presence of a value of current phase angle which corresponds to a minimum current magnitude for an operating working point. Under this current value, the torque becomes the maximum. This feature justifies the maximum torque–per–ampere control [3].
Moreover, increasing the current phase angle β, the flux linkage Λ_0[7] decrease until it reaches a minimum value under the same torque. This working condition allows a maximum torque–per–flux control. At this same condition the electro–magnetic force[8] is minimized. The flux linkage decreasing during current phase angle rising leads the Flux–Weakening (FW) control.

Equation 2.9 is more important because it will be very useful on next paragraph consideration.

As approximations of (2.8), neglecting the saturation phenomena, give the well known expression of IPM motor electromechanical torque average value:

$$M = \frac{3}{2} p \cdot [\Lambda_{mg} i_q + (L_d - L_q) i_d i_q] \tag{2.10}$$

[7] $\Lambda_0 = \sqrt{\Lambda_d^2 + \Lambda_q^2}$ indicates the whole flux linkage on the machine.
[8] EMF.

with both L_d and L_q considered constants.
From (2.10), one can obtain the constant torque curves drawn as hyperbola having the i_d-axis and the vertical line $i_d = \Lambda_{mg}/(L_q - L_d)$ as asymptotes.

2.2.2 SPM motor equations (with saturation)

Alternate current Synchronous Motors with permanent magnets glued on the surface, present an isotropic magnetic behaviour about the flux linkage paths. Under this symmetrical considerations, mutual- and auto-inductance presented by the magnetic circuits covered by the flux linkages are amounted together defining the *synchronous inductance* which does not depends on the rotor position.
A four pole SPM rotor is shown in figure 2.2, where are visible d- and q-axis, relatives to transformation indicated with equations 2.2.

Under this usual representation,

$$\begin{cases} u_d &= R \cdot i_d + \dfrac{d\lambda_d}{dt} - \omega_{me}\lambda_q \\ u_q &= R \cdot i_q + \dfrac{d\lambda_q}{dt} + \omega_{me}\lambda_d \end{cases} \tag{2.11}$$

where u_d and u_q are d- and q-axis stator voltage components, R is the stator resistance, i_d and i_q are d- and q-axis stator current components, λ_d and λ_q are d- and q-axis stator flux linkage components, $\omega_{me} = p\omega_m$ is the rotor electromechanical speed, p is the number of pole pairs and, at the end, ω_m is rotor mechanical speed.

In the situation of isotropic rotor structure, the flux linkages are defined as follow:

$$\begin{cases} \lambda_d &= L \cdot i_d + \Lambda_{mg} \\ \lambda_q &= L \cdot i_q \end{cases} \tag{2.12}$$

where Λ_{mg} is the constant flux linkage component given by the permanent magnets and L is the synchronous inductance.
The presence of iron saturation phenomenon implies a small saliency and, as a consequence, the necessity of considering two different inductances L_d and L_q which depend of the rotor position. From this point, the treatment is the same explained on previous paragraph for IPM motor.

SPM motor equation, using current components as state variable and considering the magnetic saturation can be rewritten from 2.11 as:

$$\begin{cases} u_d &= R \cdot i_d + L \cdot \dfrac{di_d}{dt} - \omega_{me} L i_q \\ u_q &= R \cdot i_q + L \cdot \dfrac{di_q}{dt} + \omega_{me} \cdot [L \cdot i_d + \Lambda_{mg}] \end{cases} \tag{2.13}$$

As perform during the computation of equation 2.4 electro-mechanical energy balance is applied using (2.13) in order to obtain the electromechanical average torque value provided by an SPM motor.
In this type of rotor, the isotropic behaviour imply the presence of the only electro-dynamic systems principle. Torque drawn out by 2.14 is composed by a single addendum:

$$M = \frac{3}{2} p \Lambda_{mg} \cdot i_q \tag{2.14}$$

The presence of the coefficient $\frac{3}{2}$ is due to the power invariant transformation adopted (2.2)in order to transfer from steady-state reference frame to the synchronous one, which is not power-invariant.
Moreover, in the electro-mechanical torque equation 2.14 does not appear the dependence from the inductance value.

Discussion given in this paragraph will be useful in some considerations about the lift system treatment in Section 3.1.

2.2.3 Limits

Possible voltages and currents applicable to feed a PM motor have to remain within specific values. Values are provided by the manufacturer in order to keep the device and allow long life to it.

Considering an IPM motor and working at steady-state[9], currents written as magnitude and phase angle as equation 2.9, may to comply with:

$$I = \sqrt{I_d^2 + I_q^2} \leq I_N \tag{2.15}$$

[9]Capitalized letters are used to indicate constant values or quantity with very slow variation.

where I_N is the nominal current limit as continuous rating in the continuous operation. This limit can be exceeded for short time and repeated with a duty-cycle[10].

As the same way, is possible to explain the voltage constraint:

$$U = \sqrt{U_d^2 + U_q^2} \leq U_N \tag{2.16}$$

where U_N is a maximum available output voltage of the inverter, which depends on the dc-link voltage, indicated with U_{dc}.
Relating currents on Root Mean Square (RMS) values, nominal quantity become

$$I_N = \sqrt{2} \cdot I_{RMS} \tag{2.17}$$

$$U_N = \sqrt{\frac{2}{3}} \cdot U_{RMS} \qquad \text{line–to–line} \tag{2.18}$$

Replacing values of u_d and u_q from equation 2.7, evaluated in steady-state, it results:

$$(\Omega_{em} L_q I_q)^2 + (\Omega_{em} L_d I_d + \Omega_{em} \Lambda_{mg})^2 \leq U_N^2 \tag{2.19}$$

which can be rewritten in different appearance as the following:

$$\left(I_d + \frac{\Lambda_{mg}}{L_d} \right)^2 + \left(\frac{L_q}{L_d} I_q \right)^2 \leq \frac{U_N^2}{\Omega_{em}^2 \cdot L_d^2} \tag{2.20}$$

The critical condition provided by equations 2.15 and 2.20 are respectively the current–limit circle and the voltage–limit ellipse in the i_d–i_q plane. Figure 2.5 shows that limits regions and their intersection.
The voltage–limit ellipse shrinks to the center point `M` increasing the speed.
The current vector satisfying both constraints of voltage, while current must be inside of both the current–limit circle and the voltage–limit ellipse.

The just evaluated voltage and current constraints, is possible to identify the optimum current vector producing the maximum torque at any speed [2].

[10]Manufacturer usually provides also maximum rating values which can not be exceeded for any reasons.

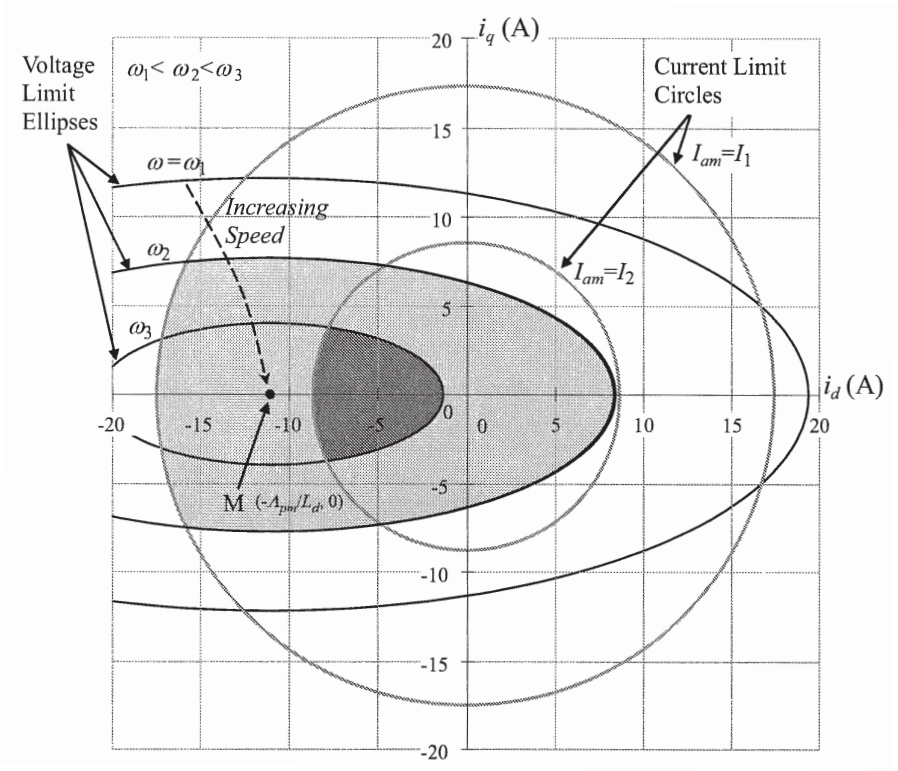

Figure 2.5: Current and Voltage limit for IPM motor in i_d, i_q plane

2.2.4 Regions

On this paragraph, during the discussion, is examined an IPM motor. Current–limit circles and voltage–limit ellipses, treated on previous paragraph and show in figure 2.5, define two operating regions, depending on the speed of the motor shaft:

- *Region I* – Constant torque region.
- *Region II* – Constant power region (FW control).
- *Region III* – Decreasing power region (FW control)

Considering short–circuit current, the center of ellipse can result inside or outside current–limit circle.
If ellipse center falls outside the circle the situation depicted in figure 2.6 appear. Here, the condition given is the follow equation:

$$\Lambda_{mg} - L_d \cdot I_N \tag{2.21}$$

The figure 2.6 also plots the MTPA locus and the point indicated as `'A'`, that corresponds to the point where the motor produce the nominal positive

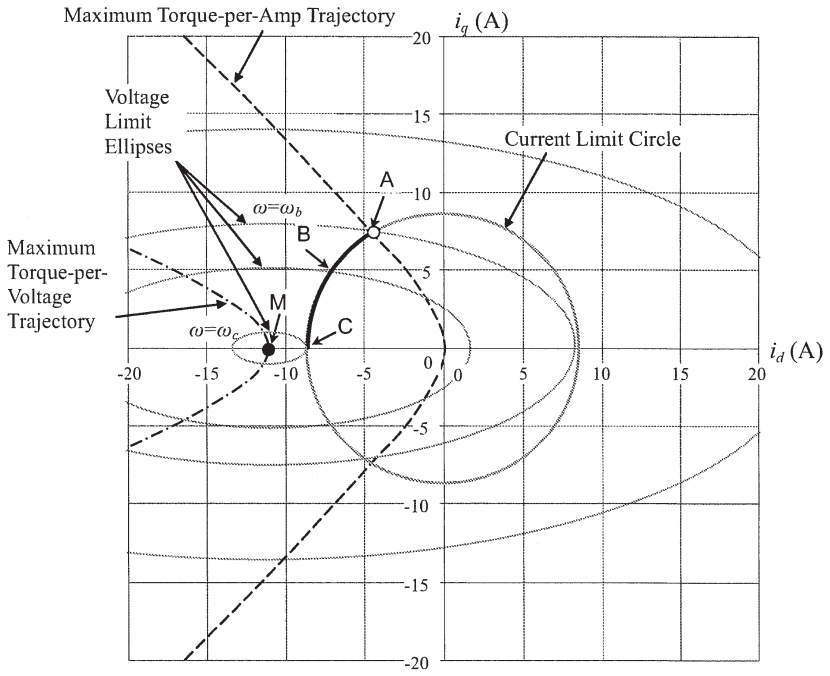

Figure 2.6: Limit on IPM motor with $\Lambda_{mg} - L_d I_N > 0$.

torque at the minimum current.
Negative q–currents half plane, is the specular situation: the nominal negative torque produced with the minimum current.

On the other hand, figure 2.7 represents the opposite case: the ellipse center which falls inside the current limit circle. This case is given with the condition: $\Lambda_{mg} - L_d I_N < 0$.

When the rotor goes at a speed below the base speed Ω_B[11], the motor working points are moving in the constant torque region (indicated as Region I). In this region, the nominal torque is produced with an MTPA control.

Above the base speed, the current vector is controlled by a flux–weakening control. Possible working points should stay in Region II. In this region, the maximum torque is the working point corresponding with the intersection with the voltage–limit and the current–limit, as point `'B'` in figure 2.7.
The maximum torque obtainable is lower than the nominal torque, and it decreases quickly when the speed increases, reaching the null torque at maximum speed given by the following equation, deduced from equation 2.20 when $I_q = 0$

[11]The motor reach the base speed when the corresponding voltage–limit ellipse intersects the current–limit circle.

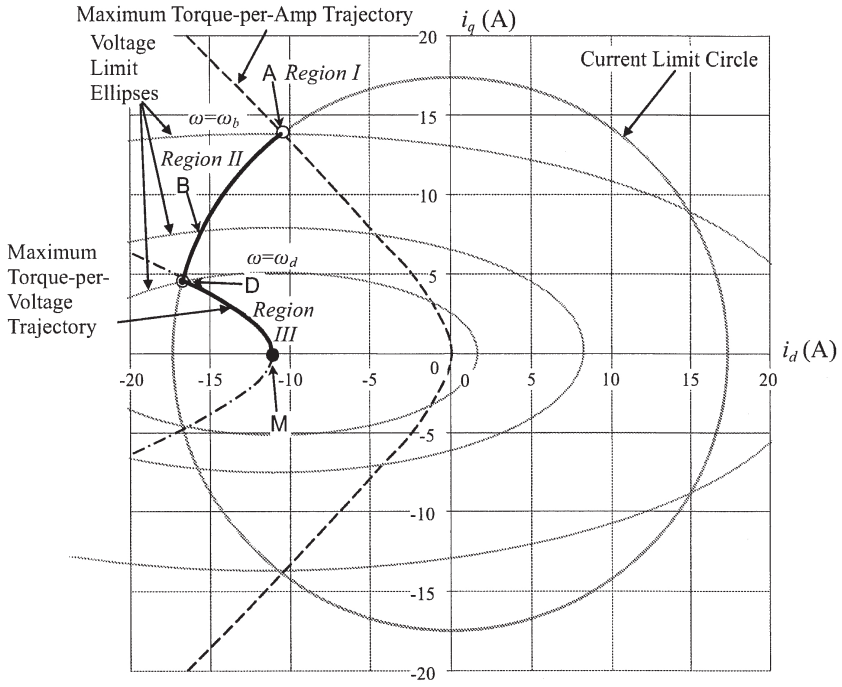

Figure 2.7: Limit on IPM motor with $\Lambda_{mg} - L_d I_N < 0$.

and $I_d = -I_N$:

$$\Omega_{MAX} = \frac{U_N}{\Lambda_{mg} - L_d \cdot I_N} \tag{2.22}$$

Plotting the mechanical characteristics of an IPM motor, is possible to see the results above mentioned. Figure 2.8 shows this mechanical characteristics when $\Lambda_{mg} - L_d I_N > 0$. Regions described before are highlighted.

Considering the case reported in figure 2.6, issues for Region I and Region II remain the same changing only that torque does not go to zero at maximum speed.
When, $\Lambda_{mg} - L_d I_N < 0$ a Maximum Torque Per Voltage (MTPV)[12] control can be applied when the speed overcomes the intersection between the MTPV curve and the current–limit circle. This speed value is indicated as Ω_d in figure 2.6 and the point is called `'D'`.
If the speed increases over Ω_d the possible working points are contained in Region III.

[12]MTPV is the locus which points are the intersection with voltage–limit ellipse and constant torque hyperbolas.

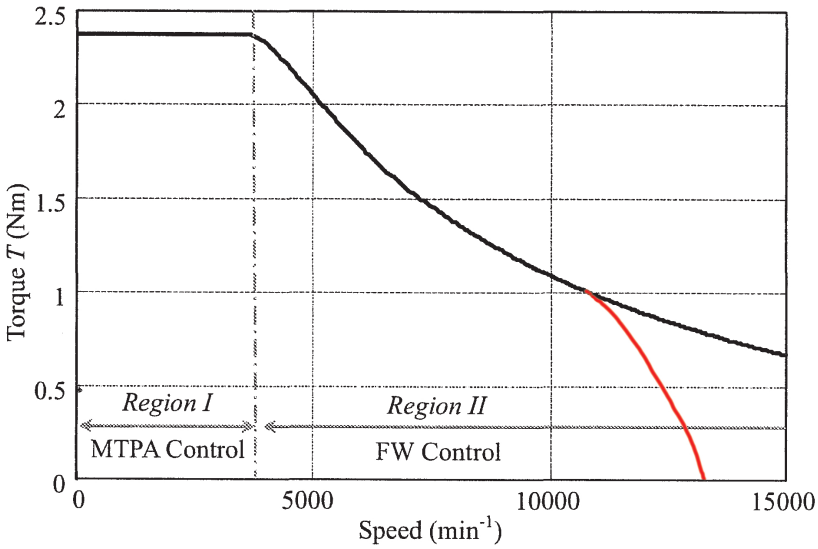

Figure 2.8: Limit on IPM motor with $\Lambda_{mg} - L_d I_N < 0$.

2.2.5 MTPA

The optimal current phase angle at which the torque per current magnitude becomes maximal is derived obtaining the current phase angle β from equation 2.9:

$$\beta = \sin^{-1}\left(\frac{-\Lambda_{mg} + \sqrt{\Lambda_{mg}^2 + 8 \cdot (L_d - L_q)^2 \cdot I_a}}{4 \cdot (L_q - L_d) \cdot I_a}\right) \tag{2.23}$$

For d– vs. q–axis current vector, the MTPA condition is given by following equation:

$$i_d = \frac{\Lambda_{mg}}{2 \cdot (L_d - L_q)} - \sqrt{\frac{\Lambda_{mg}^2}{4 \cdot (L_q - L_d)^2} + i_q^2} \tag{2.24}$$

Equations 2.23 and equation 2.24 are shown in figure 2.9 as maximum torque per ampere trajectory. In this figure are also depicted constant current circles and constant torque loci.
Is known that MTPA curve is the locus of tangent points from constant torque loci with constant current circles, in figure indicated as P_1, P_2, P_3.
As consequence, the maximum available torque is obtained producing a current vector corresponding with maximum torque per ampere points[13].

[13]Considering the current limit.

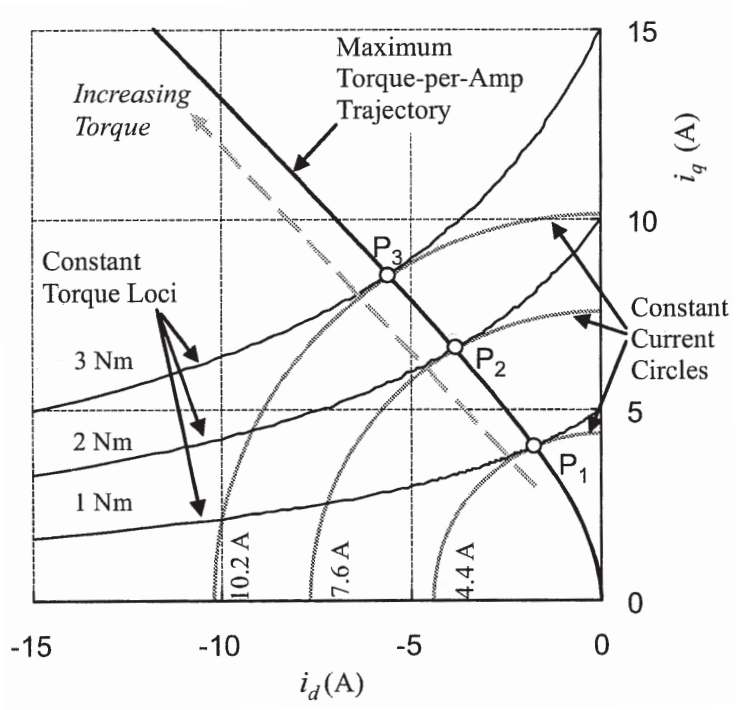

Figure 2.9: Current vector trajectory for MTPA control

The only $i_d < 0$ and $i_q > 0$ values are plotted in figure 2.9, considering that characteristics curves are symmetry with d–axis. For negative torque, region with both d– and q–current negative is used.

For SPM motors, neglecting iron saturation, because of auto–inductance on d–axis corresponds with the q–axis one ($L_d = L_q = L$) the Maximum Torque Per Ampere working points stays in q–axis.
Therefore, feeding SPM motors in MTPA condition is reachable setting i_d current equal to zero.

2.2.6 Cogging

Cogging torque of PM motors is due to the interaction between the permanent magnets of the rotor and the stator slots opening. Also called as detent or 'no-current' torque, it is an undesirable component for the operation of such a motor. It is especially prominent at lower speeds, with the feeling of jerkiness.

Presence of cogging torque involves some problems, in particular when the mechanical load needs a flat torque.
There are some intervention in order to reduce, during the motor design. In figure 2.10 are shown various cogging torque simulation results compared each

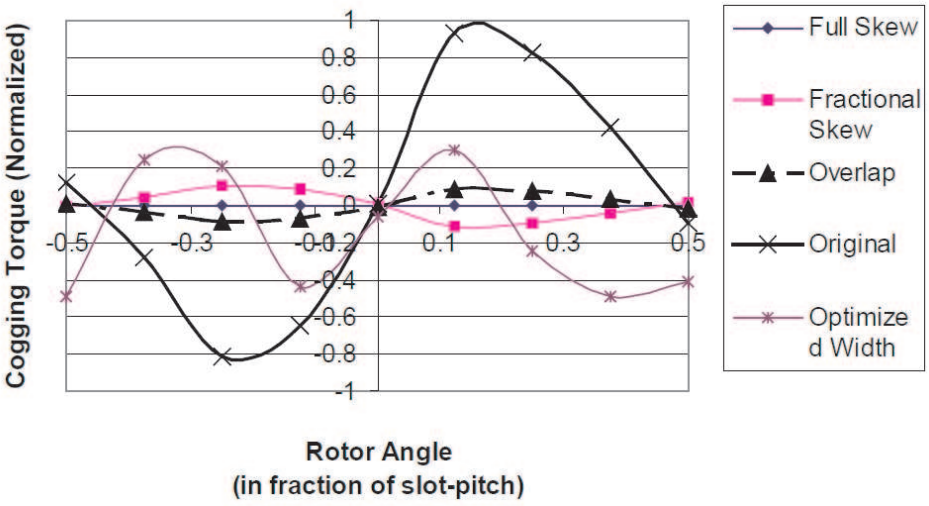

Figure 2.10: Cogging torque as a function of rotor angle at different skewing angle

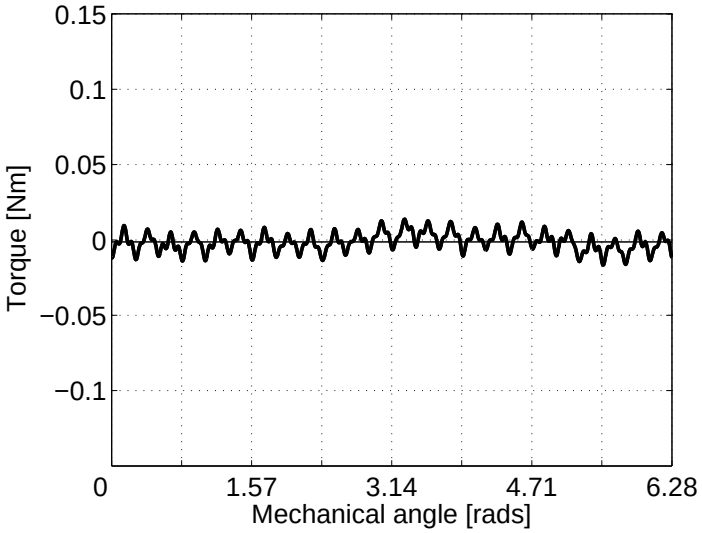

Figure 2.11: Cogging torque measure with a test bench

other.

For a PM motor figure 2.11 shows a cogging torque measured with a test bench.

This effect which is compared with a noise signal in control strategy, may cause some instability and, in some cases, should be necessary to know the frequency value of cogging torque, in order to properly design the control loops.

2.3 Test on PM motors

As a concluding phase of the development of new electromechanical machines, an accurate characterization should be a mandatory step just after the design procedure.
In such a case the goal is the confirmation of the designed motor performance and/or the justification of some discrepancy between specifications and experimental results.
A set of measurements has to be performed during this test phase [4], [5].

One more purpose of motor characterization is a requirement in developing innovative and sophisticated control systems, in order to accurately tune the control algorithms or, in a previous stage, to check the control feasibility.

During the research activities illustrated in present thesis, a couple of test benches have been developed to perform the following measurements on PM motors:

- Quasi–static torque characterizations.
- Dynamic tests with high speed.

Both test benches have been connected to the same Personal Computer (PC) (the Measure Point), to store and compute measured value. Also the currents that feed the motor under test are controlled in hysteretic mode, so that any current waveform is theoretically possible, regardless on motor parameters.
The Measure Point is widely automated and programmable, to derive the most important motor parameters as well as characteristic curves of the motor under test (MuT), as flux–current curves and torque–current curves. It is equipped with MATLAB® and an acquisition board produced by DSpace® manufacturer.

For quasi–static measurement the test bench is equipped with an irreversible gearbox to reduce and stabilize the speed of the motor under test.
The following test procedure can be implemented in this bench equipment (for definition and terminology see [6]):

- *d– and q–axis automated detection* – It consists in determining the position of the polar axis of the MuT with respect to a zero position of the incremental encoder. This is an indispensable measurement preliminary to all the other tests.
- *Flux-current magnetization curves* – It is the measurement of the flux vs. current relationship for both d- and q-axis including saturation and cross-coupling effect.

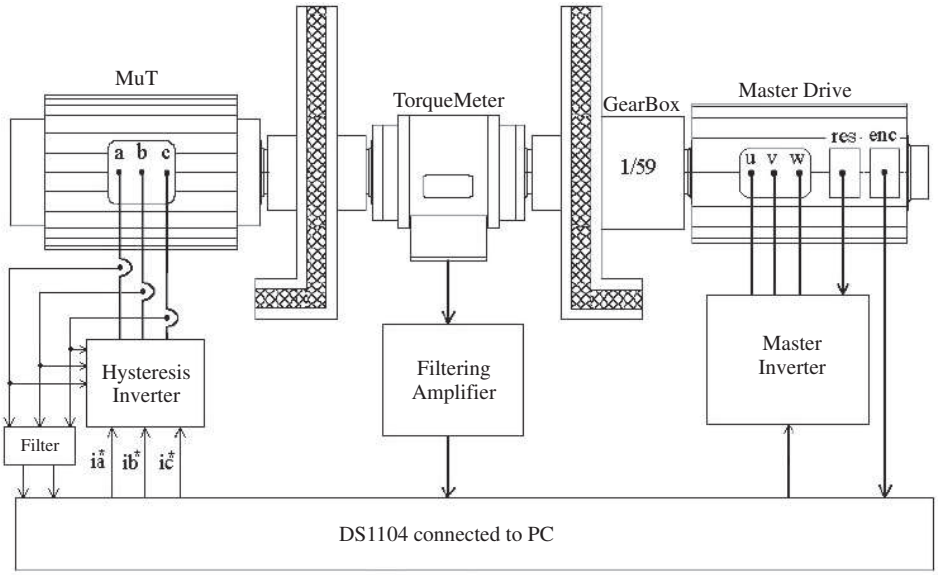

Figure 2.12: Quasi–static Test Bench schematic

- *PM cogging torque* – It is the measurement of the torque due to the interaction of PM pole edges on the rotor and slotting of the stator, while the stator is not energized.

- *Torque at given d– and q–current* – It consists in measuring the relationship $M = M(\vartheta_m)$ for given fixed current, ϑ_m being the rotor (polar axis) position with respect to axis of phase a.

- *Torque mapping in i_d and i_q plane and derivation of the maximum torque per amps (MTPA) locus* – The measure allow a map of the torque in the d– and q–axis current plane to be obtained.

2.3.1 Low speed test bench configuration

The configuration regarding the quasi–static, low speed characterization is shown in figure 2.12, as schematic of the low speed version. The system is made up of two motors: the *Master Drive Motor* (MDM) and the *Motor under Test* (MuT). An irreversible gearbox with a gear ratio 1:59 is inserted between motors. The shafts are connected by a joint with high torsional rigidity and a torque meter. As introduced above, the test bench includes a PC equipped with MATLAB® (for pre-processing and post-processing) and a dSpace DS1104 board for real-time acquisition and control. Data measured with DS1104 are passed to MATLAB® which get out the required post-processing.

Master Drive and Gearbox

The Master Drive Motor consists of a brushless motor controlled by a three-phase inverter with a speed regulation which provide a constant and controlled speed on the shaft to drag the motor under test. The set point is supplied by the dSpace interface via RS485 bus, because the speed is calculated by the software developed and resident on the DSP in the dSpace interface.
The Master Drive Motor used in the test bench is an SPM synchronous motor with a power of 1.24 kW at nominal speed of 3000 rpm.
In order to reduce the speed on the MuT (low speed shaft) and carry out a torque multiplication a gearbox with a ratio of 1:59 is fitted after the MDM (high speed shaft). This also assures that, fluctuation of speed caused by the MuT torque oscillations can be in practice eliminated and a very constant low speed is assured as required by some motor tests. The maximum speed at which the MuT can be driven is:

$$\omega_{slave_{MAX}} = \frac{1}{59} \cdot \omega_{master_{MAX}} \simeq 50\ rpm \simeq 5.3\ \frac{rad}{s} \tag{2.25}$$

while the maximum continuous torque on the low speed shaft is about 200 Nm in the whole speed range. A feedback of the incremental position of the master shaft is provided by a 1024 ppr encoder mounted in the high speed side. Encoder outputs are acquired by the dSpace system that can compute the incremental position of the low speed shaft (Slave side) with a very high resolution taking into account the gearbox reduction ratio.

Motor under Test

The problem which troubles this part of the test bench is the large variability of MuT that it has to manage. To allow that, the three-phase inverter that feeds the MuT is directed by a hysteresis current control board whose current references are provided by the dSpace software. Hysteresis algorithm assures a fast and precise current control, also robust to motor parameter variation, for any type of motor. The MuT currents are measured with three Hall-effect current sensors whose output signals are acquired by the current control board which performs the hysteresis current control. Since only three-wire motors are foreseen, the motor currents have necessarily to meet the condition:

$$i_a + i_b + i_c = 0 \tag{2.26}$$

Special strategies are thus incorporated into the control board to remove any homopolar components from the current measures and to allow the hysteresis control to work properly. As far as the power stage is concerned, the power switches are at present designed for 16 A continuous currents, that

means a Volt-Amp rating of the MuT of about 7.5 kVA at 400 V_{rms} line-to-line. Larger motors can be tested by replacing the actual power stage with a new one of higher size, while the control remain the same.

Torque meter and filtering amplifier

The test bench has been designed to be equipped by a set of torque meter from 1 to 200 Nm. Torque meter is an important component of the test bench. Precision in torque measurements and quality of the signal conditioning determine the performance of the measurement system. The output of the torque meter is acquired by the dSpace real time interface and then given to MATLAB® for post–processing elaboration. This is made through an external amplifiers that equalizes and filters the signal from torque meter to eliminate high frequency noise and provide it to the dSpace analog-to-digital converter input.

dSpace® 1104 real-time acquisition and control board

Any test procedure requires that motor currents with appropriate waveforms are applied to the MuT, sometimes in synchronism with the rotor d– and q–axis. During this action a real-time acquisition of signals from the test bench is executed. This task is performed by a digital board in which current reference generation algorithms, acquisition algorithms and any real–time service algorithms for the test procedure are implemented. Anyway, sampling and analog-to-digital conversion of the field variables, must be connected with position value acquired from the MuT encoder and with current reference values sent to the MuT.
A dSpace 1104 board provides this performance because gives real–time operation in acquisition (analog-to-digital conversion) and in signal generation (digital to analog conversion). This is done by a Digital Signal Processor (DSP) configured in slave mode and a Power PC that control the communications with the PC (firmware download and memory monitor).
The dSpace 1104 is programmed in `ANSI C` language and provides the automatic implementation of a serial monitor which enables the DSP variables visualization in a PC through a graphic interface (figure 2.13). To achieve the described test bench realization, any other acquisition and control system, able to perform a real–time acquisition and other synchronous operation could be used.

Matlab® post-processing

This is the environment where all the post-processing takes place. The test is started by clicking on the dSpace Cockpit, as depicted in figure 2.13. This

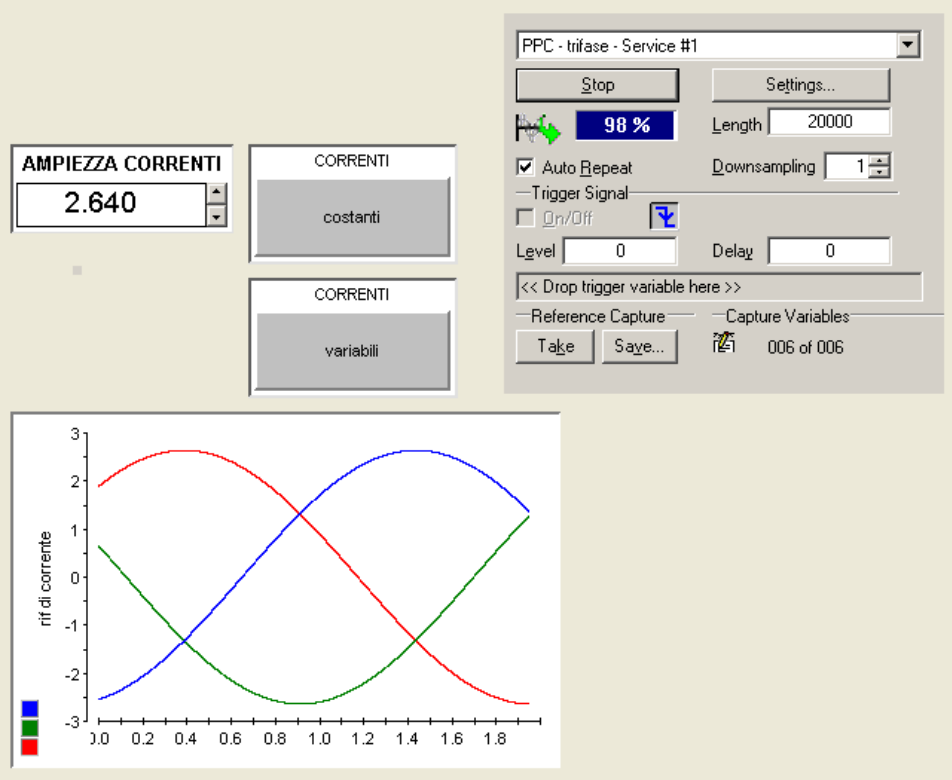

Figure 2.13: Shot of real–time interface provided by dSpace® board

launches the algorithm of the related test as described below. At the end, all data acquired by dSpace board are sent to MatLab via a specific tool called `MTrace`. This library contain some routines invoked from the code, specifically developed for the connection with the dSpace. The compiler on dSpace invokes the real–time routine provided by Matlab. A block diagram which clarify the procedure is reported in figure 2.14.

2.3.2 High speed test bench configuration

The high speed version of the test bench differs from low speed version shown in figure 2.12 for the absence of the gearbox and the use of a Field Oriented Controlled-Induction Motor Drive as Master Drive.
MDM power rating is 5.5 kW with a base speed of 2250 rpm and a maximum speed of the flux weakening region of 2250 rpm. An encoder of 1024 ppr is used as position sensor.

All measures (currents, torque, voltages) are implemented as low speed test bench version. In order to start a test session as high speed motor characteri-

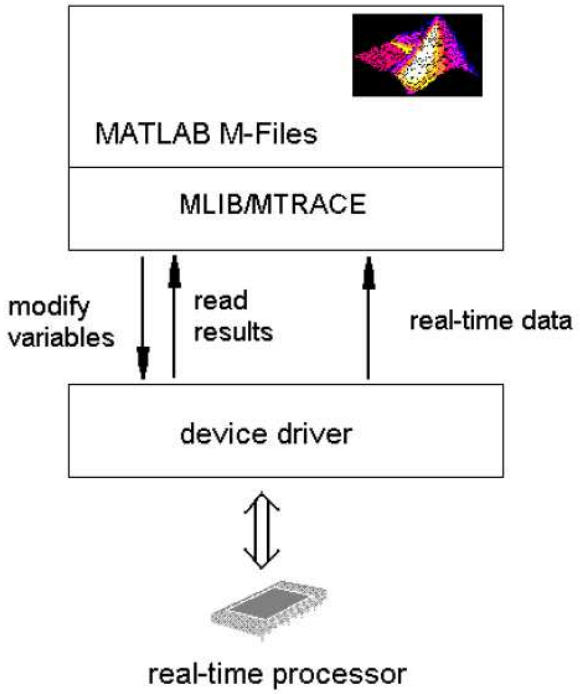

Figure 2.14: MATLAB® real–time via MTrace library structure

zation, commutation onto Master Drive Induction motor is the only operation which has to take place.

2.3.3 Test and Post–Processing Algorithm

In this section, some of the previously listed measures, applied to an IPM and an SPM motors, will be presented. Modelling some motor prototype supporting the control strategy design has been take place with the guide of following examples.

An algorithm developed in MATLAB® environment defines current waveforms and any preset variables according to different the test requirements:

1. A three-phase system of sinusoidal currents;

2. A triplet of constant currents (which can be assumed as a shot of references on previous point.

The dSPACE software receives information on the test to be carried out and accordingly generate the current references for MuT drive and the speed reference for the MDM.

Automatic detection of d– and q–axis

Usually, motors to be tested are not equipped with a rotor position transducer and therefore, after it has been mounted on the test bench, the absolute position of their d– and q–axis have to be detected. This has to be done before any other measure requirements.

Here, a difference between two version of measures. In the high speed test bench, polar axis information can be extracted from the no load back-EMF waveforms measured at the motor terminals while rotor is running at a given speed.
Null value of the polar axis (d–axis) position with respect to axis of phase `a` coincides with negative-slop zero crossing of the back-EMF of phase `a` (assuming a `WYE` connection of the stator phases). In case of distorted back-emf, a Fourier series analysis[14] can be performed and the d–axis position extracted from the fundamental component of the series expansion.
When the neutral point is not accessible, the real component of the stator voltage vector in a stationary reference frame expressed as a function of the line-to-line voltages u_{ab} and u_{cb} according to

$$u_\alpha = \frac{2}{3} \cdot \left[u_{ab} - \frac{1}{2} u_{cb} \right] \tag{2.27}$$

can be used instead of voltage of phase `a`.

On the other hand, in Low Speed test bench[15] rotor position information cannot be derived from the back-emf. However, this information can be found from the behaviour of the torque vs. rotor position under constant stator currents.

Considering the torque equation of a motor with anisotropic rotor:

$$m = \frac{3}{2} \cdot [\lambda_d(i_d, i_q) \cdot i_q + \lambda_q(i_d, i_q) \cdot i_d] \tag{2.28}$$

where p is the number of pole pairs and $\lambda_d(i_d, i_q)$ and $\lambda_q(i_d, i_q)$ are the flux linkages of two fictitious stator phases wound around two rotating orthogonal d– and q–axis and with currents i_d and i_q. If the d–axis is assumed coincident with the polar axis, the q-axis flux linkage meets

$$\lambda_q(i_d, 0) = 0 \tag{2.29}$$

[14] Computed in post–processing mode.
[15] Also in case of pure reluctance machines.

In case of linear magnetic circuit without magnetic cross-coupling effects, neglecting cogging and ripple torques, equation 2.28 can be simplified in:

$$m = \frac{3}{2} p \cdot [\Lambda_{mg} \cdot i_q + (L_d - L_q) \cdot i_d i_q] \tag{2.30}$$

with L_d and L_q are the synchronous inductances of the d– and q– stator phases respectively.
Equations 2.28 and 2.29, or 2.30 point out that the torque is null if the q–axis current is null.

Denoting by i_a, i_b and i_c the real phase current of the motor, d– and q–currents can be computed by transformation matrix given previously with equation 2.2[16].

At first step, the MuT is fed by constant currents given by

$$i_a = 0; \qquad i_b = -i_c = I_k \tag{2.31}$$

that corresponds to leave phase `a` open and to feed the MuT through phase `b` and `c`.
Then, applying the transformation given by equation 2.2, one obtains the following result:

$$\begin{cases} i_d = \dfrac{2}{\sqrt{3}} \cdot I_k \sin \vartheta_{me} \\ i_q = \dfrac{2}{\sqrt{3}} \cdot I_k \cos \vartheta_{me} \end{cases} \tag{2.32}$$

According to the previous considerations on the torque behaviour, if the rotor is moved while the stator is fed with the currents given by equation 2.31 and equation 2.32, when torque is null results $\vartheta_{me} = \dfrac{\pi}{2}$.

An example of measured torque over mentioned conditions is given in figure 2.15, during one revolution turn of a the rotor of figure 2.16.

The measure sampled by dSpace board and stored for MATLAB® post–elaboration is affected by noise and cogging effects that can be removes by a Fourier harmonic analysis and a recomposition of a limited number of harmonic components.
The results is shown in figure 2.17.
Filtering the signal torque with this technique has been demonstrated to be very effective for this type of measurements.

[16]The angle indicated as ϑ_{me} is the position of the d–axis (polar axis) with respect to the axis of phase `a`.

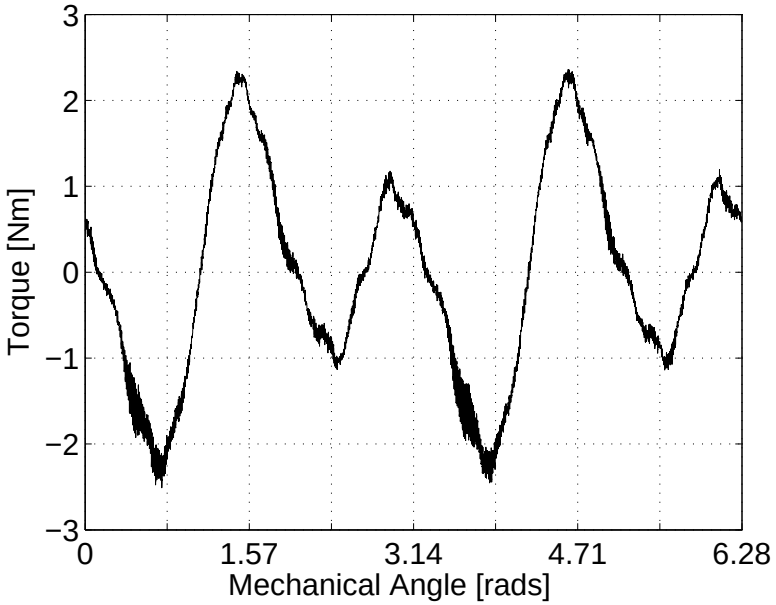

Figure 2.15: Torque measure during positive speed (original signal)

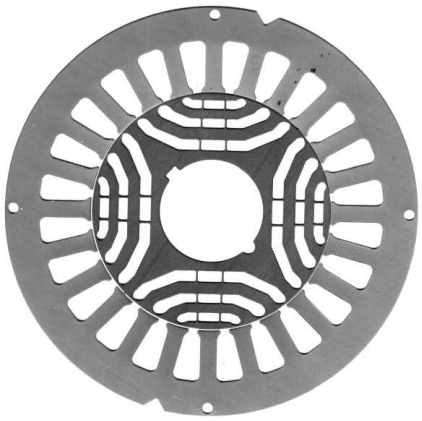

Figure 2.16: Prototype motor lamination used in tests

In case of torque disturbed by cogging and ripple torques and, in any case, to distinguish the two zeros (at least) in any period of the torque behaviour, it is convenient to supply the motor with low currents to make negligible any magnetic saturation and cross-coupling effect.
In the figure 2.17, the thick continuous line is the torque curve composed by the addition of first and second harmonic, the bold continuous line is the addition of first 24 harmonic components. Two dotted lines are the fundamental harmonic and the second harmonic components.
Therefore equation 2.30 can be applied.

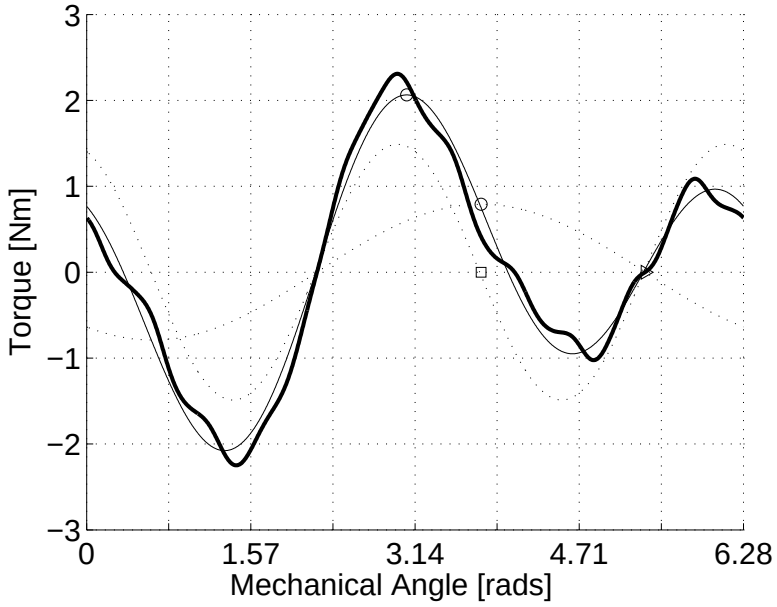

Figure 2.17: Elaborated torque measure during positive speed (some harmonics)

According to equation 2.32, the torque results:

$$m = \sqrt{3}p\Lambda_{mg}I_k \cos\vartheta_{me} + p(L_d - L_q)I_k^2 \sin(2\vartheta_{me}) \tag{2.33}$$

Equation 2.33 reveals that with the supply conditions indicated above, the torque consists of two harmonics[17]: the first one supported by the permanent magnets and the second one due to reluctance contribution, with a twice frequency.
Both of them are null when $\vartheta_m = \dfrac{\pi}{2}$ and this is the information used obtaining the d–axis position and, immediately the quadrature axis.

The sampling of torque signal take place in one mechanical rotation; with this, every single harmonic has a number of period coincident with the number of pole pairs multiplied by the order of the harmonics.

As indicated by equation 2.33, the angle $\vartheta_{me} = 0$ is where the first harmonic is maximum positive and the second one is null with negative derivative. In the figure this occours at about 3.6 *rads* of the incremental position of the encoder and is the point marked by a circle for the maximum torque of the

[17]Neglecting ripple torque.

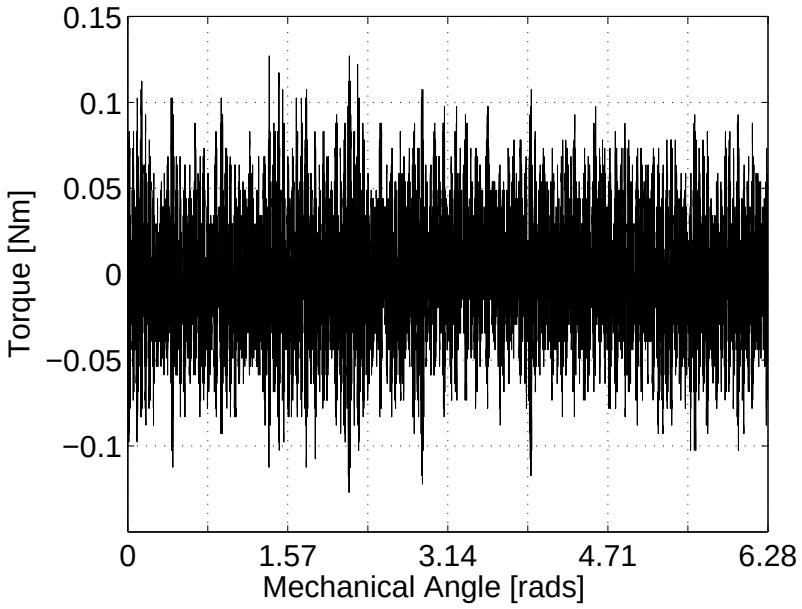

Figure 2.18: Torque measure signal from torquemeter

first harmonic and with a square for the null value of the second harmonic. For this value of ϑ_{me} the current–vector is along the q–axis.

This method want to know the direction of rotation because the position of d–axis respect of the maximum torque value depends of the rotation direction: before if rotation is positive and afterward if rotation is negative. Anyway, the d–axis position is where the second harmonics is null and the first one is maximum.

Because of the first harmonic torque is present even if $L_d = L_q$, the method is the same also if the MuT is an SPM motor.
In such a case the zero detection of first harmonic can be preferred.

Cogging Torque measure

The measurement id performed by running the MuT through the torquemeter with a very constant speed while the motor is not energized by the inverter supply (stator phases are open).
Ripple torque can be very small, in some case lower than the torque measurement noise, as in figure 2.18 which is the plot of signal acquired from the torquemeter.

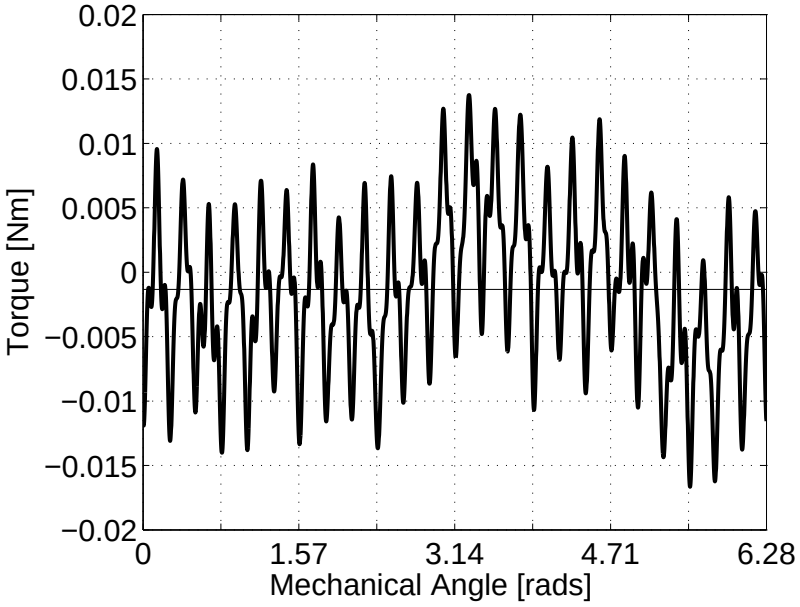

Figure 2.19: Cogging torque after elaboration

However it can be extracted taking advantage from its periodicity that is related to the number of slots and pole and anyway is easily recognized by the measurement data.
To this purpose a Fourier harmonic analysis is performed on the sampled torque. DC component and undesired harmonic components are rejected while the components at the frequency of the cogging torque and its multiples are preserved and re-composed.

The result is the curve shown on figure 2.19.

Flux-current magnetization curves

The high speed version of the test bench is used for dynamic measurements on the MuT, as motor efficiency, thermal test, flux-weakening performance and so on.
One of the possible test is also the measurement of the d– and q–axis flux-current curves (magnetization curves). The measure procedure consists in running the MuT at a given constant speed and measuring the stator terminal voltage while the motor is fed by either a d– or a q–axis constant current.
With $i_d = I_d \neq 0$ and $i_q = 0$, the steady–state q–axis stator voltage becomes:

$$U_q = p\Omega_m \Lambda_d(I_d) \tag{2.34}$$

while under $i_q = I_q \neq 0$ and $i_d = 0$, the steady–state d–axis stator voltage is:

$$U_d = -p\Omega_m \Lambda_q(I_q) \tag{2.35}$$

As a result from equation 2.34, one obtains:

$$\Lambda_d(I_d) = \left.\frac{U_q}{p\Omega_m}\right|_{I_q=0} \tag{2.36}$$

and from (2.35):

$$\Lambda_q(I_q) = \left.\frac{U_d}{p\Omega_m}\right|_{I_d=0} \tag{2.37}$$

Both d– and q–axis voltages are reconstructed from the measured line–to–line terminal voltages after an appropriate filtering in order to removing switching harmonics.
An example of measurement of flux-current curves is reported in figure 2.20 and 2.21 which report fluxes vs. currents for both d– and q–axis relative to the rotor depicted in figure 2.16.

One can recognizes:

- the linear behaviour of the flux-current relationship in the d–axis for negative current, as the magnetic circuit is highly de–saturated.
- the saturation effect on the same curve at positive current.
- the deformation of the curve due to de–saturation of iron bridges just the d-axis current is positive and the successive re-saturation (in reverse direction) at higher positive current.
- the saturation effect on the flux vs. current relationship in the q–axis for both negative and positive current.

The test should be simply repeated with both d– and q–axis currents different from zero to highlight magnetic cross–coupling effects.

Torque mapping in i_d–i_q plane.

The test bench is designed to perform also a torque measurement at different combinations of d– and q–current. The values of torque given back from the dSPACE® real time acquisition to MATLAB® can be processed to derive

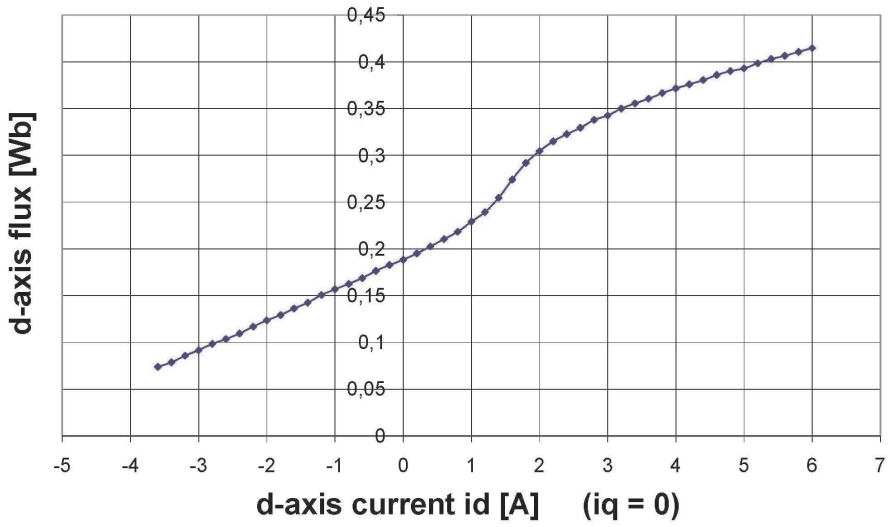

Figure 2.20: d–axis flux of the MuT vs. currents

constant torque curves as in figure 2.22.

Torque measures has been filtered and processed to remove cogging and ripple components. The shadowed area on the up corners identify the extrapolated region (yellow background). The dotted lines are the loci computed with a linear non saturated model; instead, the continuous lines, are the plots of the measures. The labels over the curves identify the torque level for calculated and measured torque.

From figure 2.22 one can readily recognize the effects of iron saturation. In particular an interesting aspect of the data of figure 2.22 is the difference between calculated (linear) curves and measured curves for positive d– and q– currents, where saturation occurs in both axis. The result is a rotation of the asymptote of the constant torque curves (coincident with the zero torque curves for high currents) from its theoretical vertical position calculated close to $I_d = 2\ A$.
This can be justified linearizing the flux–current curves in the saturated region

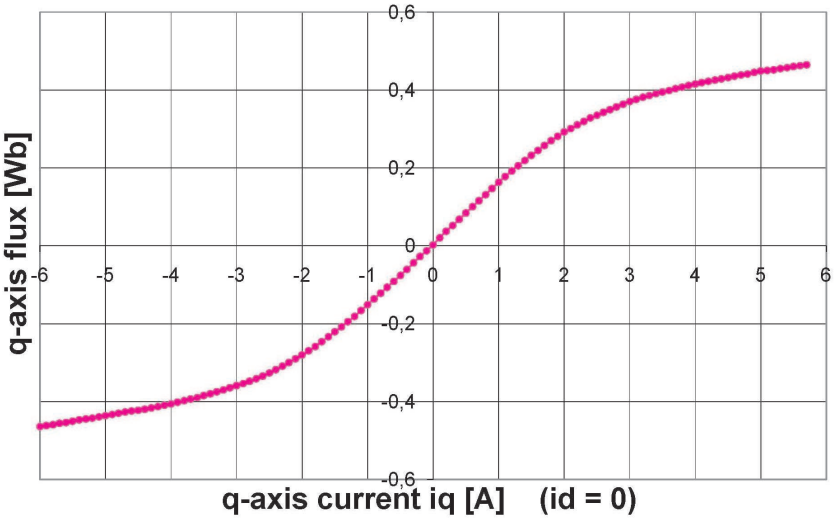

Figure 2.21: q–axis flux of the MuT vs. currents

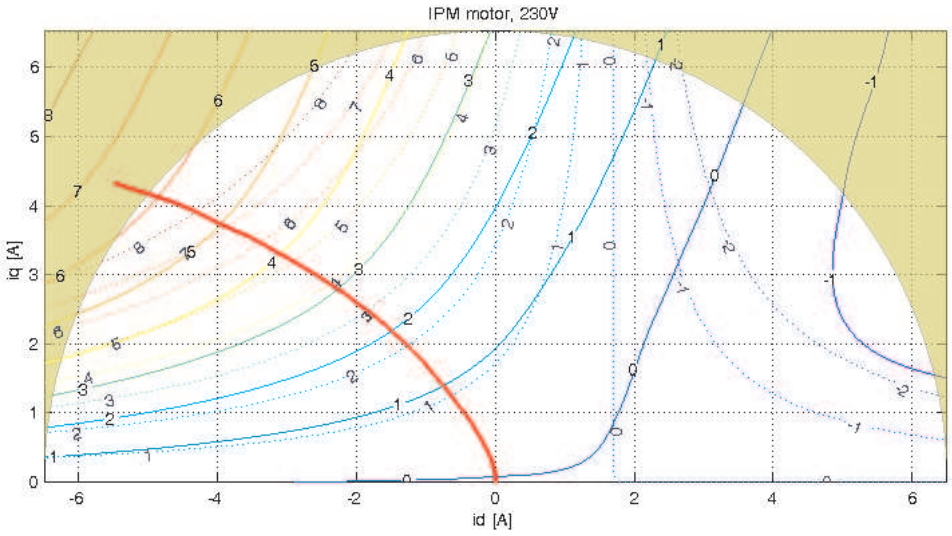

Figure 2.22: Constant torque loci in the d– and q–current plane for an IPM motor

as follows:

$$\begin{cases} \lambda_d &= \lambda_{de} + L_{sd} i_d \\ \lambda_q &= \lambda_{qe} + L_{sq} i_q \end{cases} \tag{2.38}$$

where λ_{de} and λ_{qe} are extrapolated values at null currents and L_{sd} and L_{sq} are saturated (differential) inductances.

From equation 2.38 and assuming that $L_{sd} = L_{sq}$ (which is near to the reality) the torque expression results:

$$m = \frac{3}{2} p \cdot [\lambda_{de} i_q - \lambda_{qe} i_d] \tag{2.39}$$

which is null along the line given by the following equation[18]:

$$\frac{i_q}{i_d} = \frac{\lambda_{qe}}{\lambda_{de}} \tag{2.40}$$

A post-processing routine has been also developed to detect on each constant torque locus the MTPA point, reported by the bold line in figure 2.22.

[18] Obtained approximating the d–axis flux linkage as a line.

Chapter 3

Applications

3.1 Direct–drive control model

An important application using a high-torque low–speed motor is the Direct–drive mode, where the shaft is directly connected to the load with no speed reduction gear box.
In this part of the dissertation it's explained a direct drive rope–based lift system which is widely used in civil and commercial buildings because of the advantages in terms of volume and costs due to the elimination of the gear–motor room.
Reliability of the whole system is also improved and the need of maintenance is greatly reduced.
An accurate and comfortable motion control of the cabin should be the main issue in a rope–based lift system especially during the start of the cabin from the floor and the stop at the floor approaching. To achieve this target is important to use a minimal set of sensors and transducers in order to reduce costs and to increase reliability.
In particular, the control of the cabin has to realize the simple motion of the lift but, at the floor level after the doors are closed and mechanical brakes are released, any shake of the cabin has to be as small as possible. This is the more demanded achievement of comfort during the lift service.

In order to solve this task, an effective estimation algorithm of the load torque applied to the motor pulley, which is due to the unbalanced mass applied, is implemented. I.e. the counterweight and the mass of the cabin. The latter is variable because of the undetermined number of people whom go up the elevator. In this case, in order to determine the unbalance direction, a torque estimation is perform rapidly just after sending the release command to the brakes, using only the information received by the incremental encoder installed on the motor shaft.
On the basis of estimate, a feed-forward action is applied at the output of the

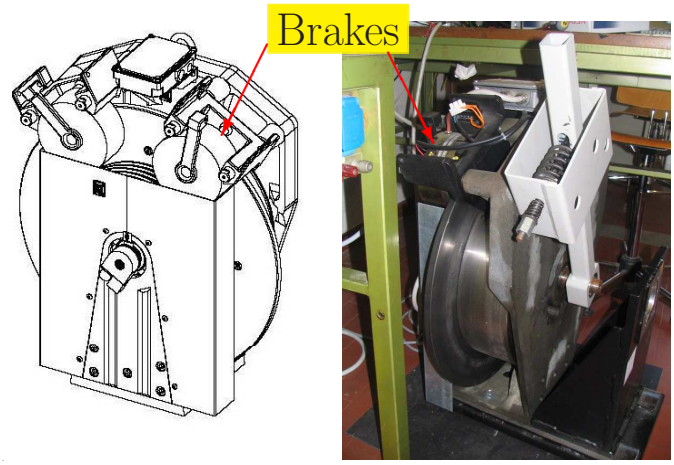

Figure 3.1: Motor drawing (left) and mass-spring test bed (right)

Proportional, Integrative and Derivative (PID) speed controller, to generate an enhanced torque reference with the purpose of obtaining a minimum speed error. Since the speed reference signal is equal to zero, the overall result is a minimized cabin movement.

The first part of this section describes the items which compose the system. Then the study and development of a detailed dynamic model of the system, considering the rope elasticity is explained on the second part. Third part reports the load torque estimation algorithm and feed-forward action on the torque reference signal in order to carry out better results as movement comfort.

3.1.1 Lift system and components

The elevator system considered uses a motor drive specifically designed, as shown in figure3.1, [7].

The machine is a Surface-Mounted Permanent Magnet three-phase synchronous motor with external rotor; the parameters are reported in table 3.1, together with the essential information about the control system. Figure 3.1 shows also the brakes that work on a disk which is axially connected to the rotor.

In order to characterize the SPM motor used on the lift equipment, a set o measurements on test bench has been done. Results are reported as follows:

$$\begin{cases} \lambda_d = \lambda_d(i_d) \\ \lambda_q = \lambda_q(i_q) \end{cases} \tag{3.1}$$

Table 3.1

	SPM Motor with external rotor		
	Description	**Value**	**Unit**
1	Nominal Voltage (U_a)	380	V
2	Nominal Current (I_n)	24	A
3	Nominal Torque (M_n)	320	Nm
4	Pole pairs	12	
5	Pulley radius	0.17	m
	Control system		
6	Position measure: encoder 2048 ppr with SPI absolute position		
7	Inverter: three-phase IGBT with 10 kHz PWM		
8	Controller board: equipped with Freescale DSP 56F803		

Equation 3.1 indicates the measures implemented: flux linkage varying the d– and q–axis currents. The measures have been made in two different way and the results are plotted in figure 3.2.

- Time constant of both axes from voltage–step response (blue line).
- Flux linkage MATLAB® computation using voltage reference u_d^* and u_q^* from current control loops (red line).

Figure 3.2 shows two plot of flux linkage, as indicated from equation 3.1. On both plots, the red lines represent the values of L_d and L_q, neglecting the cross–coupling[1], obtained by MATLAB® computation evaluating flux linkage and next inductances value. Fluxes are computed using equation 3.2 as example of Λ_d evaluation.
The measure has been done using 6000 samples, with a downsampling factor of 2. The motor was dragged at a constant speed of 50 *rpm*.

$$\Lambda_d = \frac{u_{q_{mt}}}{p \cdot \omega_m} \tag{3.2}$$

In addition, blue lines on figure 3.2 are both axes flux linkage obtained from inductances measure as response to a voltage–step of $\pm 100\ V$ with the rotor braked.
Voltage step is applied to u_d estimating L_d and to u_q estimating L_q. An oscilloscope has been used for the measure of voltage response in a time–window

[1]Referring to sub–paragraph 2.2.1.

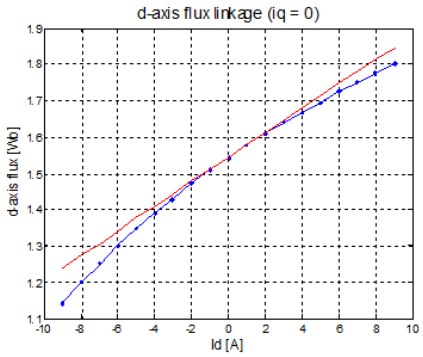

(a) D-axis flux linkage ($iq = 0$)

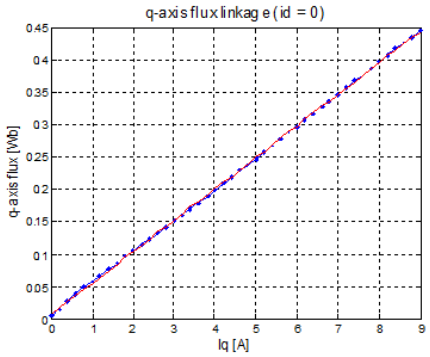

(b) Q-axis flux linkage ($id = 0$)

Figure 3.2: D- and Q-axis flux linkage

of 1 ms^2.

The axis inductance values obtained from the measure are (mean values):

$$\begin{cases} L_d = 34\ mH & \text{(around the point } i_d = 0\text{)} \\ L_q = 49\ mH & \text{(constant in the current range examined)} \end{cases} \tag{3.3}$$

Even if the motor is an SPM the inductance values are different for the two axes because of the different path of flux produces different iron saturation.

With the volt-ammeter measurement, the value of the line–to–line resistance is obtained. Its value has resulted:

$$R_{f-f} = 8.9\ \Omega \tag{3.4}$$

These measures are an useful tool for designing a motor model to evaluate the best control strategy.

In order to guarantee the minimum cabin oscillation, a particular care has been reserved for the control strategy design.
Figure 3.3 shows the mathematical model used to simulate different type of control (speed control and position control).

This MATLAB® –Simulink model has been used to simulate the speed control and it does not take into account rope elasticity. It is mainly composed by a speed loop with a discrete–time PI controller which provides a torque reference entering in a block named 'Torque Control'.

[2]Corresponding to 10 PWM periods.

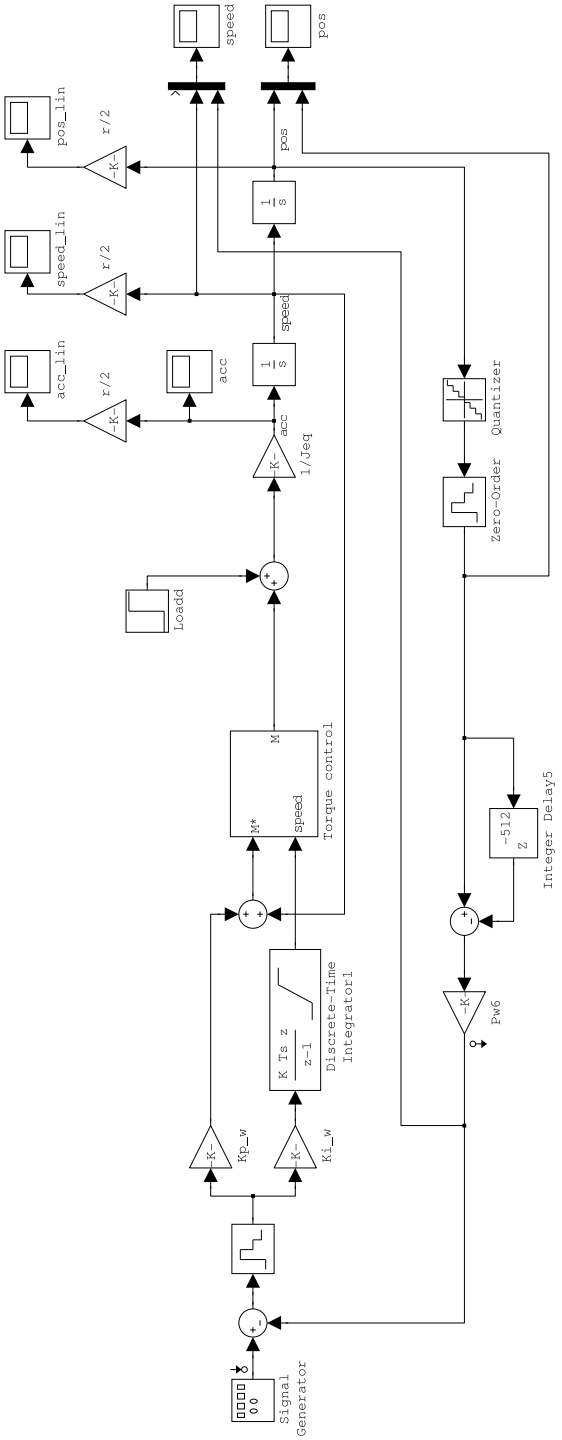

Figure 3.3: Simplified Motor and Load model

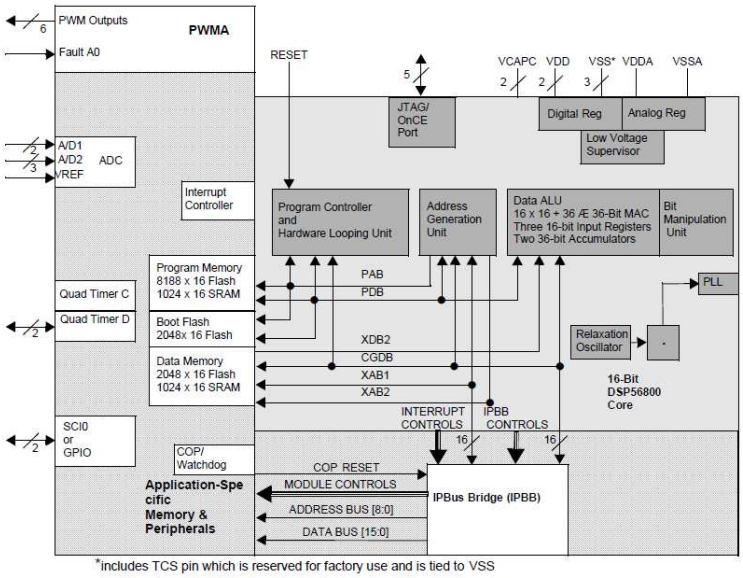

Figure 3.4: Freescale® $DSP56F803$ block diagram

This block contains the motor model obtained from parameter measured above. On figure 3.3, is possible to see the speed–feedback which has the conversion from continuous–to–discrete time.
A value of inertia, indicate as J_{eq} on the block diagram, is computed adding the inertia contribution of motor, counterweight and cabin.

The simulations results have been proved in a prototype realized in a laboratory bench, as will be presented in the specific subparagraph. Motion control is realized with the actual motor and the power inverter. There is a closed speed loop using the signal obtained by the speed sensor (encoder) connected to the motor shaft. Also the stator current high performance loops are present in order to implements a vector control.
No other transducer is installed for the motion control task.

The control firmware is realized with a Digital Signal Processing Freescale Semiconductor `DSP56F803`, which provide several peripheral dedicated for motion control.
Figure 3.4 is the block diagram of Freescale DSP, which shows peripheral and interconnection between them.

Some features are reported in the following list:

- *Pulse Width Modulator module (PWM) with six PWM outputs, three Current Sense*

inputs, and three Fault inputs, fault tolerant design with dead-time insertion, supports both center- and edgealigned modes, support patented dead-time distortion correction.

- *Two 12-bit Analog-to-Digital Converters (ADCs), which support two simultaneous conversions; ADC and PWM modules can be synchronized.*
- *Quadrature Decoder with four inputs (shares pins with Quad Timer)*
- *Four General Purpose Quad Timers*
- *CAN 2.0 B module with 2-pin ports for transmit and receive*
- *Serial Communication Interface (SCI) with two pins (or two additional GPIO lines)*
- *Serial Peripheral Interface (SPI) with configurable 4-pin port (or four additional GPIO lines)*
- *Computer Operating Properly (COP) Watchdog timer*
- *Two dedicated external interrupt pins*
- *Sixteen multiplexed General Purpose I/O (GPIO) pins*
- *External reset input pin for hardware reset*
- *JTAG/On-Chip Emulation (OnCE®) for processor speed-independent debugging*
- *Software-programmable, Phase Lock Loop-based frequency synthesizer for the DSP core clock*

It is a micro-controller specifically oriented to motion control, with its high-speed 12-bit Analog-to-Digital Converter (ADC) which provide digital current value in 1.2 μs. Furthermore, it's possible to synchronize the converter with the Pulse With Modulation machine. ADC is a very important part of the control system because of it's full control of the IGBT (Insulated Gate Bipolar Transistor) which are the power switch of the converter. The dead-time distortion correction feature provided directly by the PWM machine, is very useful in order to have the best linearity in the control chain, in which the inverter is a specific block.

Figure 3.5 is a shot of the inverter prototype used for the bench in order to evaluate the effectiveness of the control algorithms.
It is composed by a set of boards such as logic board, microcontroller board and power board. Is is a 15 kW inverter system, with a PWM of 12 kHz.

The DSP manufacturer provides some motion control routines in order to reach the best performance of the computational speed of the logic unit.
All the variable are fixed–point format and this implies to pay care during the algorithm implementation.

Figure 3.5: Inverter prototype use to create the lift equipment

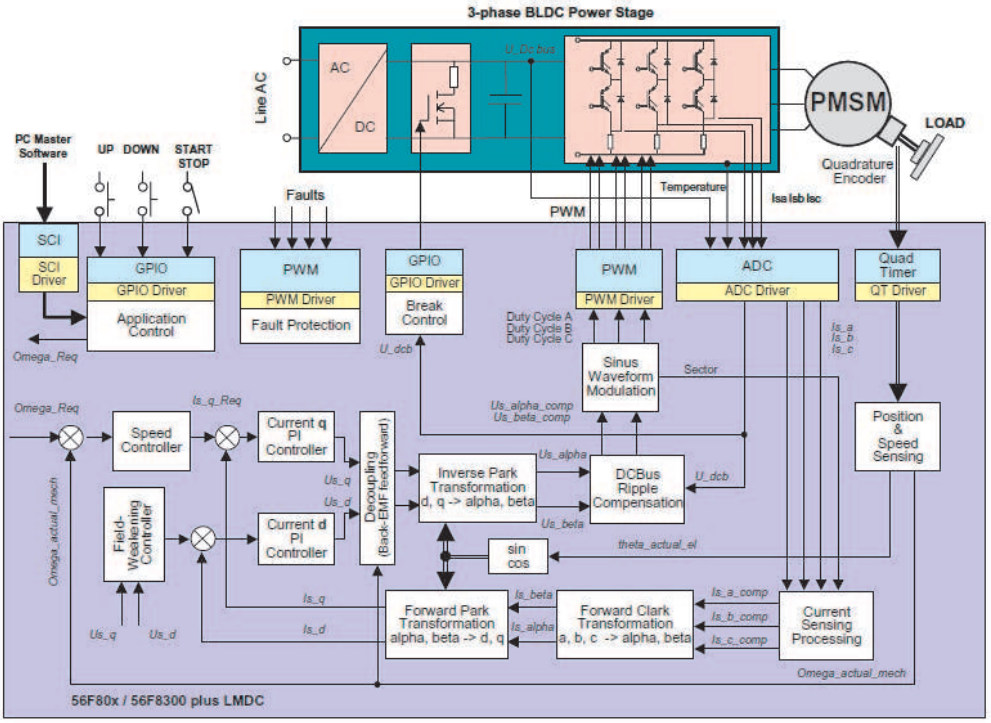

Figure 3.6: Basic vector control block diagram with routine designed for Freescale® DSP

Figure 3.6 shows a block diagram of principal routine which have to be used for a vector motion control of PM synchronous motor.
Each block corresponds to a routine which can be implemented on DSP firmware. It can be noticed that the control system can be interfaced with external world via some communication protocols.

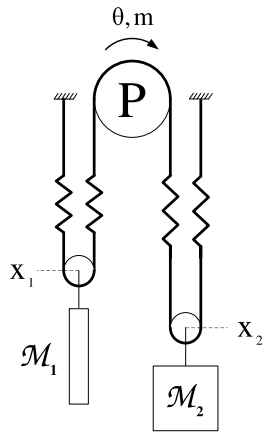

Figure 3.7: Schematic model of Direct-Drive lift system

3.1.2 System modeling

A possible improvement is to create a mathematical model which considers the rope elasticity modelling by springs along the rope. The direct drive lift system can be then modelled as shown in figure 3.7. The system includes the pulley P directly connected to the PM synchronous motor that moves, by means of the ropes, the counterweight $\mathcal{M}_1$ and the cabin $\mathcal{M}_2$. Brakes are applied to the pulley during the stop phase of the system, where angular position θ is assumed equal to zero. This is the steady-state position respect of which the coordinates x_1 and x_2 return the position of counterweight and cabin.

In order to obtain the Transfer Function (TF) of the system represented above, a way is to divide the system of figure 3.7 into three subsystems as reported in figure 3.8, figure 3.9 and figure 3.10.
In this treatment the lower letters are for time-dependent variables, whereas capital letters are used for constant coefficients.

For sub-system of figure 3.8, applying the force balance on the two components given by the stiffness and the damping of the rope, one can obtain:

$$\mathcal{M}_1\ddot{x}_1 = -2K_1x_1 - K_1R\theta - 2D_1\dot{x}_1 - D_1R\dot{\theta} \tag{3.5}$$

where K_1 and D_1 represent the stiffness and the damping coefficient of the rope on the counterweight side, while R is the pulley radius. Weight force $F_1 = \mathcal{M}_1 \cdot g$ (g gravity acceleration) of the mass $\mathcal{M}_1$ does not appear in (3.5) as it is balanced by the elastic force $K_1x_{1_0}$, where x_{1_0} is the steady-state elongation of the ropes.

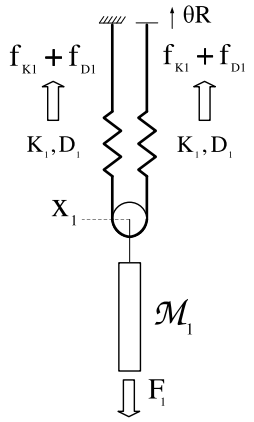

Figure 3.8: Schematic model of Direct-Drive lift system

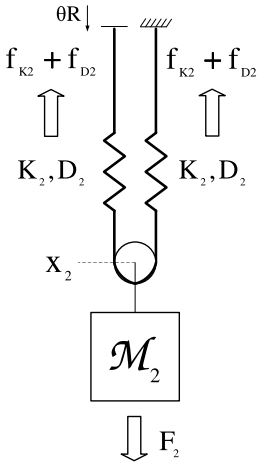

Figure 3.9: Schematic model of Direct-Drive lift system

The same force balance is applied to the subsystem of the cabin in figure 3.9, yielding to:

$$\mathcal{M}_2\ddot{x}_2 = -2K_2x_2 + K_2R\theta - 2D_2\dot{x}_2 + D_2R\dot{\theta} \tag{3.6}$$

where K_2 and D_2 are the stiffness and the damping coefficient of the rope on the cabin side. Again, the weight force $F_2 = \mathcal{M}_2 g$ of the mass $\mathcal{M}_2$ is balanced by the elastic force $K_2 x_{2_0}$, and it does not appear in (3.6). Always x_{2_0} is the steady state elongation of the ropes.

For the part of the whole system reported in figure 3.10, the motor-side torque balance returns the following equation:

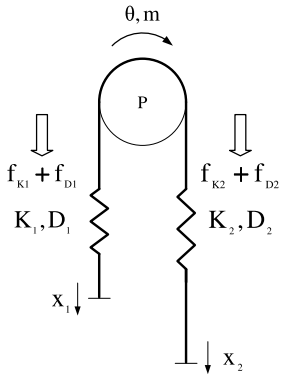

Figure 3.10: Schematic model of Direct-Drive lift system

$$J_p\ddot{\theta} = m + \left(-\frac{F_1}{2} + \frac{F_2}{2}\right) R + \\ + (f_{K2} - f_{K1} + f_{D2} - f_{D1})R \tag{3.7a}$$

where m is the motor torque and

$$\begin{cases} f_{K1} = K_1 \left(x_1 + \dfrac{\theta}{2}R\right) \\ f_{K2} = K_2 \left(x_2 - \dfrac{\theta}{2}R\right) \\ f_{D1} = D_1 \left(\dot{x}_1 + \dfrac{\dot{\theta}}{2}R\right) \\ f_{D2} = D_2 \left(\dot{x}_2 - \dfrac{\dot{\theta}}{2}R\right) \end{cases} \tag{3.7b}$$

are respectively elastic forces and damping forces, as indicated in [8].

From (3.5), (3.6) and (3.7) one can realizes that input of the system is $m_{eq} = m + (-F_1 + F_2)R/2$ which is the unbalanced torque on the pulley, and the whole mechanical system can be represented by the block diagram of figure 3.11.

Transforming into s-domain the three basic equations (3.5), (3.6) and (3.7) come out the following expression:

$$\begin{aligned} TF(s) &= \frac{\Omega(s)}{M(s)} \\ &= \frac{\left(s^2 + s\frac{2D_1}{\mathcal{M}_1} + \frac{2K_1}{\mathcal{M}_1}\right)\left(s^2 + s\frac{2D_2}{\mathcal{M}_2} + \frac{2K_2}{\mathcal{M}_2}\right)}{J_p s(s^4 + a_{D3}s^3 + a_{D2}s^2 + a_{D1}s + a_{D0})} \end{aligned} \tag{3.8}$$

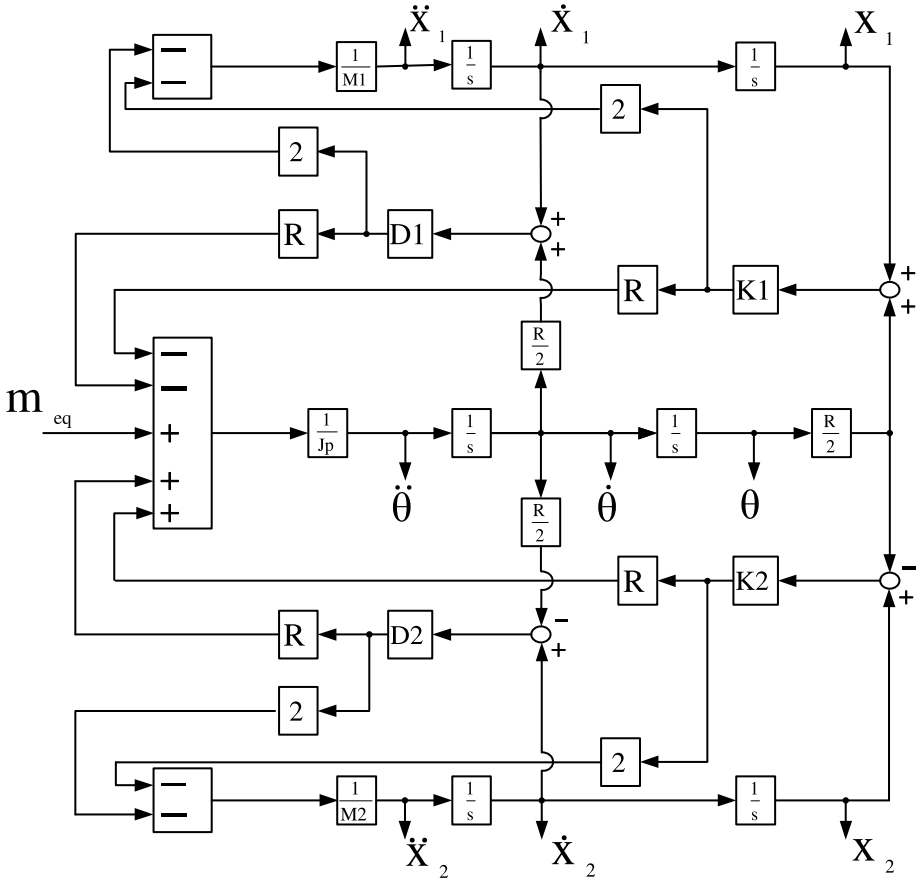

Figure 3.11: Block diagram of Direct–Drive lift system

where

$$
\begin{aligned}
a_{D3} &= \frac{2D_1}{\mathcal{M}_1}\left(1+\frac{R^2\mathcal{M}_1}{4J_p}\right)+\frac{2D_2}{\mathcal{M}_2}\left(1+\frac{R^2\mathcal{M}_2}{4J_p}\right)\\
a_{D2} &= \frac{2K_1}{\mathcal{M}_1}\left(1+\frac{R^2\mathcal{M}_1}{4J_p}\right)+\frac{2K_2}{\mathcal{M}_2}\left(1+\frac{R^2\mathcal{M}_2}{4J_p}\right)+\\
&\quad+\frac{4D_1D_2}{\mathcal{M}_1\mathcal{M}_2}\left(1+\frac{R^2\mathcal{M}_1}{4J_p}+\frac{R^2\mathcal{M}_2}{4J_p}\right)\\
a_{D1} &= \frac{4D_1K_2}{\mathcal{M}_1\mathcal{M}_2}\left(1+\frac{R^2\mathcal{M}_1}{4J_p}+\frac{R^2\mathcal{M}_2}{4J_p}\right)+\\
&\quad+\frac{4D_2K_1}{\mathcal{M}_1\mathcal{M}_2}\left(1+\frac{R^2\mathcal{M}_1}{4J_p}+\frac{R^2\mathcal{M}_2}{4J_p}\right)\\
a_{D0} &= \frac{4K_1K_2}{\mathcal{M}_1\mathcal{M}_2}\left(1+\frac{R^2\mathcal{M}_1}{4J_p}+\frac{R^2\mathcal{M}_2}{4J_p}\right)
\end{aligned}
$$

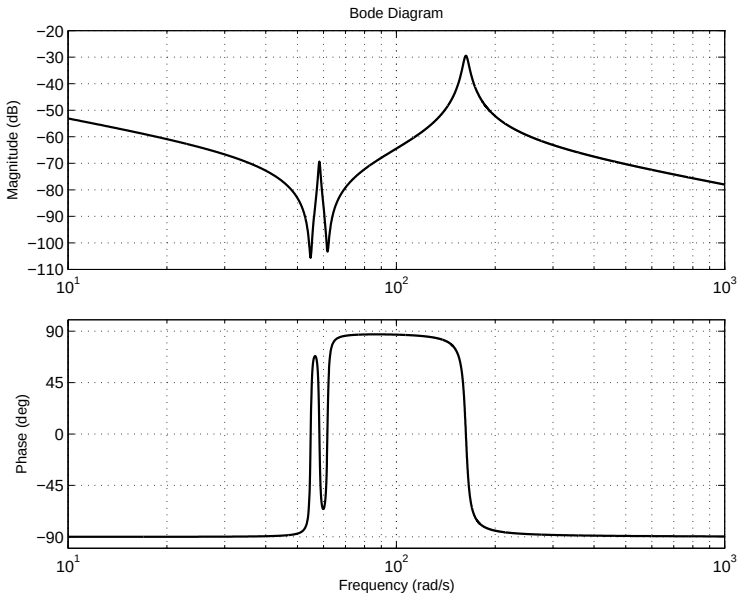

Figure 3.12: Bode diagram of $TS(s)$ considering the rope elasticity

Figure 3.12 shows the Bode diagram (frequency response) of $TF(s)$ in the case $K_1 = K_2$. From the figure, it can be seen, and is possible to prove, that $TF(s)$ exhibits a sequence of second order zeros and poles, in addition to the pole and the zero at null and infinite frequency respectively.
With the Transfer Function 3.8 is possible to design the speed control loop, as indicated in [9]

3.1.3 Load torque estimation using the complete model

When the brakes are released, the unbalanced situation that appears on the motor pulley is unknown because it depends on the number of people in the cabin. It involves a system acceleration whose direction and intensity are therefore unknown.
The dynamic behavior can be examined using the scheme shown in the figure 3.13, get by the $TF(s)$ developed in the preview paragraph.
The block surrounded by a dashed line which provide the torque estimation value m_e is a contribution to the PID speed controller output (a feed-forward action). At first analysis, this contribution can be ignored: it will be discussed later.

The brake system of the elevator equipment operate directly on the pulley applying a force on a disk integral with the rotor of the motor. Feeding the brakes, an electromagnet provide the removal of the pad from the disk. When

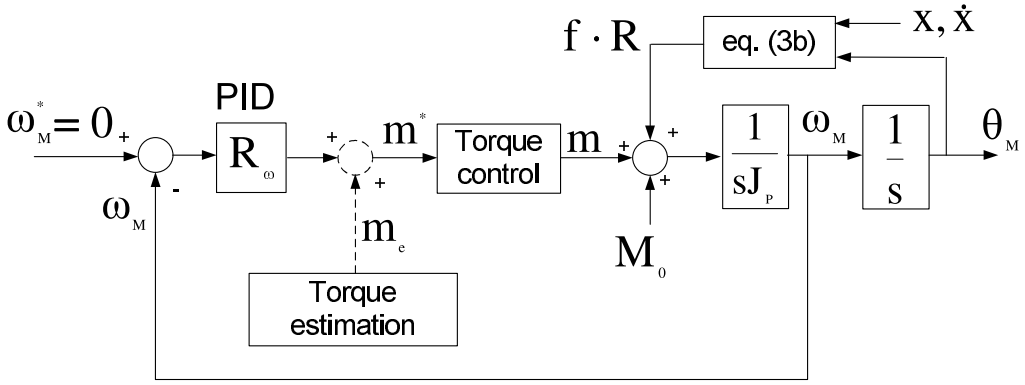

Figure 3.13: Motion control scheme

electric power is take out, two springs exercise the force which stops the pulley and, consequently, the cabin. Because of this, is assumed that the brakes are released instantaneously, so torque disturbance is a step-shaped torque given by equation 3.9.

$$M_0 = (-F_1 + F_2) \cdot \frac{R}{2} \tag{3.9}$$

while the torque addendum given by $f_x\, R$, with f_x expressed by equation 3.7b, is equal to zero in any steady state condition.
Speed reference ω_m^* is kept equal to zero to keep the cabin still at the floor level. However, the cabin position does not remain equal to zero, due to torque disturbance applied when the brake are opened and caused by the unbalanced contribution of cabin and counterweight, as explained above.
Considering the control scheme of figure 3.13, in particular the speed loop, it can be proved that steady–state position error at the floor level after the brakes are released is proportional to load torque amplitude.
The proof is quickly accomplished by evaluating the torque m when the time is infinity, as reported on the following equation:

$$m(\infty) = -M_0 = K_I \int_0^\infty \omega dt = K_I \theta(\infty) \tag{3.10}$$

where K_I is the integral gain of the PID controller. Some consideration about the equation 3.10: in writing it it's important to take into account that proportional and derivative contributions of the speed controller are null at steady-state.
Furthermore, for simplicity, it as been assumed a unitary gain of the torque control block.
From equation 3.10, the follow relation for the angle θ is directly obtainable:

$$\theta(\infty) = \frac{M_0}{K_I} \tag{3.11}$$

Equation 3.11 confirms the elastic behaviour of a PID speed control under null speed reference.
In order to reduce angular movement and therefore the cabin hop after brake releasing, the integral gain has to be increased as much as possible, assuring the stability of the system. However, the elasticity of the ropes with the presence of the poles in the system transfer function, as one can see from figure 3.12, implies an upper limit of the PID speed control bandwidth and, consequently, an upper limit of the integral gain [9].

An alternative way to reduce the cabin hop when it is in idle at the floor level and the brakes are released, consists in introducing a feed–forward action by adding an estimation of the load torque to the output of the speed controller. This avoid the torque reference to be entirely generated by the integral action of the speed controller and then reduce the integral of the speed error given in equation 3.10.

This feature can add an instantaneous value to the torque reference, but is important to estimate this value as close as possible to the instant of the brake release. In ideal conditions, if the estimation is exactly coincident to the load torque M_0 and the torque control has an unity gain and negligible delay, no movements will occur as can be easily recognized from figure 3.11 and figure 3.13.
Unless the use of an additive transducer, i.e. a load cell which weigh the load of the cabin when the brakes are activated, the perfection of the feed-forwarded torque value in unreachable By this consideration is deducible that the problem of angular movement reduction is focused on a rapid and effective estimation of the load torque and the subsequent application of such signal as a feed-forward contribution.
To this purpose, one can observe that motor torque is initially null and pulley movement is initiated by the load torque M_0. Initial acceleration of the pulley is therefore given by

$$\dot{\omega}(0) = \lim_{s\to\infty} s(s\Omega(s)) = \lim_{s\to\infty} s^2 TF(s)\frac{M_0}{s} = \frac{M_0}{J_p} \tag{3.12}$$

where a load torque given by a step function has been assumed. From equation 3.12 it results:

$$M_0 = \dot{\omega}(0) \cdot J_p = \alpha(0) \cdot J_p \tag{3.13}$$

which suggest that the load torque can be estimated through the measurement of the initial motor acceleration $\alpha(0)$, multiplied by the motor inertia.
The algorithm used to estimate the torque compares actual motor position θ_k, deduced by the encoder counter at the sampling time t_k, with the estimated

angular position $\tilde{\theta}_k$ that is given by the following equation:

$$\tilde{\theta}_k = \frac{1}{2}\alpha \cdot t_k^2 \tag{3.14}$$

which is a parabolic relationship.
In writing the equation 3.14, a constant acceleration has been assumed during the short interval of the torque estimation.
The angular acceleration in (3.14) is evaluated by minimizing the quadratic error of comparison between the actual motor position and the estimated one, which brings to the follow equation:

$$\alpha = 2\frac{\sum\limits_{N} \theta_k t_k^2}{\sum\limits_{N} t_k^4} = \frac{2}{T_s^2}\frac{\sum\limits_{N} \theta_k k^2}{\sum\limits_{N} k^4} \tag{3.15}$$

where the comparison is applied for the first N samples and T_s is the sampling period.
Starting from the instant in which the load torque is applied, the equation 3.15 is applied iteratively. This computation stops when a reliable acceleration is attained. This is given when a maximum value of acceleration is carried out by (3.15). The estimated value resulting is used to launch the feed-forward action.
The procedure described above is applied in an actual system used to emulate the elevator system. The results are reported in the next subparagraph.

3.1.4 Experimental results

During the work, some tests in a laboratory bench have been done. In figure 3.1 the architecture of the test bench used in order to simulate the lift system is reported.
The right picture of the figure 3.1 clearly shows the spring which reproduces the torque effect due to an unbalanced cabin-counterweight combination. In fact, the spring does not apply an ideal step-shaped torque to the motor shaft, because of the dependency of its force on the length variation (Hooke's law):

$$F_{spring} = K_s \cdot x \tag{3.16}$$

where K_s is the force constant of the spring and x is its extension, which vary with compression.
In this section, some details of these experimental results are shown.

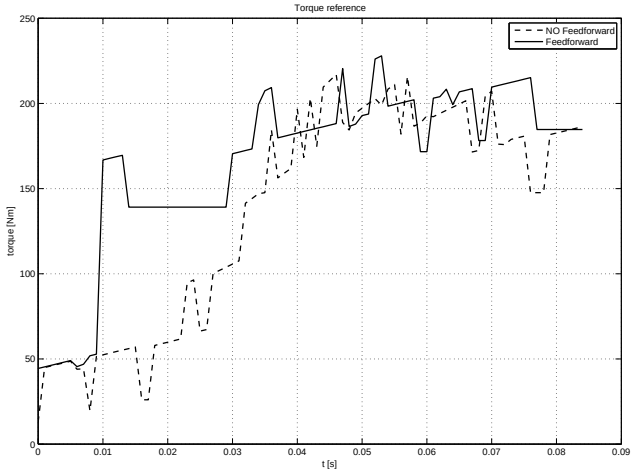

Figure 3.14: Torque reference with and without feed–forward action

The improvement given by the feed–forward action is visible in figure 3.14, where it is possible to see the increment of torque reference, due to the estimated value added.
During the experimental operation, the time interval between the brakes opening command and the actual brake release (which corresponds to the initial movement of the motor) is unknown because of the uncertain and non repetitive behaviour of the brake system. If the estimation algorithm start triggered with the brakes command, the estimation value may be wrong due to the time when the acceleration remain zero. To overcome this trouble, the time origin for the estimation algorithm is fixed at the occurrence of the second encoder pulse in one or the other direction. Then the algorithm starts computing and, after some milliseconds, the final torque is estimated, much earlier than the integration in the PID controller is completed (continuous line in figure 3.14).
The feed-forward action anticipate a substantial part of the steady state reference of the torque which is required to sustain the load. The advantage in term of reduced cabin movement can be clearly recognized in figure 3.15. The figure shows the measured pulley movement with and without the feed-forward action. The measure is expressed in encoder pulses and each pulse corresponds to a cabin movement of about 65 μm.
The advantage of using the load torque estimation and the feed-forward contribute is evident as the cabin movement is approximately reduced within 0.5 mm, instead of more than 1.5 mm, which is tolerable by the comfort requirements.

3.1.5 Conclusion

This work has reported some important results during the modelling of the system. In the first part, during the simulation to select the best control method,

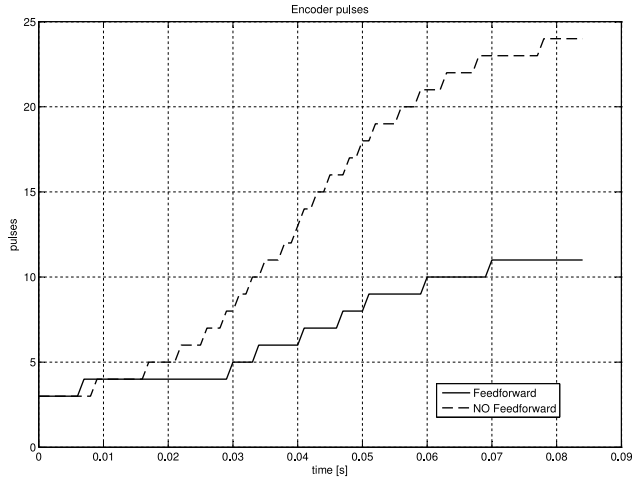

Figure 3.15: Motor position after the release of the brakes, with and without feed-forward action

it has been verified that a position control is not useful for the feature proposed in order to guarantee a comfortable performance. This is also verified when lift–users jump in the cabin: it can prime an oscillation that cause an instability of the system with a position control.
Moreover, the oscillation around a few numbers of encoder pulses is comparable with numerical error.

For the second part of the work an effective estimation algorithm of the load torque applied to the motor pulley, which is caused by the unbalanced suspended bodies of the elevator system, has been developed.

The simulation and the experimental results have reveal that torque estimation, rapidly performed just after the release command is sent to the brakes, is very useful in order to meet particular comfort requests. For improvement of costs and reliability, the torque estimation is based only on the information received by the incremental encoder installed on the motor shaft.
A feed–forward action applied to the output of the PID speed controller to achieve a minimum speed error and then, consequently, a reduced cabin movement is a clever way to help the slow dynamic of the control systems.
Experimental tests provided in order to validate the proposed solution have given good results.

3.2 Maximum Torque per Ampere Self-tuning

In Permanent Magnet Synchronous Motor (PMSM) current control, the usually adopted strategy determines the current vector that generates the required torque, and such a current vector has the minimum magnitude allowing the achievement of that torque. This process of optimization, desirable for minimum losses performance, namely high torque per losses requirements, is based on the mathematical analysis of the constant torque loci, usually in the reference frame fixed to the rotor (d– and q–coordinates, where component d–direct is aligned with the magnet axis of the rotor and component q–quadrature is electrically orthogonal), in order to ease the computations and therefore the implementation of the algorithm in the drive control procedures [2], [10] and [11].

High performance applications, such as wide range speed machinery and robotic devices, generally rely on IPM motors in order to take advantage of their high torque to size ratio and flux-weakening capabilities. Nevertheless the drive has to manage a suitable current control scheme to provide the desired cur- rent components [12].
Figure 3.16 plots the constant–torque loci (hyperbolas in absence of iron saturation) in the i_d–i_q plane. The depicted characteristics correspond to the performances of an IPM motor, as that shown in figure 2.22 and which lamination is reported on figure 2.16, assuming constant non saturated inductances. Positive torque is characterized by positive i_q values while negative torque has negative i_q. The circle corresponding to the nominal motor current (I_N) is also shown.
The optimal working points lie on a locus connecting the center of the plane (point `'O'`) to the base point (point `'B'`). This is the locus where the constant current loci (circles centered in `'O'`) are tangent to the hyperbolic constant torque loci. This curve, therefore, represents the MTPA set of operating points.

3.2.1 MTPA locus

The mathematical equation of the MTPA trajectory, assuming a motor with constant parameters, is

$$i_d = \frac{\Lambda_{mg}}{2 \cdot (L_q - L_d)} - \sqrt{\frac{\Lambda_{mg}^2}{4 \cdot (L_q - L_d)^2} + i_q^2} \tag{3.17}$$

in terms of the two current components i_d and i_q, where Λ_{mg} is the permanent magnet flux linkage, while L_d and L_q are the two motor inductance components in the d– q–reference frame.
It is useful, especially for implementation purposes, to express the MTPA given

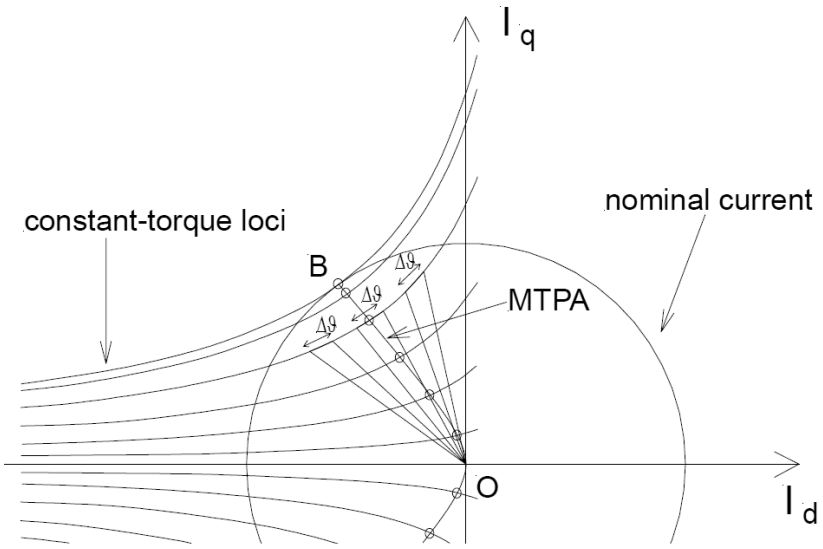

Figure 3.16: MTPA loci on I_d–I_q plane

the current module $i = \sqrt{i_d^2 + i_q^2}$, where the two current components are given by:

$$\begin{cases} i_d = \dfrac{\Lambda_{mg}}{4 \cdot (L_q - L_d)} - \sqrt{\dfrac{\Lambda_{mg}^2}{16 \cdot (L_q - L_d)^2} + \dfrac{i^2}{2}} \\ i_q = \sqrt{i^2 - i_d^2} \end{cases} \tag{3.18}$$

From the above equations one can note that the MTPA curve is a fixed locus as long as the motor parameters remain unchanged during operation. This is not true for a short term runs (e.g. during startup, where the drive[3]) temperature increase to its steady state value) and also during long term runs, due to aging effects and variation of the operating working point.

With regard to the inductive components (L_d and L_q), they are subjected to saturation (short term changes) when high current is fed to the motor; on the contrary the PM flux linkage is more prone to aging effects (long term changes, also due to temperature variations).

Figure 2.22 points out the actual measured constant torque and MTPA loci for the motor shown in figure 2.16. One can realize the different behavior with respect to the ideal case of figure 3.16, due mainly to the non linearity of

[3]Inverter and motor.

the motor inductances.
To take into account every parameter change, a cumbersome parameter monitoring/estimation could be performed, but this requires relevant computational power at the controlling stage and additional hardware on the drive. Moreover, a 'motor parameter model' must also be implemented, tested and evaluated making this effort even non compensating the benefits it gives to the whole drive control.
As a compromise, commercial drives usually implement fixed MTPA characteristics that give average optimization over the whole range of operating point and motor parameter changes. Simple look-up tables or easy to compute interpolating curves are generally used. This allows the use of 16 bit fixed point microcontrollers, avoiding the evaluation of the exact mathematical equation (also involving the computation of square roots).
If IPM motors are used, both i_d and i_q have to be considered in order to characterize the MTPA: this is usually not needed in SPM motors where the quadrature current component only is responsible for the generation of the mechanical torque (apart from side effects due to the i_d, controlled to zero). Therefore a suitable model and its implementation in the drive control is required when IPM machines have to be used.

3.2.2 Simulation analysis

In order to evaluate the feasibility of the proposed self-tuning scheme, some preliminary simulation analysis have been performed. They point out that some information related to the current working point (e.g. how much it is close to the MTPA trajectory) could be extracted from the current signals (reference and actual values) as long as the superimposed spurious pattern stays within the current control bandwidth.
Further analysis also investigates the use of high frequency signals with spectral component above the current control bandwidth.
The drive response to a current control strategy, in which the reference current vector phase is altered on purpose, has been investigated, using the block diagram reported in figure 3.17.

At a given working point (constant required speed and thus torque), the reference current magnitude is delivered by the speed controller when its phase is commanded to vary from $\frac{\pi}{2}$ to π in 9 s, starting from time = 1 s (figure 3.18), after the drives passed the initial transient. Such a change covers the positive torque region in which the MTPA lies. The changes in the reference current phase are obtained by superimposing a phase displacement ϑ_{disp}, moving from 0 to $\frac{\pi}{2}$ in figure 3.17.

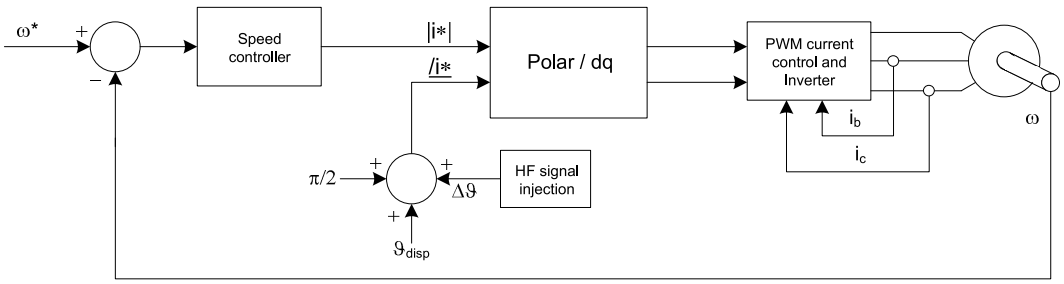

Figure 3.17: System block diagram with self-tuning of MTPA curves

In addition a spurious pattern needed to evaluate the working point position with respect to the actual MTPA is injected. It is a fast (sinusoidal) small–amplitude variation of the phase around its average value. The mechanical torque is kept constant (as constant is the speed of the same mechanical load) due to the current control with bandwidth greater than the spectral component of the superimposed sinusoid.
Figure 3.18 shows that the optimal working point (corresponding to the minimum current magnitude required to generate the desired, constant, torque: MTPA) separates two regions in which the superimposed sinusoidal phase variation in the reference current vector is respectively in phase and in phase opposition (π radians displaced) with respect to the resulting sinusoidal signal over the current vector magnitude reference, as one can realize by analyzing the $\Delta\vartheta$ effects in figure 3.16.
This helps to extract the desired information from the two patterns and therefore to correct the working point towards the optimal MTPA working point at that given current magnitude.

The plots in figure 3.19 represent the result (blue line) obtained after a high pass filter has been first applied to the two signals of figure 3.18 (in order to extract the high frequency component from the current magnitude and to equally phase shift the injected sinusoid) and after they have been multiplied together to obtain only positive or negative values.
A low pass filter then extracts the average value (green smoothed line), corresponding to the error affecting the phase displacement from the actual MTPA working point. All these operation are reported as a block diagram on figure 3.20.

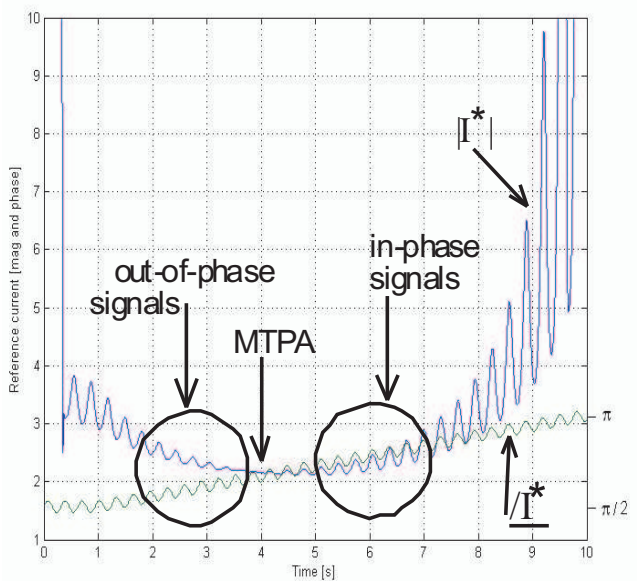

Figure 3.18: Simulation reference current (magnitude and phase)

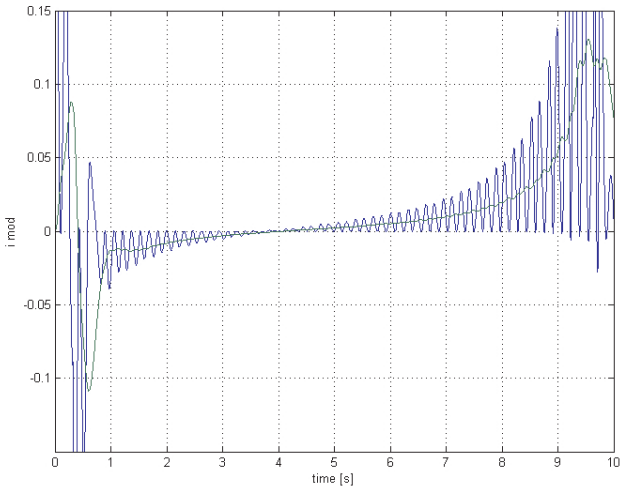

Figure 3.19: Resulting elaborated signals giving information on MTPA phase displacement

3.2.3 Experimental validation on a test bench

The simulated operative condition has been validated on a laboratory test bench in order to check the concept feasibility and to point out some issues that could eventually rise in an industrial environment [4] and [5].

First of all, the possibility to detect effectively the change in the output

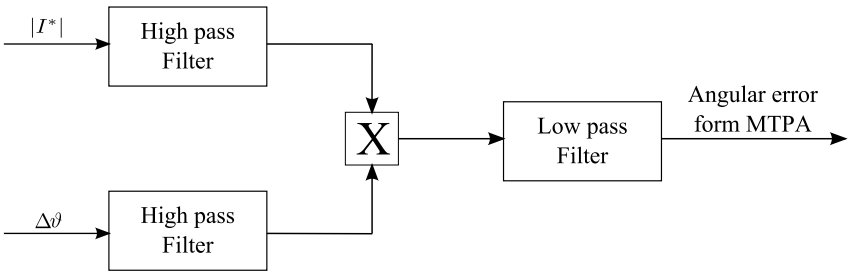

Figure 3.20: High–pass and Low–pass filter blocks used in the signal elaboration

torque due to the injected current–phase signal has been considered. This is not a secondary problem because it affects the drive performance in terms of production of smooth torque, especially on loads that could suffer in their mechanical structure.
The purpose of the suggested technique is to implement a control strategy based on a superimposed current signal whose effect is to produce unwanted torque only when the drive does not operate under optimal condition (outside the MTPA trajectory). As long as the control strategy optimizes the working conditions, it acts to minimize (theoretically to force to zero) the superimposed torque disturbance.

The capability to effectively extract the torque information from the superimposed noise caused by the actual environment (acquisition noise, dynamic controlling signals, undesired cross couplings, etc. . .) has also been verified on the same test bench. Therefore, a trade off between the capability to detect the effects of the injected signal, when it shows non–optimal working conditions, and to produce smooth torque has been verified in practice.

The same operative conditions analyzed in simulation have been duplicated onto a test bench where electrical quantities (currents, voltages, etc. . .) and mechanical quantities (position, speed, torque, etc. . .) are measured throughout the whole test sessions. This does not reflect what is a common industrial application but it is the only way to prove the effectiveness of the presented control strategy. The schematic of the test bench structure is in figure 3.21.

It includes a high bandwidth hysteresis current control. The measured quantities have been acquired by a fast DSP-based control board whose task includes also the processing of the signals shown in figure 3.22 and figure 3.23. The torque measurement capability of the test bench has been performed by the torquemeter `Magtrol TM208` whose measuring range (from -20 to 20 Nm) is actually aligned to the drive performance.

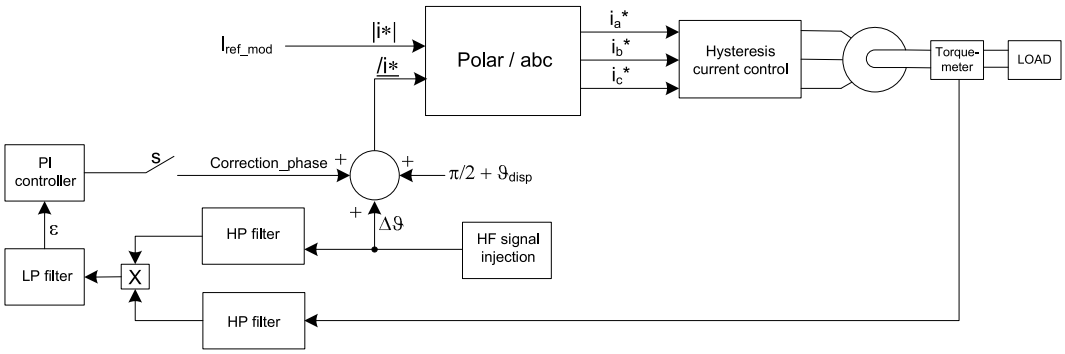

Figure 3.21: Drive scheme with self tuning of MTPA

Multiple tests have been carried out under optimal (on MTPA) and non–optimal conditions. As examples, figure 3.23 shows such different operating conditions. While current vector amplitude is kept constant and equal to 1.5 A, the operational working condition has been forced on purpose to use a current–phase (in the d–,q– reference frame) from $\frac{\pi}{2}$ to π radians. This causes that the optimal point is met in between those values: it happens when the working point is onto the MTPA. To this aim, the phase displacement signal in figure 3.21 is swept from $\frac{\pi}{2}$ to zero and then to $\frac{\pi}{2}$ again (figure 3.22) while switch S is open. In addition a sinusoidal variation of the current phase angle with peak–to–peak amplitude of 0.3 $rads$ and a frequency of 50Hz is superimposed. figure 3.23 gives the current behavior in terms of d– and q–current components.

The torque delivered by the motor, as measured by the torquemeter, is reported in figure 3.24. One can realize that the average torque level is not constant; it reaches its maximum value when operating point lies on the MTPA locus.
As long as the drive operates in MTPA the produced torque is not affected by the signal superimposed on the reference current phase as it could be observed in figure 3.24 where the torque oscillations have a reduction to zero and an inversion of phase passing through the MTPA conditions.

In order to investigate better the phenomenon, the high frequency torque content is multiplied by the injection phase signal and the product is passed through a low pass filter. The result is given in figure 3.25 which shows an error signal of figure 3.21 that gives information on how far the operating point is from the MTPA condition.

Based on this fact, a simple but effective self–tuning strategy has been implemented, by closing the switch S in figure 3.21. A low-dynamic PI control

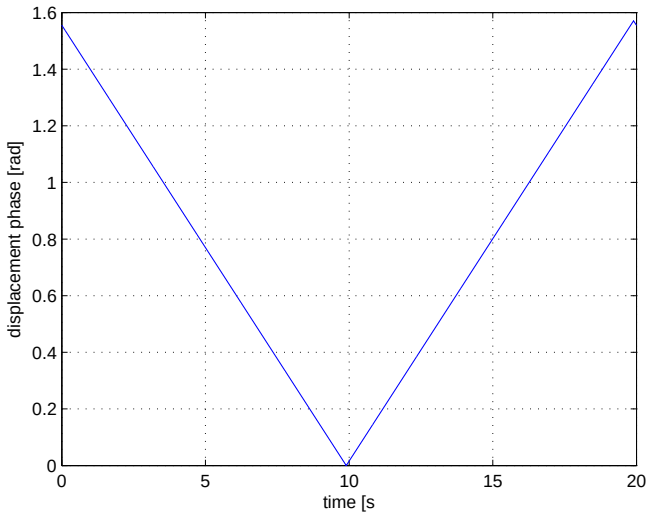

Figure 3.22: Current phase trend during variation

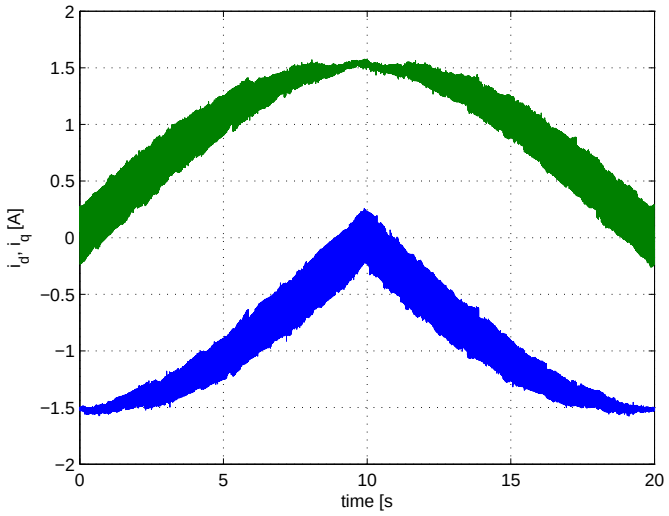

Figure 3.23: i_d and i_q currents during displacement phase variation

produces a corrective current–phase additional signal that compensates for the forced misalignment of the current with respect to the MTPA.
This helps to operate on the optimal working point and also corrects eventual drifts of the motor and controller parameters due to temperature, aging effects, etc ...
The result is shown in figure 3.26 which gives error signal and correction phase

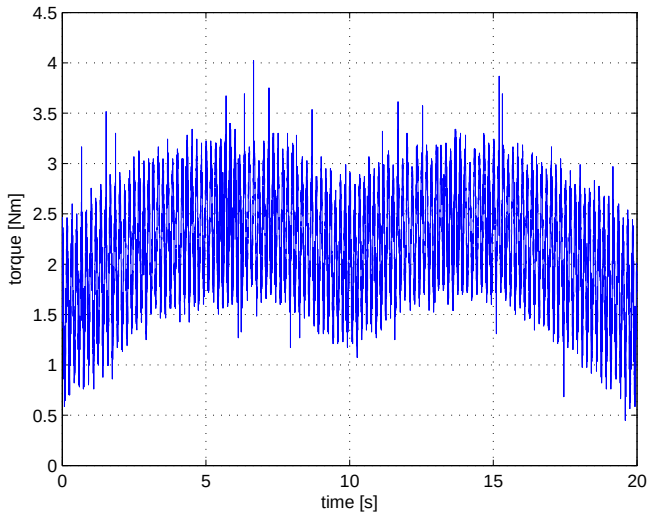

Figure 3.24: Torque measured during the displacement phase variation

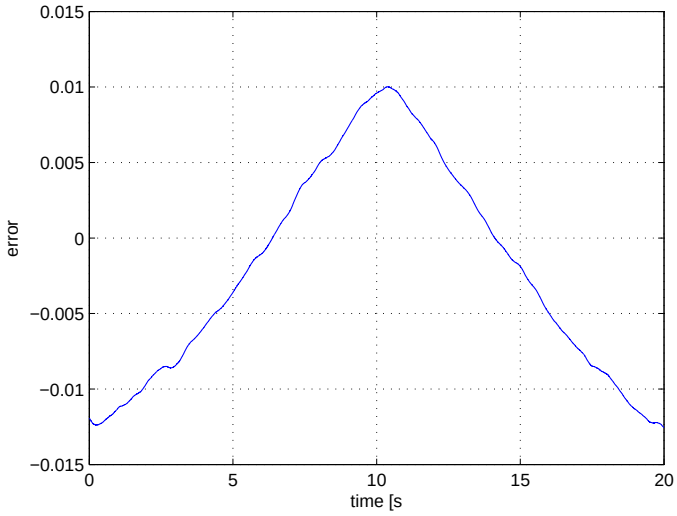

Figure 3.25: Filtered error signal during the displacement phase variation

(output of the PI controller) after the drive is started with a current phase angle of $\frac{\pi}{2}$ ($\vartheta_{disp} = 0$ in figure 3.21).
One can realizes that the error signal converges to zero (the drive reaches MTPA working condition) by delivering through the PI regulator the required MTPA current phase displacement. Such a simple self–tuning scheme of the MTPA current vector generation can be considered a basis for more elaborated

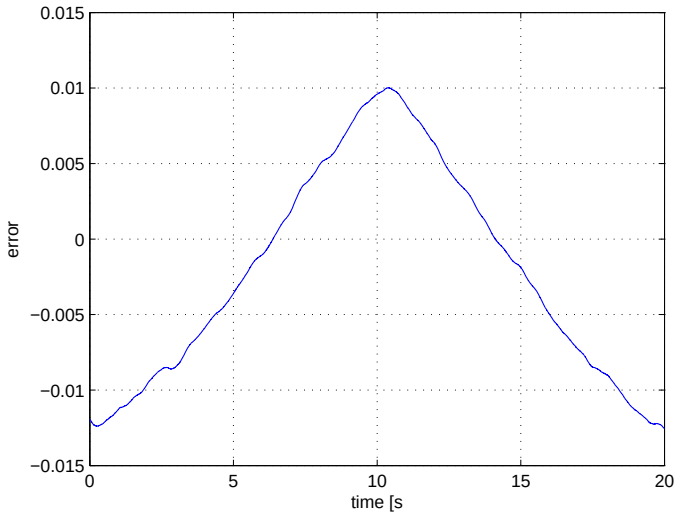

Figure 3.26: Correction phase signal during self–test algorithm

and computing intensive algorithms.
To this aim, the more effective is a strategy to distinguish between 'forced injected noise' and 'environmental noise', the better is the resulting optimization in producing the current reference components, yielding a better drive power management and energy saving.

3.2.4 Experimental validation on an industrial prototype

The self–tuning scheme for MTPA current vector generation has been tested on a laboratory industrial drive prototype, figure 3.27. The spurious torque cannot be directly measured because of the lack of torque sensors in the industrial prototype and therefore the self-tuning scheme must rely on indirect torque estimates.

If the drive operates in current–control mode (such as when the motor is required to produce a given torque at any speed) it is very hard to use the described strategy in the way it has been implemented so far because the produced torque, reconstructed from current measurements, could not be easily compared to any 'clean' (without additional noise) reference: the same quantities (the current components) are used either to carry the spurious torque component (superimposed onto the current phase) and to estimate the actual torque. It is therefore necessary another quantity to base the indirect torque

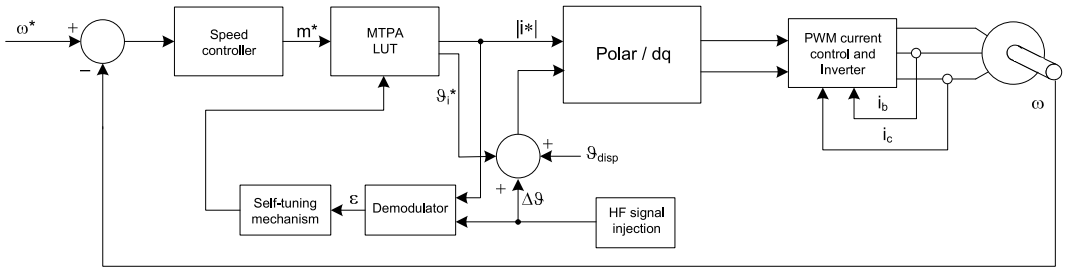

Figure 3.27: Speed control industrial prototype block diagram

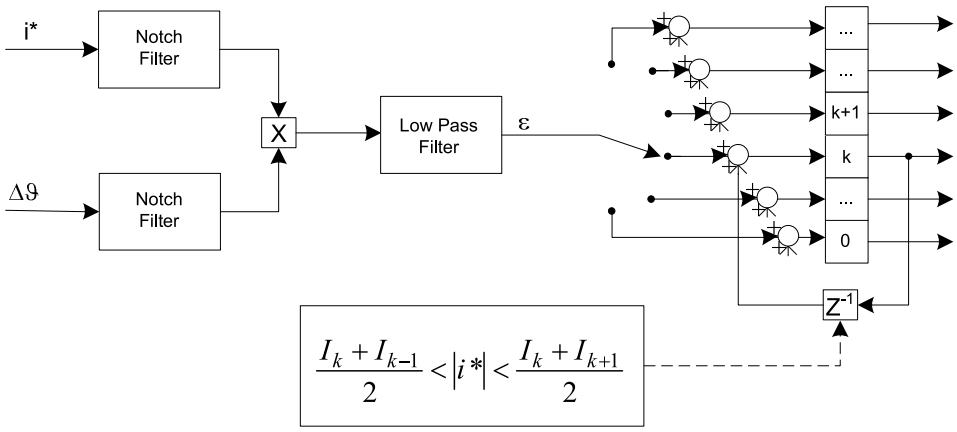

Figure 3.28: Self–tuning mechanism block diagram

analysis, as for example, the speed ripple.
If the drive operates in speed–control mode the reference current components generated by the speed controller (for the inner current/torque loop) are affected by the MTPA selection strategy (the separation of the whole current magnitude in its d– and q– components).
Any disturbance that the speed control tries to compensate acting on the reference torque (output of the speed controller) is related to the injected noise if that disturbance is strictly related to the injected pattern. If a sinusoidal high frequency current–phase is considered as revealing signal, a series of tuned high pass filters (to restrict the analyzed bandwidth) and low pass filters (to implement a modulation-demodulation scheme) have been used to obtain a signal e whose value indicates how much the working point is far from the MTPA trajectory. This procedure is depicted by the block diagram of figure 3.28.

Before activating the self-tuning mechanism, the derivation of the error signal by the scheme of figure 3.28 has been tested, while the drive is operated

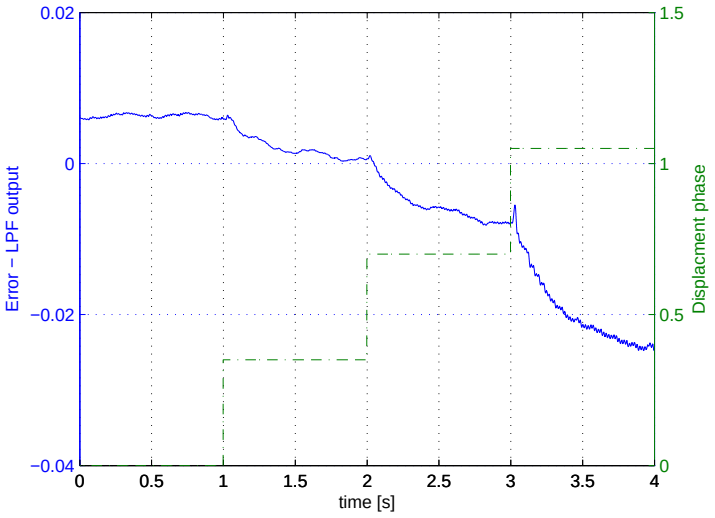

Figure 3.29: Error signal measured on industrial prototype

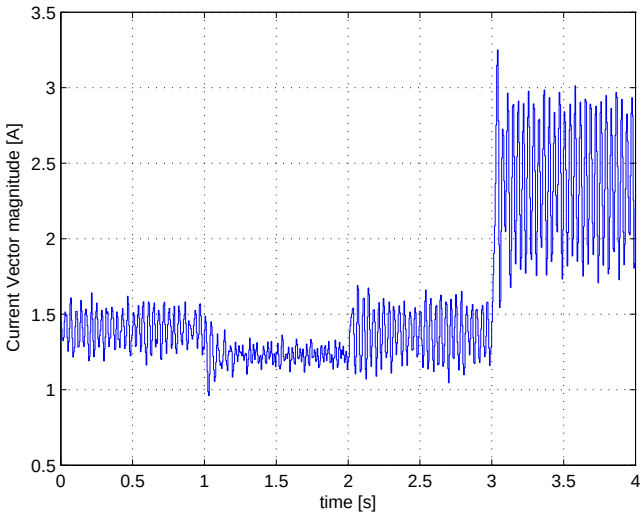

Figure 3.30: Current vector magnitude on industrial prototype

in speed–control mode dragging an electrodynamic brake.

To this purpose, the phase displacement ϑ_{disp} in figure 3.27 is changed by three steps of 20 degrees, starting from 0 to $\frac{\pi}{3}$ and the error signal as well as the current vector amplitude have been measured, as reported in figure 3.29

and in figure 3.30, while β^* at the LUT output is kept equal to $\frac{\pi}{2}$.
In addition to the phase displacement, figure 3.29 shows the filtered signal ϵ In detail the modulation/demodulation scheme that generates signal ϵ is implemented as follows:

- The detected signal i^* (representative of the generated torque) is band–pass filtered according to the spectrum of the injected signal. This grants that additional noise outside the considered bandwidth is not considered in the torque detection.

- The injected signal is band–pass filtered with an equal filter in order to keep the phase relationship between source and detected signals.

- The two signals are multiplied together (modulation). The effect of the modulation is a second harmonic component superimposed onto a continuous component whose magnitude represents the effect of the working point not being on the MTPA locus.

- A low-pass filter isolates the continuous component of the multiplied signal (demodulation) and returns the error signal ϵ.

The later converges to different levels according to the imposed phase displacement, reversing its sign when the MTPA locus is crossed. Operation after the first step, that is $\vartheta_{disp} = 0.35\ rads$ is very near to the MTPA condition as one can realize from figure 12a that shows a corresponding $\epsilon \approx 0$ and from figure 3.30 that shows a minimum average values of i* and minimum oscillations of the current reference.

3.2.5 Self-tuning of MTPA current vector generation

Given the above information, the implemented MTPA self–tuning mechanism simply updates the MTPA trajectory in order to generate the optimal reference current vector at any desired torque.
The adjustment is performed in 'quasi real–time' to the actual optimal trajectory in the $d-\quad q-$ reference frame by the mechanism sketched in the right side of figure 3.28.
The figure shows the LUT positions that contains the MTPA current phase reference for a set of current amplitude levels. The proposed mechanism consists in updating a LUT position by summing up every time the current amplitude reference remains approximately constant for a time interval longer than the

settling time of the low–pass filter around the current level of the considered LUT position.
In this way, the filtered signal is controlled to zero by the low dynamic integral action performed by the LUT updating in order to keep the working point on the MTPA locus.

Of course, the self–tuning mechanism is more effective when quiet mechanical load are driven, while it may not operate with highly perturbed load torque. In the last case, the self–tuning features of the driver should be activated during the drive commissioning on a more appropriated commissioning load.
As implemented, the strategy does not have to rely on computed or estimated motor parameters, but only on the analysis of additional signals superimposed on the driving voltages/currents, without affecting the overall drive performance.

3.2.6 Conclusions

The proposed solution of self–tuning MTPA working condition have provided good results.
The advantage that it does not have to rely on computed or estimated motor parameters, but only on the analysis of additional signals superimposed on the driving voltages/currents has confirmed the simplicity but effectiveness of the strategy. And all, without affecting the overall drive performance.
The study has revealed that the described strategy is effective if the frequency of the considered signals stay within the corresponding speed controller bandwidth.
In particular:

- the 'torque–revealing' signal spectrum must be within the speed control bandwidth because the change in the torque reference (output of the speed control) shows how good is the MTPA selection on the given working point;

- the injected noise signal (superimposed on the reference current values) must be within the current control bandwidth because it must be properly generated to trigger the corresponding change in torque.

For the further research, improvements on the algorithm may require on–purpose generated 'noise' signals to replace the sinusoidal current–phase injection considered in the presented analysis.
A mixture of deterministic and random 'noise components' are also expected to

reduce the stress on the whole drive, in particular with respect to mechanical resonance effects, that could be easily triggered by pure sinewaves (continuous deterministic patterns forcing single frequency components).
Random (or pseudo-random) Binary Sequences, modulated signals and similar waveforms could be smartly employed in self–tuning schemes, based on the same principle that drive must detect a signal added just to reveal a non–optimal working condition [13] and [14].
Such signals could also be designed on purpose to present keying patterns to be more effectively detected, thus making the self–tuning scheme robust to environmental noise, implementing the *extremum seeking* technique.

3.3 Drive communication

In typical industrial motion systems, electrical drives share a common power supply and are located far from the control supervisor. Bright examples are represented by industrial systems in which many inverter-fed ac motors share a common DC bus, or specific applications in which the drive location is critical, as in the case of submerged pumps with on-board electronic. In these applications, a dedicated bus is often used for information exchange between each drive and the remote supervisor.
The data transferred through the bus are either reference signals to the control units, or supervisor actions directed to the management of status alarms coming from the drive location.
Obviously, wired systems increase installation costs and maintenance, while reducing the overall system reliability. This is especially true when a slow data flow between the devices is enough. A dedicated bus for a low 32 $kbit/s$ rate, which is enough to transmit, every millisecond, a 16 bit digital number containing a speed reference and a word (other 16 bit) for a general-purpose status register, represents a non-negligible factor in the overall system cost.
Removing the data bus between supervisor and drives should be a significant improvement in terms of both economic savings and reliability. The actual trend of embedding intelligence in every remote component, particularly on electrical drives, can be capitalized with the purpose of creating a communication network based on the already existing power supply network. This should lead to a strong reduction in wiring costs, although the complexity of the transmission methods should increase. Besides, nowadays power line communication techniques are already adopted by several power energy distributors, to realize a data exchange between elements supplied from the main line, such as automatic measure and remote control [15].
Many studies have been conducted on noise modelling in low voltage mains for civil/residential purposes [16] and signal propagation modelling in general Power Line Communication (PLCom) communication networks [17]-[18], although industrial system PLCom applications have not been specifically investigated yet.

One of the major challenges in the use of PLCom techniques into the electrical drives scenario is represented by the communication reliability and the countermeasures for its improvement, as depicted on block diagram in figure 3.31. This picture represents a standard architecture of PLCom scheme implemented for energy consumption measures in remote access for home appliance. Actually, reliability (as trade-off with bit rate) is the key factor in an extremely noisy environment, as that of power lines feeding PWM inverters. Signal transmission among these lines suffers the presence of conducted noise due to the inverter switching activity. Moreover, in an industrial system with several in-

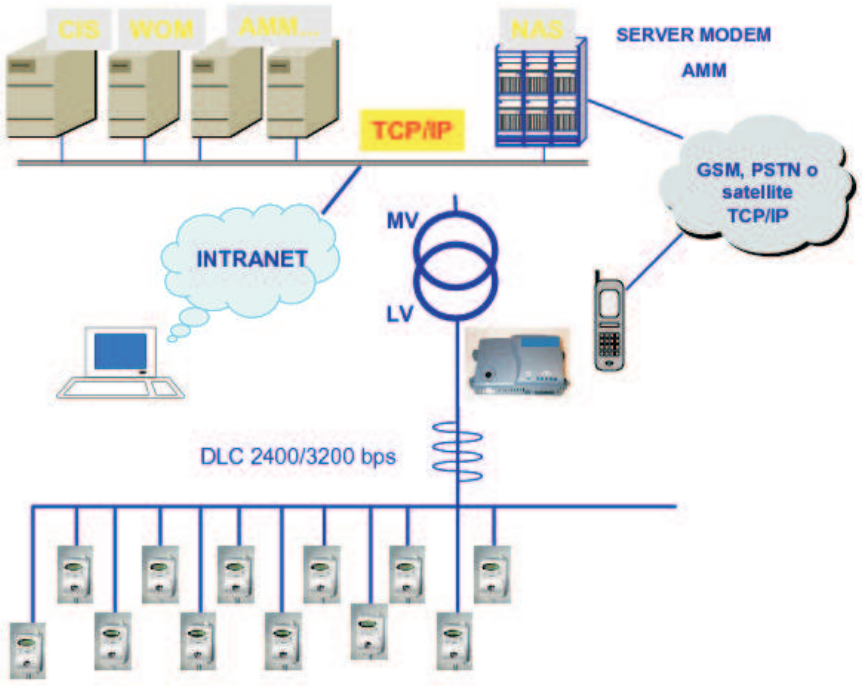

Figure 3.31: System architecture of PLCom for remote energy consumption measure

verters, each with its own switching frequency, and all sharing a common DC bus, harmonics can be predicted neither in amplitude nor in frequency.

Communication reliability on power lines can be improved not only providing a robust transmission technique with good error correction algorithms [19], [20], but also by using proper inverter modulation techniques.
As a practical example, in a shared DC bus configuration with different switching frequencies originated by an unknown number of inverters, a Random Space Vector Modulation (RSWM) technique [21], [22] should lead to consistent benefits, because of its capability of spreading the power spectrum over a broad frequency range.

During the research activity, a laboratory bench has been implemented with the purpose of exploring the benefits of RSVM techniques on a Frequency Shift Key (FSK) transmission between two industrial PLCom transceivers, located at the ends of the power cable that connects an inverter-fed induction motor to the main supply. The expected advantages are confirmed by the experimental results, which show a statistical report of various transmission tests using classical Space Vector Modulation (SVM) techniques compared with a RSVM technique.

3.3.1 The Proposed RSVM Technique

An ideal RSVM technique should vary the switching frequency or the pulse position within the switching period in a continuous and random manner. However, digital implementations of RSVM techniques must cope with the limits of fixed-point hardware and memory size. In order to obtain a simplified RSVM technique, which is suitable to be implemented on low-cost drives, a digital frequency-span RSVM algorithm has been adopted. The basic concept lies in the relation between a pseudo-random generated number and the output switching frequency range that, in this case, has been chosen between 6.3 kHz and 11.2 kHz. One of the simplest ways of obtaining m pseudo-random numbers is to use a pseudo-random generator, which can be implemented by the following recursive expression:

$$x_{k+1} = (a \cdot x_k + c) \bmod m \tag{3.19}$$

in which the `mod` operator represents the rest of the division of $(a \cdot x_k + c)$ by m. Different initial conditions x_0 leads to different sequences; moreover, there are some constraints on the values of a and c in order to obtain a good sequence of uniformly distributed random numbers, as reported in [23]:

$$\begin{gathered} \sqrt{m} \leq a \leq m - \sqrt{m} \\ a \bmod 8 = 5 \\ \frac{c}{m} = \frac{1}{2} - \frac{1}{6} \cdot \sqrt{3} \end{gathered} \tag{3.20}$$

For the implemented RSVM technique, the following values have been selected:

$$\begin{cases} m = 1024 \\ a = 517 \\ c = 217 \end{cases} \tag{3.21}$$

Moreover, considering the minimum time interval that can be represented on the microprocessor used for the RSVM algorithm implementation, that in this work was $Q = 160\ ns$, the number of different switching frequencies is equal to:

$$N_f = \frac{\dfrac{1}{f_{min}} - \dfrac{1}{f_{max}}}{Q} = \frac{\dfrac{1}{6300} - \dfrac{1}{11200}}{160 \cdot 10^{-9}} = 434 \tag{3.22}$$

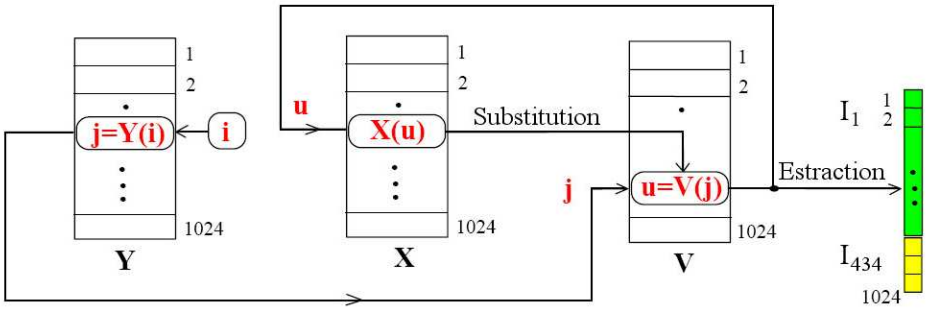

Figure 3.32: Pseudo-random sequence generation

The length m of the pseudo-random sequence reflects a compromise with the required microprocessor storage space. A value of m=1024 has been selected in this work. However, the following procedure allows the virtual stretch of the sequence, with benefits in terms of power spectral density of the resulting RSVM. Three pseudo-random sequences $\mathbf{X}$, $\mathbf{Y}$ and $\mathbf{V}$ have been created off-line by using (3.19) with the following initial conditions:

$$\begin{cases} x_0 = 0 \\ y_0 = 1 \\ v_0 = x_0 = 0 \end{cases} \tag{3.23}$$

The sequences have been stored as three vectors $\overline{\mathbf{X}}$, $\overline{\mathbf{Y}}$ and $\overline{\mathbf{V}}$ respectively. During the on-line execution of the random sequence, the vector elements are combined following three steps (figure 3.32):

- For $i = 1..m$, generation of the index $j = \overline{\mathbf{Y}(\mathbf{i})}$;
- extraction of the final value from the scramble vector $u = \overline{\mathbf{V}(\mathbf{j})}$;
- substitution of $\overline{\mathbf{V}(\mathbf{j})}$ with a new value from the sequence stored in X, $\overline{\mathbf{V}(\mathbf{j})} = \overline{\mathbf{X}(\mathbf{u})}$.

It can be shown that, if boundaries (3.20) are fulfilled, the resulting pseudo-random sequence has a repetition length of m^2. Each pseudo-random number must be associated to each of the N_f frequency (3.22). It is worth to note that a direct relation between $\overline{\mathbf{V}(\mathbf{j})}$ and N_f would lead to uniformly distributed frequencies in the frequency domain, but not in the time domain (i.e. lower frequencies are applied for a higher time with respect to higher frequencies).

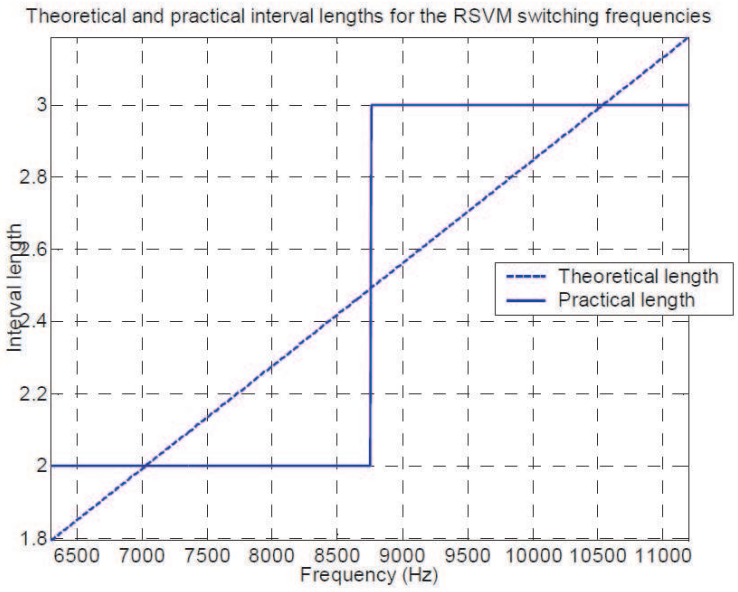

Figure 3.33: Mapping Vector for the random sequence

Although there are no significant advantages in the experimental tests, theoretical analysis of the RSVM spectrum is simplified if the frequencies are uniformly distributed in the time domain [24, 25]. To get that feature, the output sequence (which span between 1 and m) has been mapped into the N_f frequencies by setting N_f intervals of variable length, computed by

$$I_h = \frac{m \cdot f_h}{\sum_{i=1}^{N} f_i} \qquad (h = 1, \ldots, N_f) \tag{3.24}$$

In this way, the theoretical interval length related to each of the N_f frequencies assumes the linear outline, represented by the dotted line of figure 3.33. It can be interpreted by considering that a time-uniform sequence of switching frequencies would require that, for example, the frequency 7 kHz should appear twice in the m-elements vector which maps the output $\overline{\mathbf{V}(\mathbf{j})}$ to the randomly selected switching frequency. On the other hand, a higher frequency, for example 8 kHz, should appear a fractional number of times in the aforementioned mapping vector (dotted line in figure 3.33), and this is practically unfeasible. In practice, a quantization of the interval length has become necessary. Figure 3.33 indicates that the length of the intervals can be split between two and three elements. Therefore, the output frequency vector has been divided into "a" intervals of two elements and "b" intervals of three elements, satisfying

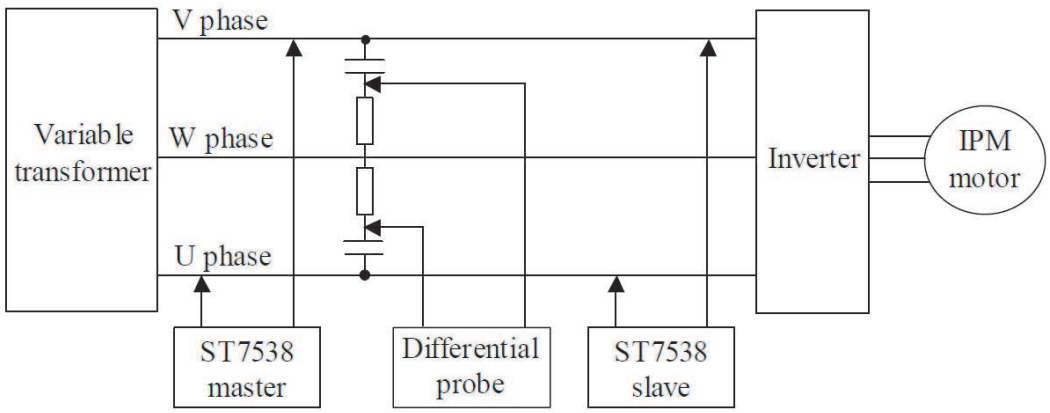

Figure 3.34: Measure Scheme used in tests

the following constraints:

$$\begin{cases} 2a + 3b = 1024 \\ a + b = 434 \end{cases} \tag{3.25}$$

which returns $a = 278$ and $b = 156$. Consequently, the output vector of switching frequencies has been divided in 278 intervals of two elements and 156 intervals of three elements, associating the lower frequencies (higher switching periods) with the 2-elements intervals, and the higher frequencies (lower switching periods) with the 3-elements intervals (continuous line, figure 3.33). Approximately, (3.25) yields the desired uniform frequency distribution in the time domain.

3.3.2 Test-Bed Implementation

The experimental laboratory setup consists of a variable transformer, an inverter-fed IM motor, and a couple of PLCom transceivers, for a master-slave communication on the U-V phase lines, as depicted in figure 3.34. The inverter is controlled by means of a card equipped with a Texas Instruments `TMS320C31` floating-point DSP, for fast control prototyping. By means of a C-written code, the control card allows an easy change of the PWM parameters characteristics, as switching frequency and type of modulation (classical PWM or RPWM). The PLCom board is based on `ST7538` Frequency Shift Keying (FSK) transceiver, whose block diagram is reported in figure 3.35. It is an integrated modem chip specifically designed for PLCom applications on low voltage (220 V) and medium voltage (2 KV) main supply. It realizes the

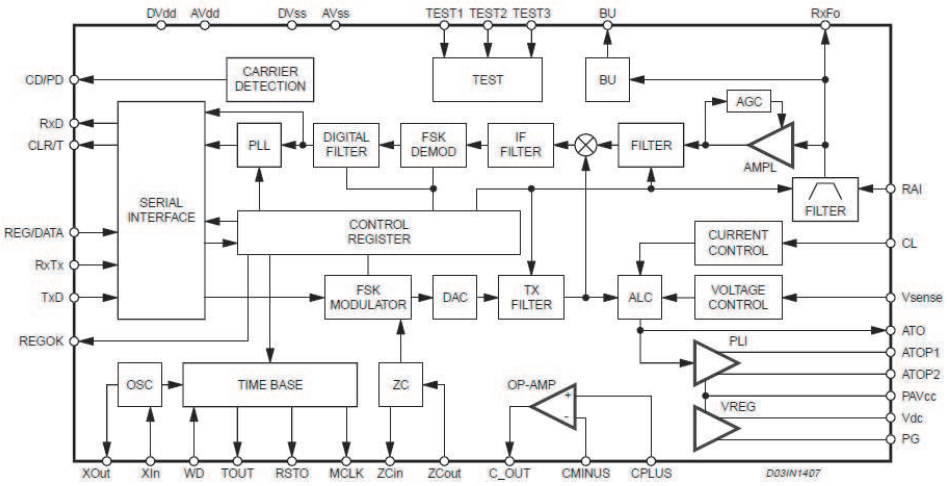

Figure 3.35: ST7538 FSK transceiver block diagram

interface from an electrical network and a system (usually a microprocessor with some sensors), which manages the main control procedure and the upper layers of the communication protocol.

The transceiver is organized in three main sections: the modem section, the serial interface with control logic section and the microprocessor supervisor section. For several reasons, which are linked to the topology of the electrical network, the noise and the low impedance of the line, the transmission is realized by means of a half duplex FSK modulation. Shortly, it is worth to recall that the FSK modulation technique translates a digital signal into a sinusoidal signal that can have two different frequency values, one for the logic high–level of the digital signal (f_h), the second one for the low level (f_l) [26]. The average value of the two tones is the carrier frequency (f_c). The difference between the two frequencies is a function of the baud rate b_r of the digital signal (the number of symbols transmitted in one second), as follows:

$$f_h - f_l = \text{dev} \cdot b_r \tag{3.26}$$

where `dev` is the deviation, a user–selectable parameter.
The PLCom board is able to communicate using one of 8 different channels (60, 66, 72, 76, 82.05, 86, 110, 132.5 kHz), selecting for the chosen channel four baud-rates (600, 1200, 2400, 4800 *baud*) and two different deviations (1 and 0.5). These parameters are configured writing the internal control register (Status Register, figure 3.35). It has been found that the transmission reliability is hardly affected by the choice of a correct parameter set, whose selection is not trivial [26, 27]. The modem provides the possibility of inserting a preamble and the reception operated by the slave card can be conditioned on

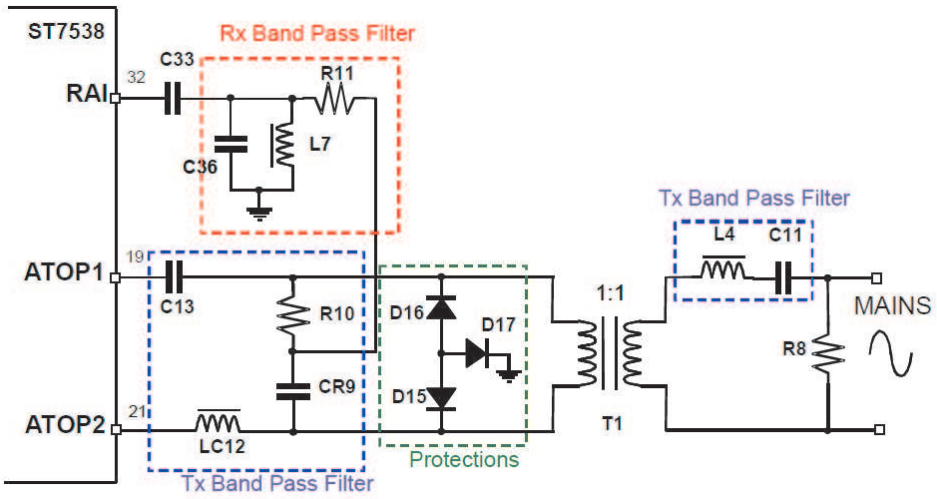

Figure 3.36: Mail line interface configuration

the recognition of a predefined characters pattern, to limit as much as possible the retransmissions, with the consequent reduction of the baud rate. Actually, the influence of noise is critical in power lines connected to PWM inverters. The preamble uses only a 16-bit sequence but reduces the reception of wrong messages or, in the worst case, the lost of the entire message. As a matter of fact, experimental results have shown an increase in communication immunity if the transmission uses the preamble detection combined with carrier detection. The PLCom board is equipped with a power line interface, which filters out all the environment noise except the band of the modulated signal. All filters' sections that compose the board circuitry interface are shown in figure 3.36. It is worth to note that the Rx Band Pass (BP) filter must be tuned according to the selected carrier frequency. The topology of the Rx BP filter is that of a resonant parallel circuit: C_{36}, L_7 and R_{11} realize a 2^{nd} order passive filter with cut-off frequency of:

$$f_0 = \frac{1}{2\pi \cdot \sqrt{C_{36} \cdot L_7}} = 132.5\ kHz \tag{3.27}$$

To limit the cross coupling with the transmission circuit, R_{11} has been selected as higher as possible. The chosen components also influence the quality factor of the filter, which is equal to:

$$Q \simeq R_{11} \cdot \sqrt{\frac{C_{36}}{L_7}} = 2.85 \tag{3.28}$$

Finally, a proprietary software supervisor runs on two PCs connected via RS232

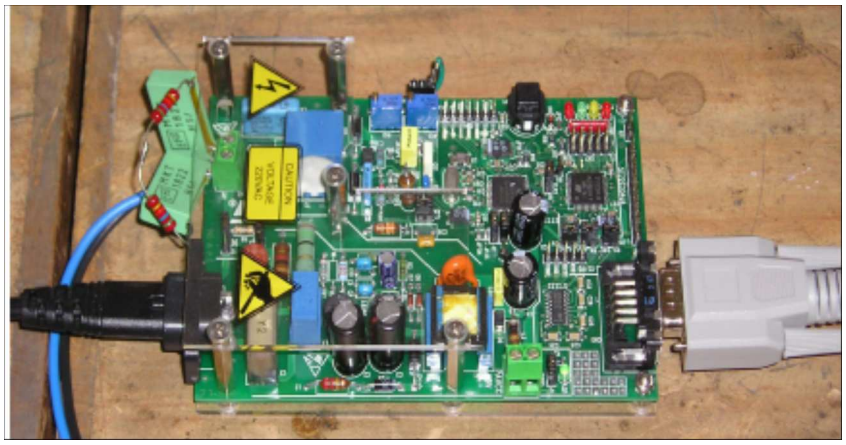

Figure 3.37: The PLCom board in the test bench

with the master and the slave PLCom transceivers, allowing transmission of arbitrary sequences of maximum 127 *bytes* with three transmission modes (continuous, one-shot or repeated N times), or ping `(Packet InterNet Groper)` operations between the cards. A photo of the PLCom board is shown in figure 3.37.

3.3.3 Experimental results

The experimental stage of the work is essentially divided in two parts: a spectrum analysis and a statistic test using the `ST7538` ping protocol with the correction bit error algorithm.

Spectrum Analysis

For the spectrum analysis, the phase-to-phase voltage has been measured utilizing a differential probe and a digital oscilloscope, as sketched in figure 3.34. FFT signals have been directly created with the oscilloscope math facilities, and then saved and post-processed in the MATLAB® environment. For the following experiments, a 4800 $baud - rate$ has been chosen, and a unit coefficient for the deviation frequency ($dev = 1$). The selected carrier frequency was $f_c = 132.5\ kHz$ so that, according to equation 3.26, the FSK algorithm uses

$$f_l = 130.1\ KHz \quad f_h = 134.9\ kHz \tag{3.29}$$

The measured FSK modulation spectrum, with an inverter DC bus of 250 V and no inverter activity, is shown in figure 3.38.

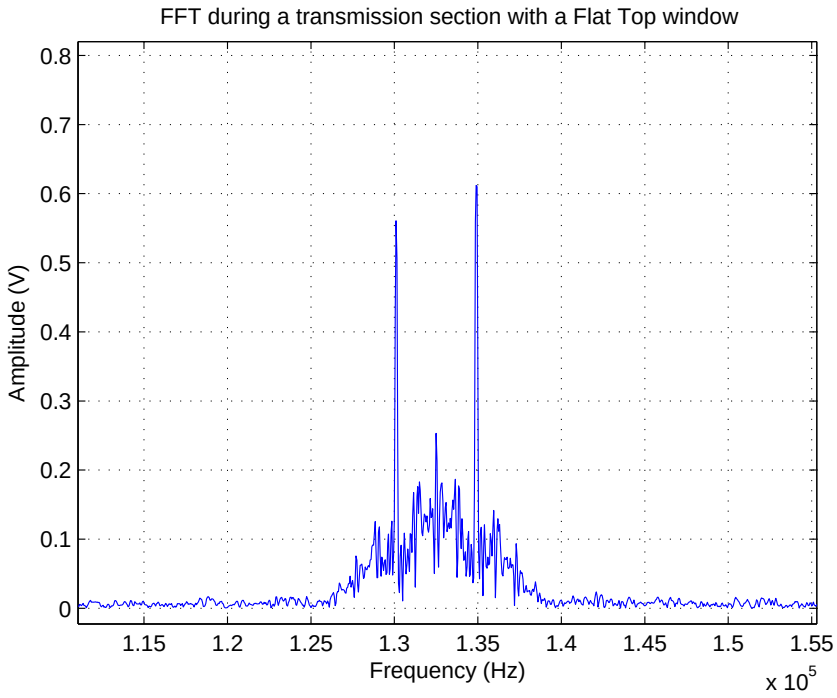

Figure 3.38: FSK spectrum during transmission ($f_c = 132\ kHz, b_r = 4800\ Hz, dev = 1$

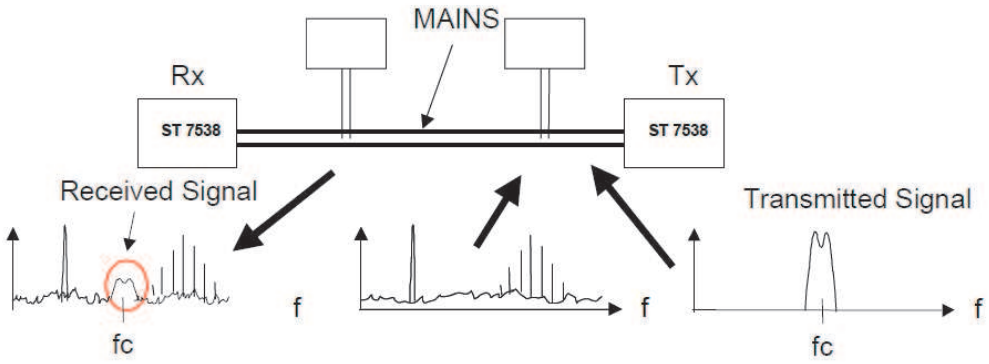

Figure 3.39: Transmission and reception board connection for tests

FSK transmissions have been performed while the inverter was feeding the IM motor with either a symmetric 12 kHz SVM [28] or with the RSVM described in Section 3.3.1.
The connection of boards for tests is shown in figure 3.39, where are reported also FSK spectrum along the mains line.

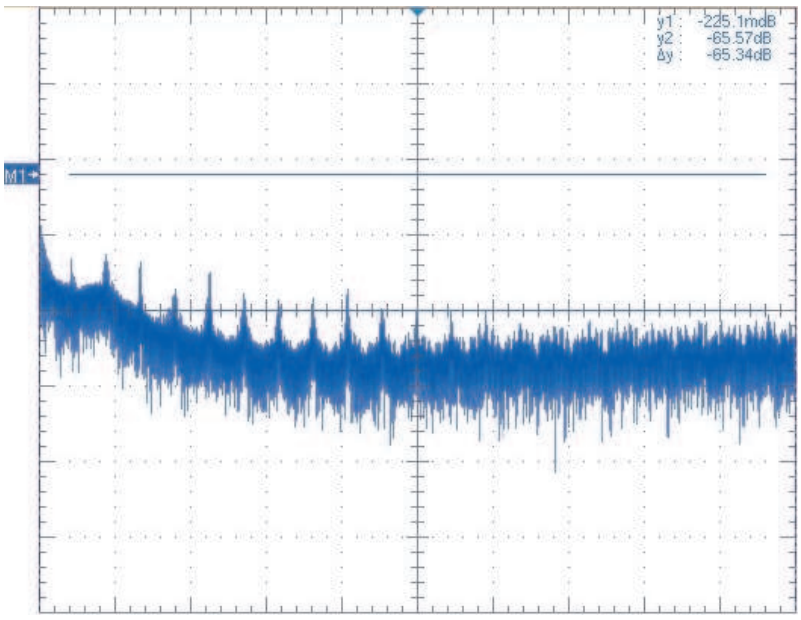

Figure 3.40: Main Supply, SVM phase-to-phase voltage spectrum ($x = 26.4\ kHz/div$, $central freq.132.5\ kHz$; $y = 36.3\ dB/div$

Figure 3.40 and figure 3.41 show the phase-to-phase main supply voltage spectrum of the 12 kHz SVM and the RSVM respectively, with a 250 V DC bus voltage and a modulation index of about 40 %.

The switching frequency at 12 kHz has been selected because its eleventh harmonic nearly matches the selected carrier frequency, and therefore it is a clear case in which the noise conducted into the mains can hardly affect the reliability of the PLCom. As expected, SVM shows sharp harmonic peaks at specific frequencies, while the RSVM exhibits a spread and smooth spectrum.

In particular, as highlighted by red circles in figure 3.40 and figure 3.41, the amplitude of the noise at the central frequency of 132.5 kHz, with RSVM, is almost 12 dB lower than that of SVM, and this has positive effects in the percentage of successful power line transmissions, as shown in the next paragraph.

Ping Test

Using the `RS232` serial port interface facility of the PLCom boards and two PCs (one for each PLCom board), it is possible to realize a ping test, to investigate on the statistics of transmitted and received data through the transmission line. The ping test architecture implemented on the PLCom board is realized

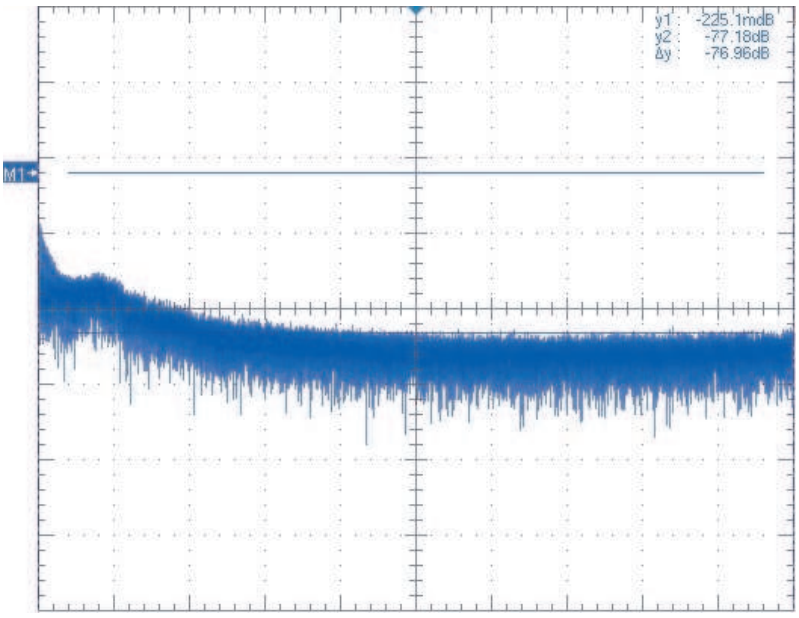

Figure 3.41: Main Supply, RSVM phase-to-phase voltage spectrum ($x = 26.4\ kHz/div$, $centralfreq.132.5\ kHz$; $y = 36.3\ dB/div$

by transmitting data frames through the line with redundant bytes, used for error detection and correction. In principle, several slaves are able to respond to the master, through an addressable protocol. In this specific case, only a board-to-board configuration has been used for the communication tests, as shown in figure 3.34. The ping protocol master frame is composed of a total of 20 bytes, as shown in Table 3.2. Once a PLCom board, acting as a master,

Preamble	Header	Slave Ad.	Master Addr.	Msg. Nr.	Aux. byte	FCS
AAAAh	9B58h	8bit	8bit	8bit	(8bit	(8bit
		+FEC	+FEC	+FEC	+FEC) $x3$	+FEC) $x2$

Table 3.2: Master frame used in Ping Test

has sent the 20 bytes frame, another PLCom board, acting as a slave, detects the data and answers with an ACK frame of the same size, which composition is reported in Table 3.3. Meanwhile, the master board waits for any slave response, for 200 ms. Then, a timeout routine is triggered, and the master reports to the PC a Not Acknowledged (NA) message, through the serial line. Different tests have been performed using different DC bus voltages, comparing the percentage of the correct received messages with either the classical SVM or the RSVM. Figure 3.42 shows a histogram of the results.

The higher the DC bus voltage, the higher the percentage of NA messages.

Preamble	Header	Slave Ad.	Master Addr.	Msg. Nr.	Aux. byte	FCS
AAAAh	E958h	8bit	8bit	8bit	(8bit	(8bit
		+FEC	+FEC	+FEC	+FEC) $x3$	+FEC) $x2$

Table 3.3: Slave response frame for Ping Test

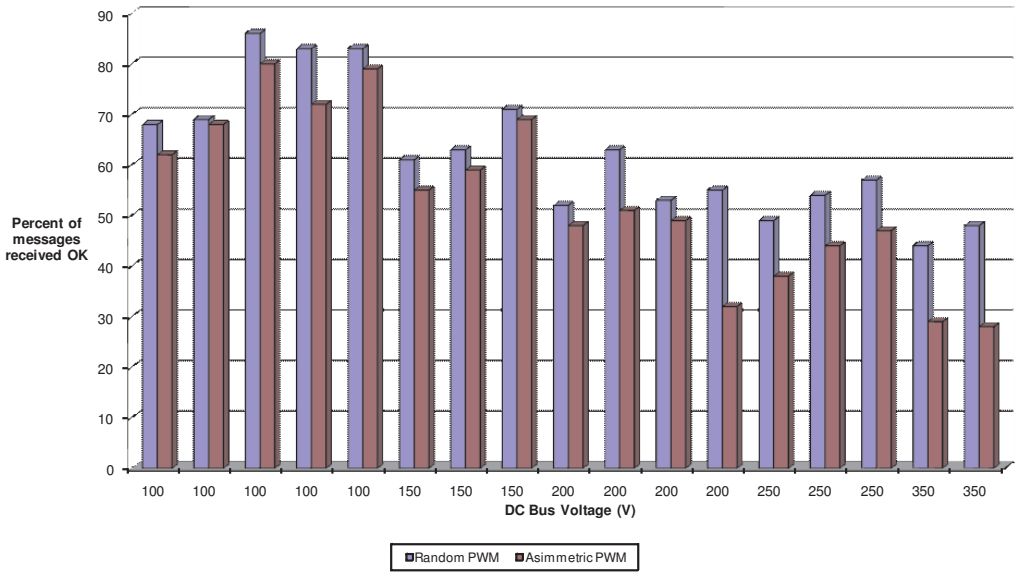

Figure 3.42: Absolute percentage of OK messages vs. DC bus voltage

This is because it is higher the noise conducted to the mains. Nevertheless, the percentage of correct data frames is in any case better with RSVM (62.29 % mean, 86 % peak, 44 % worst case) with respect to conventional SVM (53.52 % mean, 79 % peak, 28 % worst case). figure 3.43 reports another trend: among correct received messages, the percentage of messages corrected by the error correction algorithm, with respect to all acknowledged messages. Consistently with the results of figure 3.43, the number of corrected messages is generally higher as the DC bus voltage increases, while the differences between RSVM and classical SVM are not relevant in this case.

3.3.4 Conclusions

This work with the application of power line communication in the noisy environment has been carefully investigated the influence of voltage inverter modulation technique on transmission reliability. The experimental results,

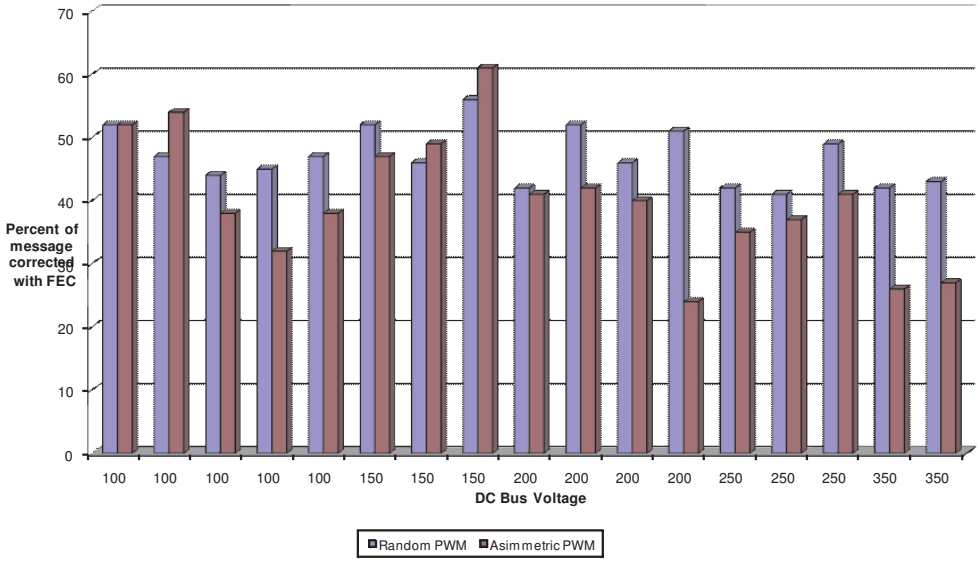

Figure 3.43: Relative percentage of corrected messages through FEC byte

carried out on laboratory setup with evaluation power communication boards have confirmed that random Space Vector Modulation, with its spread frequency spectrum, greatly improve the data integrity. The mean percentage of corrected data frames, under different working condition, passes from the 53.52 % of conventional space vector modulation to the impressive 62.29 % of random modulation. Future works will include the possible implementation of the PLCom system into a low-cost `FPGA` component, for easier integration with the drive system.

3.4 Starter Alternator

3.4.1 Introduction

Reduction of fuel consumption and increase of travel comfort are some main reasons that explain the recently trend to use electrical driven parts in road vehicles and the replacement of mechanical actuators with electromechanical counterpart [29], [30], [31], [32], [33], [34] and [35].

Due to the similar values of power generation machines in a car and of torque demand during the starting step of ICE (Internal Combustion Engine) can be a consequence to join the ICE starting and successive power generation features in the same electrical machine: the Integrated Starter–Alternator (ISA).

Following paragraphs describes a control strategy of an ISA prototype, able to achieve a high starting torque as well as a high efficiency up to the maximum speed during the generation mode of operation. Inverter voltage limitation has to be managed at the highest speed. An IPM synchronous machine with a fractional–slot winding is adopted [36]. A flux–weakening control is implemented, considering the magnetic model of the electrical machine.

3.4.2 ISA specifications and prototype characterization

The requirements of a direct–drive Integrated Starter–Alternator are very restrictive and they need to meet also cost issue. First of all, ISA has to provide an effective start–and–go capability of the vehicle. To this aim, it has to deliver a high starting torque of some tens of Nm (or more for big trucks), from standstill up to 200–400 rpm, which is the minimum starting speed of an ICE. Duration of the starting phase is normally shorter that 1 *sec*. At higher speed, ISA is asked to operate in generation mode from the minimum ICE operating speed (i.e. 1000 rpm) up to the maximum ICE speed. The power to be delivered by ISA during generation mode is decided by the global on–board electric load, the maximum of which should be more than 10 kW in electric vehicles of the next future. Last but not least, modern ISA can be also utilized for a mild hybridization of the power train, by assisting ICE with additional torque during sudden accelerations and by performing a regenerative braking feature during decelerations.
In order to fullfill the just mentioned requirement, an IPM synchronous machine with a fractional–slot winding has been chosen in this work. Such an electrical machine exhibits very high torque–to–volume ratio, high power efficiency, electromagnetic losses mainly located into the stator and thus easily

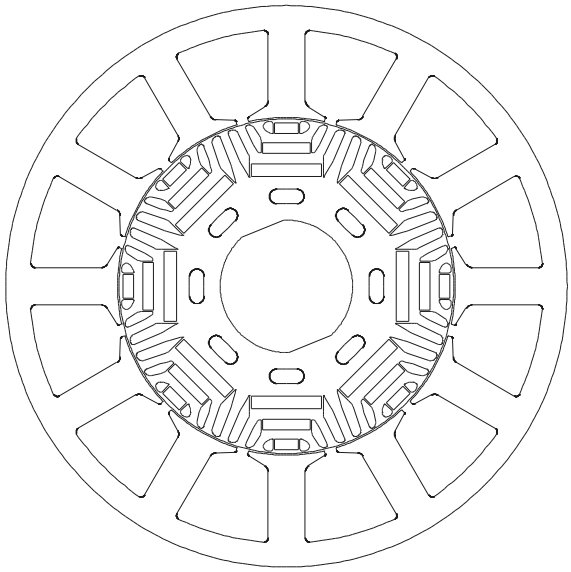

Figure 3.44: Prototype 12-slot 8-pole IPM machine

removable, and, also, field–weakening capabilities through a proper stator current control, for advantageous design of the power electronic stage. A sketch of the stator and rotor lamination of the adopted IPM machine is given in figure 3.44.

In figure 3.45 the flux linkages $\lambda_d(i_d)$ (for negative i_d on the left) and $\lambda_q(i_q)$ (for positive i_q on the right) are reported as they result from the Finite Element Analysis [36].

The machine is a low power laboratory–oriented ISA prototype that could comply with ISA requirement only for small vehicles. It has been designed to deliver a constant starting torque of 30 Nm from standstill to 300 rpm, as requested from ISA specifications. Then an accelerating torque, decreasing with the speed, can be delivered until 1500 rpm at which ISA prototype should pass smoothly from motor to generator mode for a constant torque of -3 Nm and a maximum speed of 2500 rpm.

During the implementation of tests, a 200 V inverter DC–bus has been chosen as a compromise between available laboratory equipment ratings and car specifications. However, the voltage level is mainly a issue of winding design and does not affect electromechanical performance of the drive.

As described in section 2.3, the electromechanical prototype has been tested in order to derive the information needed for designing an appropriate and effective control. This is a good way in order to design a machine model suitable for the correct control strategy.

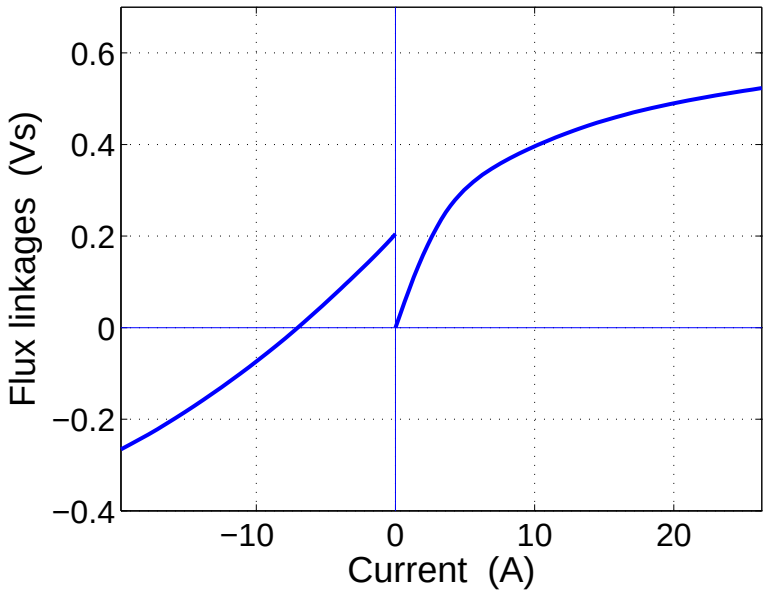

Figure 3.45: Current–flux characteristics: $\lambda_d(i_d)$ left, $\lambda_q(i_q)$ right

One of the aim of the research thread was the use and the study in dept of the method which provide the specific design of the control knowing and participating to the machine design.
During the development of this work, MTPA[4] locus has been experimentally derived.
To do this, the rotor has been locked through a torquemeter mounted in a suitably bench (see section 2.3) and a very low speed rotating current vector with constant amplitude which has been applied to the stator windings. The torque measured by the torquemeter results as in figure 3.46 during a part of the slow revolution of the current vector with 30 A amplitude.

As known, the torque is null when only d–axis current is applied and therefore d–axis position can be easily recognized from the figure. The maximum of the torque occurs when the current vector crosses the MTPA locus in the d– q–axis currents plane.
By measuring on the x–axis the distance between torque peak occurrence and zero crossing of the torque behavior in comparison to the distance between two corresponding zero crossings, the current vector angle that produces the maximum torque can be extracted. Its components give the coordinates of a point of the desired MTPA locus.
A series of successive tests at different current levels has been conducted in order to obtain the whole MTPA locus, as reported in Table 3.4 for positive

[4]Referring on subparagraph 2.2.5 for theory details.

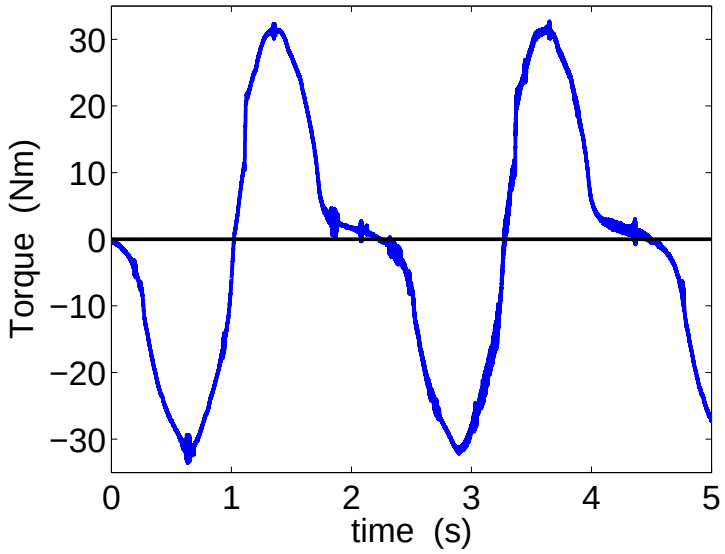

Figure 3.46: Torque vs. current vector position at locked rotor

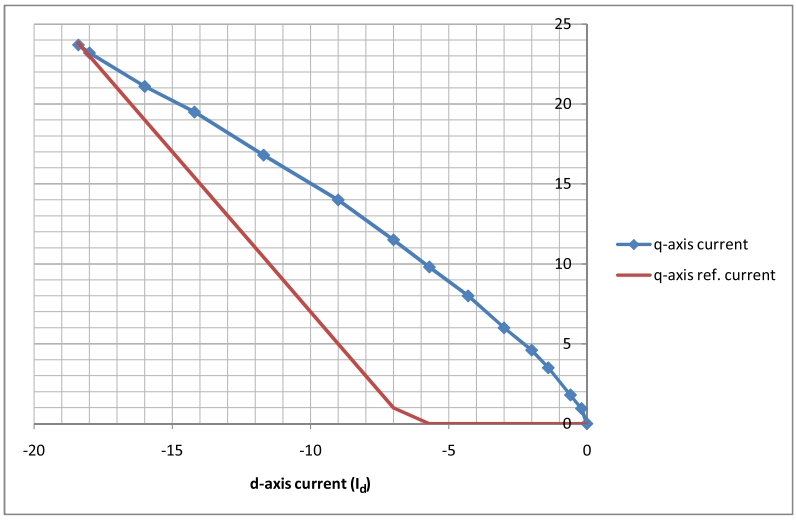

Figure 3.47: MTPA locus (marked) and ISA operating locus

torque and by marked line in figure 3.47. In that figures, marks denote measured points. As known, MTPA locus for negative torque exists symmetrically in the third quadrant of the d–q current plane.

From the figure one can realize that the desired starting torque of 30 Nm can be obtained by about 30 A of peak stator current. By estimating the corresponding d– and q–axis flux linkages from figure 3.45 it can be calculated that 30 A can be impressed up to a speed of 120 rad/s (1150 rpm) at which

Table 3.4: Measured MTPA operating points

$I_d\,(A)$	$I_q\,(A)$	$\hat{I}_{meas}\,(A)$	$\hat{T}\,(Nm)$
0	0	0	-0.05
-0.6	1.8	1.9	2.4
-1.3	3.4	3.6	5.5
-2.1	4.7	5.2	9.4
-3.0	6.1	7.1	11.8
-4.3	8.0	9.1	14.7
-5.7	9.8	11.3	17.3
-7.0	11.5	13.5	20.0
-9.0	14.0	16.6	23.6
-11.7	16.8	20.5	26.2
-14.2	19.5	24.1	28.5
-16.0	21.1	26.5	29.4
-18.0	23.2	29.3	30.4
-18.4	23.7	30.0	31.6

the voltage limit occurs.

A thermal analysis made by the motor designer indicates a rated current peak of 8 A: that corresponds to a torque of about 13 Nm.
With the given voltage, these last current and torque values can be obtained up to 165 rad/s (1580 rpm).
The voltage limit occurs at 254 rad/s (2500 rpm) for 3 Nm.

Trough this measure value, the operating regions of figure 3.48 can be drawn, together with the speed–torque requirement of the ISA application.

3.4.3 The ISA control scheme

A vector current control in d– q– synchronous reference frame (fixed to the rotor) is implemented, as one can see in the figure 3.49, [37].
Two current loops are closed using equivalent PI controllers. The current references which enter the difference block of loops are derived from the torque demand m^*. As depicted in the scheme 3.49, both the output of the current loops are limited with values computed according to assumed ISA specifications and the control strategy.

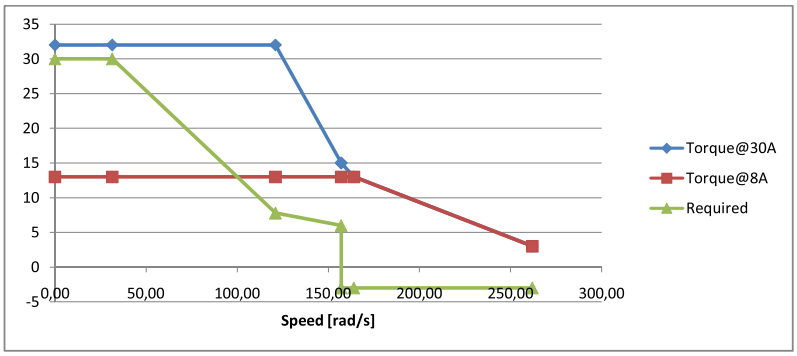

Figure 3.48: ISA operating regions

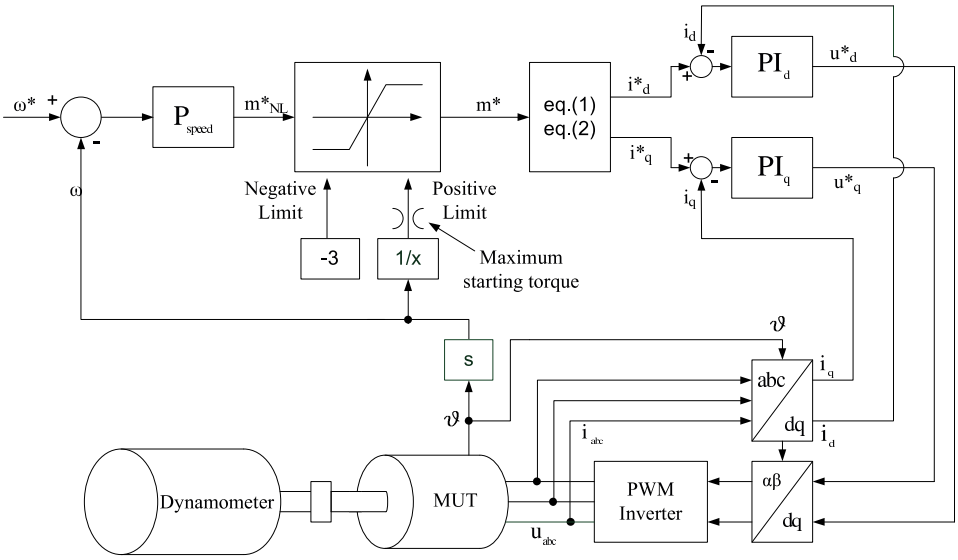

Figure 3.49: Control scheme

For this work, the torque limits are $-3\,Nm$ and $30\,Nm$, where the negative limit is the maximum torque needed in generation mode while the positive limit is required for starting the ICE.

Motor to generator transition is managed by an outer speed loop incorporating a simple high gain P (proportional) controller. The output of the controller is the non-limited torque demand which is the input of the torque limit strategy described later. The speed reference ω_{ref} is the speed of the transition from motoring to generating mode. This because the gain of the proportional controller is high enough to cause the action of the torque limiter at any speed (producing really a torque–controlled drive) apart from a narrow range of speed around the speed reference where the transition occurs.

Current Control

The current control is based on a conventional scheme with two loops for both d– and q–axes. The current control is obtained with two PI controllers whose references are designed as illustrated on the next paragraph. Current controller outputs (voltage references) are limited to meet voltage capabilities of the inverter.
The design of controller transfer function has been made using *Ziegler–Nichols method*, in order to guarantee a stability of loops.

Torque Control

Current reference signals are derived from the desired torque. The adopted solution consists of implementing an approximated MTPV (Maximum Torque Per Volt) strategy in the low torque range (at higher speed when the drive operation is limited by the voltage capabilities of the inverter). When a high torque is demanded (that is when the motor is going at low speed), the operating point locus is moved toward the MTPA in order to satisfy at the best the starting specifications. The implemented torque-to-current control law is shown in figure 3.47 in non-marked line, and is given by:

$$i_q^* = i_q(m^*) \tag{3.30}$$
$$i_d^* = -6.5 - 0.5 \cdot |i_q^*| \tag{3.31}$$

Equation (3.30) is derived by computing the torque for each pair of currents components given by equation 3.31, by means of the current–flux characteristics of figure 3.45.
It is worth noticing that the no–load d–axis current is equal to $-6.5\ A$. It corresponds to the short circuit current of the generator, i.e. the current that makes the d–axis flux linkage to be zero, which can be read in figure 3.45 and corresponds to:

$$i_{d_{sh}} = -\frac{\Lambda_{mg}}{L_d} \tag{3.32}$$

The no–load currents $i_{d_{sh}} = -6.5\ A$ and $i_{q_{sh}} = 0\ A$ are thus the coordinates of the short circuit operating point in the d– q– currents plane. This corresponds to the center of the voltage limits and the origin of the MTPV locus [38].
Lower no–load d–current absolute value can be adopted to reduce joule losses in the low/medium speed range.

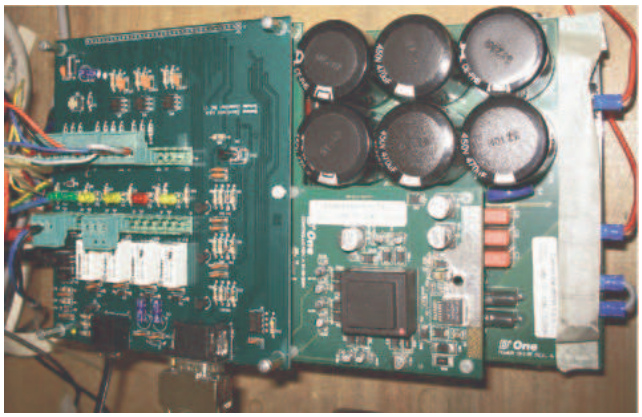

Figure 3.50: Inverter for ISA drive

Torque limits

The torque demand (and thus the delivered torque) is limited positively (motor) and negatively (generator) in different way. The motoring torque has a constant maximum limit at low speed (up to 300 rpm) than can be set from 0 Nm to 30 Nm. Above 300 rpm the positive torque limit decreases according to a $1/\omega$ law to have an accelerating torque region with a delivered constant power. The generating torque (that occurs only at high speed after the motor to generator transition) has a constant limit of $-3\,Nm$ in this laboratory drive. In practical application, the generator torque is decided by the voltage control on the battery DC bus and therefore depends on the electrical load connected to the same bus.

3.4.4 Experimental tests

The drive of the ISA uses a prototype three-phase IGBT inverter controlled by a Digital Signal Processor programmable via serial communication line. The inverter is shown in figure 3.50. This inverter use a vector PWM modulation with a switching frequency of 10 kHz and current measure with 2 Hall sensors.

The inverter software is written in C and Assembly languages and some internal variables can be read and written using a PC–interface; this allows some parameters or set–points to be readily adjusted.
Figure 3.51 and figure 3.52 shows the motor components. A 100 Nm torque transducer, has been used during all measures.

Figure 3.51: ISA Stator

Figure 3.52: ISA Rotor

Several tests have been carried out on the ISA drive. The test bench used for the experimental validation is shown in figure 3.53, where the ISA is visible on the right.

A field oriented controlled Induction Motor (IM) drive (on the left in the figure) is used and managed to emulate the ICE behavior. A slow ramp speed reference is applied to the IM drive from standstill up to its maximum speed, i.e. 2500 rpm. The torque limit is set lower than 30 Nm according to the test. In this way the acceleration is mainly decided by the ISA drive and system inertia, while above 1500 rpm the IM drive acts as a motor driving the PM alternator.

An example of test results is reported in figure 3.54, figure 3.55 and figure 3.56.

During these tests the required starting-torque as been set to the value of

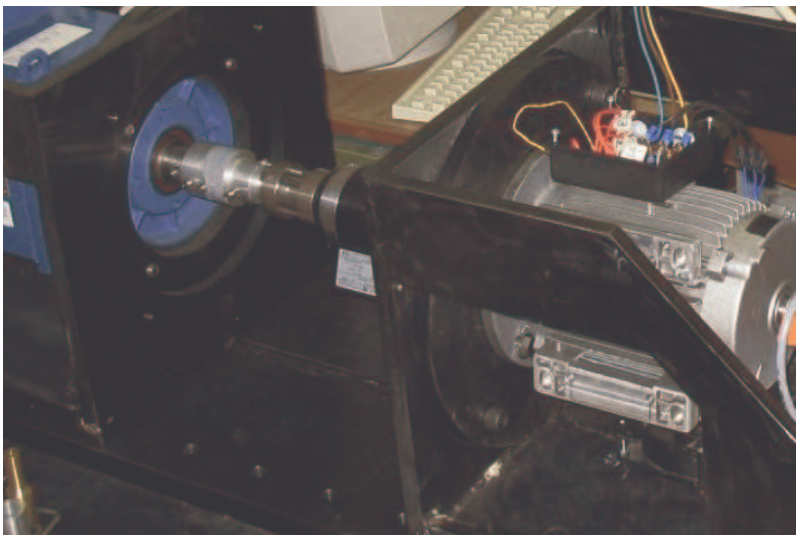

Figure 3.53: Test benches for ISA machine

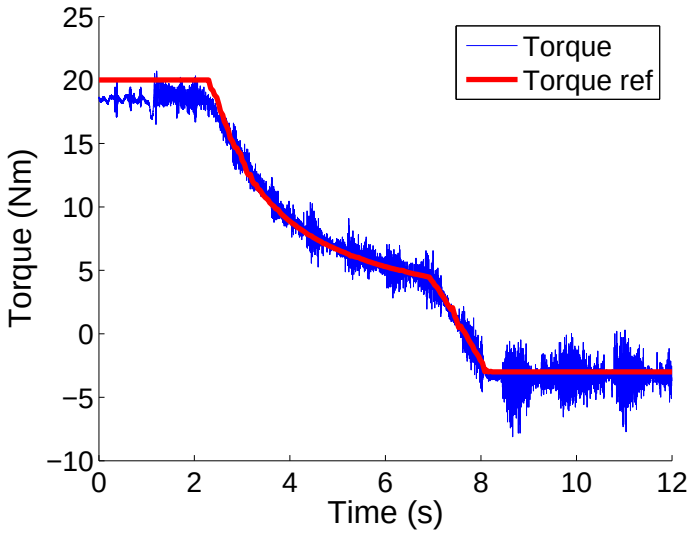

Figure 3.54: Measured torque behavior during test with starting-torque $T_{st} = 20\,Nm$ and cut–off speed $n_{cut} = 1500\,rpm$

20 Nm for matching better the available braking torque of the IM drive. The transition speed is equal to 1500 rpm. figure 3.54 refers to the delivered torque during the starting process. The measured torque is reported together with its reference detected at the output of the torque limiter in figure 3.49. It should be noted that there is a good agreement between measured and reference torque and a smooth transition from positive to negative torque as required by ISA control specifications.

Figure 3.55 and figure 3.56 shows the d–axis and q–axis current during the same start-up test. Measured values are plotted in red line while reference one is blue colored.

Both figures confirm the good agreement between the d– and q–axis currents and the corresponding current references. In particular, it can be noted that the d–axis current assume its offset value of $-6.5\ A$ when the torque is null during the mode transition.

3.4.5 Conclusions

The statement of control presented has highlighted the weight of the simple but specifically designed strategy.
Prototype implementation has given good results and has confirmed the stability of the control.

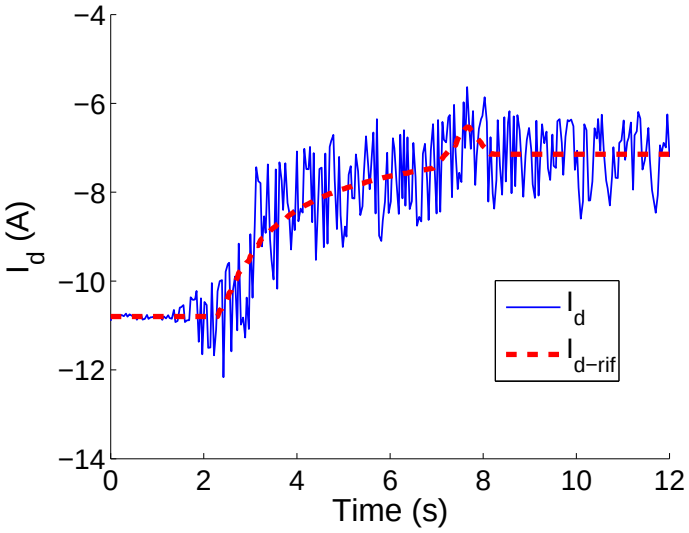

Figure 3.55: Measured I_d behavior during test with starting–torque $T_{st} = 20\ Nm$ and cut–off speed $n_{cut} = 1500\ rpm$ (solid lines is measured current, dashed lines is reference current)

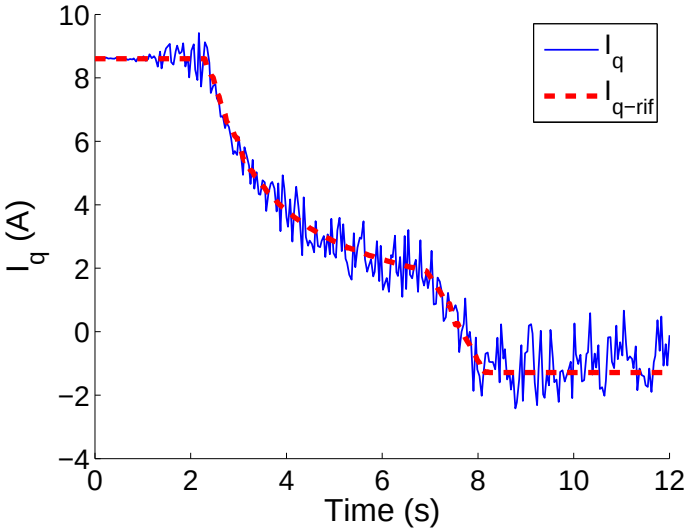

Figure 3.56: Measured I_q behavior during test with starting-torque $T_{st} = 20\ Nm$ and cut–off speed $n_{cut} = 1500\ rpm$ (solid lines is measured current, dashed lines is reference current)

For the future, some more experimental test should be conducted in order to verify the dynamic behavior of Starter–Alternator, especially during motor–generator transition.

Chapter 4

Conclusions

The applications of Permanent Magnet Motors presented in this PhD-thesis reveal that a well–selected control strategy allows to achieve in a good way the user demanded performance.

The effectiveness of the test bench for Permanent Motors, developed during the research activity, has confirmed to be an useful tool for electrical drives design and control.
The possibility to tests prototypes is very important for the best completion of the development of an innovative motor, and its functionality has been proved in the presentation of various real applications.
The same test bench is useful in identifying the motor model for control purposes.

Different applications have been reported in the thesis.

The development of a direct drive lift system control has been presented with the description of the accurate dynamic motional model, including the rope elasticity.
The investigation concerns the impact of feed forward strategy using quantity estimation to perform high dynamic response.

A section has reported as well some control design guidelines for a Starter–Alternator, applied in an hybrid vehicle. Also in this application, the importance of a specifically control strategy has been highlighted by results.

Next, the thesis has illustrated a self–tuning of Maximum Torque Per Ampere curve method, with high frequency signal injection. Results reveal the effectiveness of the system, in particular for the auto–tuning scheme.

In addition, a presentation of the usefulness and benefits of a Power Line

Communication for electrical drives placed in an industrial environment has confirmed improvement possibility by using random PWM.

In addition to the control algorithm description and its design for PM synchronous motors drives presented in the thesis, there are also some ideas for further researches in this and related fields.
For MTPA self–tuning scheme, more tests can be carried out in order to obtain more information about updating of MTPA locus points.
Also, extremum seeking algorithm can be tested for a better recognition of MTPA condition in a noisy environment.
Since electric machines and power electronics are key components in electric and hybrid drivetrains, this offers good opportunities for further research in this multi–disciplinary field.

The main results of the works reported in this thesis have been presented in International Conferences.

Appendix A

List of Symbols and Abbreviations

U	voltage
U_N	nominal voltage
U_N	nominal voltage
U_{RMS}	root mean square voltage (line–to–line)
U_d, U_q	direct axis voltage, quadrature axis voltage
U_{dc}	mean value DC–link voltage
E	back electromotive force
I	current vector magnitude
I_N	nominal current intensity
I_{RMS}	root mean square current intensity
I_d, I_q	direct axis current, quadrature axis current
I_{dc}	mean current absorbed by DC–link
P	power
R	line resistance
L	inductance, synchronous inductance for PM motors
L_d, L_q	direct axis inductance, quadrature axis inductance (for IPM motors)
λ_d, λ_q	direct axis flux linkage, quadrature axis flux linkage
λ_0	total amount of flux linkage on an electrical machine (equal to $\sqrt{\lambda_d + \lambda_q}$)
Λ_{mg}	maximum flux linkage for a line due to permanent magnet (PM motors)
M	mechanical torque provided on the motor shaft
Ω_m	angular speed expressed in rad/s (complete mechanical turn)
n	angular speed expressed in rpm (complete mechanical turn)

Ω_{me}	electromechanical speed expressed in rad/s ($p\,\Omega$)
Ω_B	base speed expressed in rad/s
β	current vector phase
δ	duty-cycle
f, f_c	frequency, switching frequency
p	number of pole pairs

Bibliography

[1] T.M. Jahns, G.B. Kliman, and T.W. Neumann. Interior PM synchronous motors for adjustable speed drives. *IEEE Trans. on Industry Applications*, IA–22(4):738–747, July/Aug 1986.

[2] N. Bianchi. *Design, Analysis, and Control of Interior PM Synchronous Machines (N. Bianchi, T.M. Jahns editors)*, chapter *Analysis of the IPM motor – Part II, Finite Element approach*, pages 3.34–3.66. IEEE IAS Tutorial Course notes, IAS Annual Meeting, CLEUP, Seattle, October 3, 2004. (info@cleup.it).

[3] S. Morimoto, Y. Takeda, T. Hirasa, and K. Taniguchi. Expansion of operating limits for permanent magnet motor by current vector control considering inverter capacity. *IEEE Transactions on Industry Applications*, 26(5):866–871, September/October 1990.

[4] S. Bolognani, M. Dai Pre', and L. Sgarbossa. An effective test bench for pm synchonous motor characterization. In *IEEE Conference of Electrical Machines*, September 2006.

[5] L. Sgarbossa, M. D. Pre', and S. Bolognani. An automated quasi-static test bench for a detailed torque characterization of PM synchronous motors. In *Universities Power Engineering Conference, 2006. UPEC '06. Proceedings of the 41st International*, volume 2, pages 758–763, September 6–8, 2006.

[6] NEMA. Ics 16 motion/ position control motors, controls, and feedback devices. Technical report, NEMA Standards Publication.

[7] G. Ciammetti, N. Bianchi, and G. Grezzani. External-rotor surface-mounted permanent-magnet motor for direct-drive elevator systems. In *Proc. of Power Converter, Intelligent Motion Europe Conference, PCIM 2005*, pages 1–6, CD–Rom, Nürnberg, Germany, 7–9 June 2005.

[8] Y. Takeichi, S. Komada, M. Ishida, and T. Hori. Speed control of symmetrical type three-mass resonant system by PID-controller. In *Advanced Motion Control, 1996. AMC '96-MIE. Proceedings., 1996 4th International Workshop on*, volume 2, pages 594–599, Mie, March 18–21, 1996.

[9] S. Bolognani, A. Venturato, and M. Zigliotto. Theoretical and experimental comparison of speed controllers for elastic two-mass-systems. In *Power Electronics Specialists Conference, 2000. PESC 00. 2000 IEEE 31st Annual*, volume 3, pages 1087–1092, Galway, June 18–23, 2000.

[10] P. Vas. *Sensorless Vector and Direct Torque Control*. Oxford University Pubblications, 1992.

[11] P. Vas. *Estimation, Condition, Monitoring and Diagnosis of Electrical Machine*. Oxford University Pubblications, 1993.

[12] S. Morimoto, K. Hatanaka, Y. Tong, Y. Takeda, and T. Hirasa. Servo drive system and control characteristics of salient pole permanent magnet synchronous motor. *IEEE Transactions on Industry Applications*, 29(2):338–343, March/April 1993.

[13] R.H. Josselsonn and J. Predina. Simultaneous rapid open and closed loop bode plot measurement using a binary pseudo-random sequence. Technical report, United States Patent n.6895352, 2005, May 17.

[14] C. Bartholomeusz. *Frequency Response Testing of Synchonous Machines*. PhD thesis, The University of Queensland, 1999.

[15] I. H. Cavdar. A solution to remote detection of illegal electricity usage via power line communications. *IEEE Transactions on Power Delivery*, 19(4):1663–1667, October 2004.

[16] H. Meng, Y. L. Guan, and S. Chen. Modeling and analysis of noise effects on broadband power-line communications. *IEEE Transactions on Power Delivery*, 20:630–637, April 2005.

[17] I. C. Papaleonidopoulos, C. N. Capsalis, C. G. Karagiannopoulos, and N. J. Theodorou. Statistical analysis and simulation of indoor single-phase low voltage power-line communication channels on the basis of multipath propagation. *IEEE Transactions on Consumer Electronics*, 49(1):89–99, February 2003.

[18] Wu Qiong Luo, Soon Yim Tan, and Boon Tiong Tan. Effects of the ground on power-line communications. *IEEE Transactions on Microwave Theory and Techniques*, 53(10):3191–3198, October 2005.

[19] D. Cooper. Low-data-rate narrow-band power-line communications on the european domestic mains: symbol timing estimation. *IEEE Transactions on Power Delivery*, 20:664–667, April 2005.

[20] E. Del Re, R. Fantacci, S. Morosi, and R. Seravalle. Comparison of CDMA and OFDM techniques for downstream power-line communications on low voltage grid. *IEEE Transactions on Power Delivery*, 18(4):1104–1109, October 2003.

[21] A. M. Trzynadlowski, M. M. Bech, F. Blaabjerg, J. K. Pedersen, R. L. Kirlin, and M. Zigliotto. Optimization of switching frequencies in the limited-pool random space vector PWM strategy for inverter-fed drives. *IEEE Transactions on Power Electronics*, 16(6):852–857, November 2001.

[22] S. Bolognani, R. Conton, and M. Zigliotto. Experimental analysis of the EMI reduction in PWM inverters using random space vector modulation. In *Industrial Electronics, 1996. ISIE '96., Proceedings of the IEEE International Symposium on*, volume 1, pages 482–487, Warsaw, June 17–20, 1996.

[23] D.E. Knuth. *The art of the computer programming, vol.2*. Addison–Wesley Pub. Co., New York, 1969.

[24] M. Andrews and J. T. Boys. Improvements in estimating the spectra of random PWM waveforms. *Electronics Letters*, 29:1822–1823, October 14, 1993.

[25] M. Andrews and J. T. Boys. Improvements in estimating the spectra of random PWM waveforms. *Electronics Letters*, 29:1822–1823, October 14, 1993.

[26] G. Cantone. St7538 fsk power line transceiver demo kit description. Technical report, ST Microelectronics Application Note 1714, 2003.

[27] ST Microelectronics. St7538 fsk power line transceiver data sheet. Technical report, ST Microelectronics, 2003.

[28] J. Holtz. Pulsewidth modulation-a survey. *IEEE Transactions on Industrial Electronics*, 39(5):410–420, October 1992.

[29] R. Dutta, M.F. Rahman, and M.A. Rahman. An ipm machine with segmented magnet rotor for integrated starter alternator. In *3rd International Conference on Electrical and Computer engineering*, Dhaka, Bangladesh, December 2004.

[30] C. P. Mudannayake and M. F. Rahman. An integrated starter alternator for the 42 v powernet. In *Power Electronics and Drive Systems, 2003. PEDS 2003. The Fifth International Conference on*, volume 1, pages 648–653, November 17–20, 2003.

[31] Junha Kim, Jinhwan Jung, and Kwanghee Nam. Dual-inverter control strategy for high-speed operation of EV induction motors. *IEEE Transactions on Industrial Electronics*, 51(2):312–320, April 2004.

[32] Jun Zhang and M. F. Rahman. A direct-flux-vector-controlled induction generator with space-vector modulation for integrated starter alternator. *IEEE Transactions on Industrial Electronics*, 54(5):2512–2520, October 2007.

[33] A. Malikoupoulos, Z. Filipi, and D. Assanis. Simulation of an integrated starter alternator (isa) system for the hmmwv. Technical report, SAE Technical Paper n. 2006-01-0442, 2006.

[34] J. Wai and T. M. Jahns. A new control technique for achieving wide constant power speed operation with an interior PM alternator machine. In *Industry Applications Conference, 2001. Thirty-Sixth IAS Annual Meeting. Conference Record of the 2001 IEEE*, volume 2, pages 807–814, Chicago, IL, September 30–October 4, 2001.

[35] J. G. Kassakian, J. M. Miller, and N. Traub. Automotive electronics power up. *IEEE Spectrum*, 37(5):34–39, May 2000.

[36] L. Sgarbossa, M. Dai Pre', M. Barcaro, L. Alberti, A. Faggion, and N. Bianchi. Design of an ipm motor for integrated starter alternator. *Paper submitted for pubblication*, 2007.

[37] P. Vas. *Vector control of AC machines*. Oxford Science Publications. Claredon Press, Oxford, 1990.

[38] S. Morimoto, M. Sanada, and Y. Takeda. Performance of PM-assisted synchronous reluctance motor for high-efficiency and wide constant-power operation. *IEEE Transactions on Industry Applications*, 37(5):1234–1240, September/October 2001.